Novel applications of structured light in the field of atom optics. Imagining optical magnetometry with images

Francesco Castellucci

Submitted in fulfilment of the requirements for the degree of

Doctor of Philosophy

School of Physics and Astronomy

College of Science and Engineering

University of Glasgow

November 2021

Abstract

Complex vectorial light fields offer unprecedented information capacity and flexibility to design light potentials with correlated or multiplexed intensity, phase and polarisation structures. In recent years many different new techniques and technological devices have been developed with the goal of allowing for the efficient generation of these fields with maximum flexibility and reliability. During my studies I employed some representatives of these newer techniques, as the light fields involved in the experiments were generated with setups containing equipment such as *Digital Micromirror Devices* (DMDs), *Spatial Light Modulators* (SLMs) and Q-plates, all of which can be regarded as being on the forefront of the development in the world of structured optics.

The main beneficiaries of this "expansion" in the generation of light fields are topics traditionally linked to optics such as microscopy, imaging and spectroscopy. However, another field that could benefit from these newer applications is atom optics. In fact, the interaction between atoms and light is vectorial in nature, as it is manifest in the electric dipole coupling which is the principal avenue of interaction between them. Main consequence of this kind of interaction are the appearance of non-linear behaviours, even for light parameters associated to a semiclassical description, e.g. coherent light from a laser source. The principal investigation during my Ph.D. can be regarded as one of the tentative efforts to introduce the innovation of structured light and atom optics, since I have focused my efforts around the experimental study of the mutual interaction of a cloud of cold rubidium atoms with a vectorial light field, carrying *Orbital Angular Momentum* (OAM) in the presence of a magnetic field. The main goal of the study was to describe and demonstrate how 3D magnetic field alignment can be inferred from single absorption images of an atomic cloud. The atomic cloud was prepared in a particular state of density, temperature and population distribution with the employ of a *Magneto Optical Trap* (MOT) first, and *Spontaneous Force Optical Trap* (SpOT) second, which are

widely utilized techniques in the world of atom optics. Then a vector vortex beam was used to interrogate the magnetic spin states population of the atoms cloud. In fact due to the relative position between the local light polarisation, which varies in the beam, and the magnetic field direction, fixed for the whole atomic sample, the absorption of the light would be affected. By varying the magnetic field inclination or azimuthal angles, the absorption pattern would vary as well confirming the previous model developed by former PhD students. In the future it is planned to address some of the limitations that are intrinsic to the selected method, the Q-plate, of generating the vector vortex light by switching to one of the other above mentioned SLM or DMD setups to obtain a wider selection of polarisation patterns to stimulate the atoms. Another venue of development is the translation of the whole system at room temperature, with the prospect of achieving a faster rate of repetition for the experiment at the expense of some control over the atomic medium.

In addition to the atomic magnetometry experiment in Glasgow, during my PhD I have been collaborating on other projects with various other physics group both within the same University of Glasgow and in the wider optics fields worldwide. The most relevant of these has been the *European Training Network* (ETN) called *Collective Effects and Optomechanics in Ultra-cold Matter* (ColOpt), which is the main funder of my PhD position.

Acknowledgements

I want to give thanks first to the institutions, funds and network that have sponsored and made possible my doctorate studies. These are the European Training Network ColOpt, funded by the European Union Horizon 2020 program under the Marie Sklodowska-Curie Action, Grant Agreement No. 721465, the University of Glasgow, the Holoeye Photonics company and all the other institutions and members of the ColOpt training.

On a more personal level I thank all the people involved in ColOpt which have made an egregious effort in setting up a productive and welcoming environment to discussion and collaboration, and a special mention must go to the head of the network Thorsten Ackermann. At the same time I want to thank all of the members of the Optics group in Glasgow that I have met during the years which have realized the same kind of positive environment to encourage academic research during my years there.

I want to share my gratefulness to all the collaborators that have worked with me in the various projects, from the students to the postdoc. In particular I want to thank Neal Radwell, Thomas Clark, Adam Selyem, Jinwen Wang which have been crucial to my success in the everyday work activity in Glasgow as well as in the publish of scientific articles.

Finally I want to express my deepest gratitude towards my supervisor Sonja Franke-Arnold. Without her as a guide and mentor I would have surely lost the way during the perilous voyage of my doctorate. I can not really express in words how she has been helpful and patient with me and I count myself lucky to have had her as a supervisor.

Declaration of Authorship

I hereby declare that this thesis is the result of my own work at University of Glasgow and other institutions between June 2017 and December 2020, except where explicit reference is made to the work of others, and has not been presented in any previous application for a degree at this or any other institution.

Francesco Castellucci

Publications

The following is a list of papers where I am either first author of co-authored during my Ph.D.

- Castellucci, F. and Clark, T. and Selyem, A. and Wang, J. and Franke-Arnold, S. 'An atomic compass – detecting 3D magnetic field alignment with vector vortex light' Phys. Rev. Lett. 127, 233202 (2021).
- Wang, J. and Castellucci, F. and Franke-Arnold, S. 'Vectorial light–matter interaction: Exploring spatially structured complex light fields' AVS Quantum Science 2, 031702 (2020).
- Gao, S. and Speirits, F. C. and Castellucci, F. and Franke-Arnold, S. and Barnett, S. M. and Götte, J. B. 'Paraxial skyrmionic beams' Physical Review A 102, (2020)
- Qiu, S. and Wang, J. and Castellucci, F. and Cao, M. and Zhang, S. and Clark, T. W. and Franke-Arnold, S. and Gao, H. and Li, F. 'Visualization of magnetic fields with cylindrical vector beams in a warm atomic vapor' Photonics Research 9, 2325 (2021)

Contents

List of Figures

Chapter 1

Introduction

Light is one of the best tool at the disposal of scientists to investigate the universe around us. Much of the earlier experiments [1, 2] and observation of the physical world [3] relied on light. In more modern times coherent sources of light such as lasers are imperative elements in many setups. Cameras and photodiodes are also essential instruments for measuring and collecting experimental information. The vast majority of uses for all these instruments are focused on the analysis of the most obvious aspects of light: color, i.e frequency, and intensity. Maybe this is in part due to the fact that our own human light detectors, the eyes, are able to characterize those two aspects of light. However we are missing something, which we might not have missed if hypothetically we had the same ability to perceive light as bees [4] or cuttlefish [5] do. Polarisation, i.e. the direction of oscillation of light fields, is in fact a fundamental aspect of light propagation. In the interaction with matter, all three aspects, frequency, intensity and polarisation, need to be taken into account, as the outcome of the interaction can change radically by modifying just one of them.

So it should come naturally that the next step in our line of reasoning, is to include the variation or structuring of light. This notion is well understood in the Optics group at the University of Glasgow lead by Prof. Sonja Franke-Arnold and Prof. Miles Padgett. The group possesses an established notoriety in the field of structured light. In particular we have focused our investigative efforts on the study of the interaction of structured light with atomic gases. For myself, having a background on atom optics [6], it was a challenge at first, as I was not well versed in the techniques used to generate structured light, but thanks to the experts in my group I caught up quickly enough to the necessary level of

knowledge to handle the setups properly. In Chapter 2, I discuss about this aspect of my research. At first is crucial to say what we intend with structured light and the notation that we use to describe it formally: the Jones and Stokes notations (Sec. 2.1).

After that, the discussion will deal with the generation of structured light (Sec. 2.2) and the phenomena of dichroism and birefringence (Sec. 2.3), that underline the optical elements involved in those setup responsible for the handling of vectorial light. Over the last decades, the generation and use of vectorial light fields with complex and spatially varying polarization profiles has developed into an active research area as the possibility to design complex vector light fields now allows the full exploration of vectorial light-matter interaction [7]. Regarding the methods, there is ample choice when deciding how to generate arbitrary light beams [8]. The DMD is one of the more flexible instrument in that regard and in our group we have come to favour the DMD setup described in Sec. 2.4, has it is a method that offers complete control in the ability to generate arbitrary polarisation and amplitude profiles for light fields, while also maintaining a relatively simple design with a low number of optical elements. At the end of the chapter I will also discuss two of the optical experiments in which I was more involved and which revolved exclusively around the study of structured light and related themes. The first of them is the experimental realization of a light beam with skyrmionic properties (Sec. 2.5). The second experiment instead was on the possible use of structure light to measure the surface depth of an SLM (Sec. 2.6), and it was carried out at the Holoeye Photonics company in Berlin. This analysis was quite an unexpected experience, but also a welcomed one, in my idea of a research doctorate. The idea, objectives and methodology that characterized this feasibility study, as well as the environment in which it was performed, are more closely associated to the technological developments for industrial R&D. A testament to the interlinked nature of the academic and industrial research for the possible application of structured light.

However the main project in which I was involved in and that I delved most of my time during the Ph.D. was focused on the study of the interaction between structured light, cold atoms and magnetic field. In particular the main goal of the experiment was to detect 3D magnetic field alignment with vector vortex light through the absorption by atoms [9], in essence to realize an atomic compass. The role of external magnetic fields on the absorption of vectorial light fields by the atomic medium was investigated,

and we concentrated on the retrieval of information about the 3D alignment of a magnetic field, which was deduced from a single absorption profile of a vector vortex beam. Atomic gases are, in general, optically active media with a highly sensitive and nonlinear external field response, making them ideal candidates for magnetometry [10–13]. Atomic magnetometer setups have been designed and developed to detect magnetic gradients [14], the various components of the magnetic vector field [15–17], or to compensate magnetic backgrounds in 3D [18]. In the typical atomic magnetometers, optical pumping is used in order to observe the coherent Larmor precession of polarized atomic spins in a magnetic field, whereas vector magnetometers may employ radio-frequency modulation to map the vector components onto different harmonics. Another kind of atomic magnetometers employs the coherent interaction between atoms and photons to obtain electromagnetically induced transparency (EIT), electromagnetically induced absorption (EIA) and coherent population trapping [19,20]. These processes can be interpreted as a consequence of quantum interference – they are based on the fact that an optical field can transform atomic states such that an atomic transition can be entirely suppressed and subsequent absorption eliminated. Quantum interference shows an exceptional sensitivity to frequency shifts, including those induced by magnetic fields.

The full vector nature of a magnetic field may be accessed by simultaneously probing the magnetic field in orthogonal directions by separate probe beams. Alternatively, adding an external transverse magnetic field (TMF) can make EIT-based methods sensitive to different magnetic field components by considering polarization rotation or resonance amplitudes [21, 22]. The magnetometry setup that we developed belongs to this category of EIT based atomic magnetometers which combine the optical pumping present in EIT with the vector nature of the spatially varying polarization profile of the probe. Rather than setting a comparison in terms of performance and sensitivity, this study for a novel scheme of magnetometry had the goal to demonstrate a fundamentally different approach to optical magnetometry, passing from a measurement based on a time evolution to a spatially resolved detection of the magnetic field by analyzing the atomic response to vector vortex light.

To tackle all the necessary knowledge that need to be presented to understand and appreciate all the various aspect of the magnetometry experiment, in the process of making this thesis I decided to divide the discussion into three main chapters. The first of these

chapters (Chap. 3) is going to be an extensive description of the experiment "making" or Ποίησιζ. In this chapter I will first show all the additional aspects of light handling (Sec. 3.1) that are necessary in an atom optics setup which is much more complex and extensive than the ones discussed in the "light only" chapter. This aspects go from the generation of laser light with a diode in an external cavity (Sec. 3.1.1) to the detection of light frequency in relation to the atomic transitions of Rb (Sec. 3.1.2), how to lock the frequency to them with a lock-in system (Sec. 3.1.3) and how the AOM are used to control and fine tune the experimental light (Sec. 3.1.4). All these techniques are going to be crucial for the next topic which is going to be discussed, the atom trapping (Sec. 3.2). The relatively recent field of cold atom optics is in fact the product of various experimental methods that use light together with the magnetic field to trap atoms at cold temperature. The technique known as the MOT (Sec. 3.2.1) is the first stage of cooling that we apply in our experiment. This experimental method combines the radiative cooling through laser light with a magnetic potential, realizing a trap for the atoms. Thus a crucial aspect of the setup is the discussion about how the magnetic field is generated (Sec. 3.2.2). Furthermore, since the main result of our experiment is the measurement of the magnetic field, it should not be a surprise that an additional degree of care and attention needs to be allocated to the compensation of the background magnetic field (Sec. 3.2.3). In particular, this aspect of the experiment is the one to which I personally have struggled during the Ph.D., as it was crucial to avoid systematic error in the magnetometry data. Structured light makes a first proper appearance in the experimental setup in the SpOT (Sec. 3.2.4), as we trap the atoms in a dark state to be then excited by our probe, which is also of course a vectorial beam. In Sec. (3.3) I discuss the optical device called Q-plate and how it is used to generate the vector vortex probe beam that interact with the atoms in the experiment.

In the next chapter (Chap. 4) of the thesis, which is also called Θέσιζ, I delve in the theoretical discussion on the light-atom-magnetic interaction. First I present an overview on the particular atomic structure of ^{87}Rb (Sec. 4.1) as this is the element that is used in the experiment. Then I talk in general of the interaction between light and atoms starting from the simpler, although useful, two level atom case (Sec. 4.2) and introducing all the different theoretical notations and definitions like the Hamiltonian and the density matrix. Then I gradually increase the complexity of the model system by adding additional levels

(Sec. 4.3), which introduce new effects such as the EIT and optical pumping, as well as adding the magnetic field interaction together with the now familiar complex structured light (Sec. 4.4) which implies that the interaction is now locally varying across the profile of the beam and depends strongly from the alignment of the magnetic field. In the end of the chapter I show the practical *Fermi's Golden Rule* (FGR) (Sec. 4.5) model that was developed in my group to encompass all those aspect of the interaction and predict the absorption of the probe light by the atomic ensemble.

In the final chapter (Chap. 5) called $\Sigma\acute{\upsilon}\nu\theta\epsilon\sigma\iota\zeta$, I indeed synthesise all the arguments discussed in the previous chapters and analyse the data obtained from the various set of experiments. I begin by presenting the experimental procedure, detailed step by step(Sec. 5.1) as well as I report the experimental parameters in which the data was obtained. Aspect of this procedure include the size and density of the atomic cloud, the variation of the magnetic field alignment, which classify the two types of dataset that we acquired. I also present the polarisation profile, the intensity and the related Rabi frequency of the probe beam that was used and end the discussion on the procedure by exposing the actual making of the data through the absorption imaging technique. The concrete analysis of the data (Sec. 5.2) is a process that starts from the processing of the images through the extrapolation of the Fourier spectrum that is needed to confront the absorption with the prediction made with the models. Finally I present the results (Sec. 5.3) that we published in [9] as they are the ultimate product of the whole experiment and the ideal ending point of the main research. In the next section (Sec. 5.4) after that I present a similar yet different experiment [23] made by our collaborators at Xi'an Jiatong University, where the different approach on the magnetometry is taken by dealing with hot atoms and on other level system than the one used in the main Glasgow experiment.

Chapter 2

Vectorial Light matter interaction

The field of optics is one of the most important fields in the history of physics. From the earlier proposals on the wave nature of light in the 17^{th} century, to the elegant formulation of Maxwell equations, which unified the previous laws and formulas devised at the time, it was assumed that propagating light needed to be described as a vector, with strict properties on the relations between the different components.

One of the most relevant effect of the vector nature of light is its role in explaining all the physical systems that involve interference in one of its many guises such as diffraction, scattering and, most relevant for the field of atom optics, the interaction with matter possessing polarisation sensitivity.

Most importantly the experimental field of atom optics would not exist without the ability to construct the polarisation structure of light beams, not only for the most recent advances in the quantum optics and exotic states of matter but also for the earlier experiments before of the advent of lasers, due to the selection rules that characterize optical transitions between atomic levels [24].

Nevertheless the research area focused around the interaction of vector light with matter, and specifically atomic gases, is quite young and only recently has attracted the attention of the research community. One of the possible explanation for this late involvement might be due to the perceived separation between the field of optics, and the experimental groups working in the field, with the community of matter. The recent reunion between this two fields has been started with the advent of atom optics and continues now with atom "vectorial" optics [7], mostly in the semi-classical regime. The interaction however is relevant for full quantum application, e.g. quantum information network. In fact, as the

light is the best carrier of quantum information, being relatively easy to produce and read, the atoms would be the natural storage for this quantum information [25,26]. Additionally atoms are intrinsically active optical elements: while they interact and change the vector structure of a light beam, they correspondingly get modified by the optical beam, in their state populations and coherences, ultimately bringing about the entanglement of optical and atomic structures. These processes are also strongly non-linear, since they intensely depend on the frequency of atomic resonances, which can be altered by the application of external magnetic fields.

As a matter of fact is pretty much mandatory to think about atomic transition in tandem with the vectorial nature of light. The electric dipole interaction, which is the most important contribution in light-atom interaction, explicitly depends on the reciprocal alignment of the atomic dipole and the polarisation of the optical field. This mechanism is the first and foremost cause for the selection rules and the strength of an atomic transition. With the knowledge of this, it should come to no surprise the importance of the polarisation in the realization, manipulation and detection of the atomic states. This is true for both incoherent processes, e.g. optical pumping, as well as in the processes erecting coherences between several atomic states, e.g. *Coherent Population Trapping* (CPT) where the interaction between two different optical transition involving a common state induce the formation of a dark state for the light [27–29] or *Electromagnetically Induced Transparency* (EIT) [30–32], which is a similar process that usually refers to the system where there is an imbalance in the intensity of the two beam, with one acting as a pump while the probe is where the transparency is observed.

In the earlier definition and experiments on the topic of structured light, the term was limitedly referred to the modulation of the intensity profile of a light beam which was obtained through manipulation of the amplitude by subtraction, i.e. filters. In the later iterations there was an expansion of the meaning to encompass more complexly tailored amplitude profiles, which was made possible in a programmable, and thus easier manner, mainly due to the implementation of diffractive optical elements such as *Spatial Light Modulators* (SLMs) [33] and *Digital Micromirror Devices* (DMDs) [34–36]. Examples of well known modes that can be generated are the *Laguerre-Gauss* (LG) or Bessel beams [37,38]. These modes are found in many scenarios of light propagation but were impractical to realize, especially the ones in the higher relevant orders, until the advent of the above

mentioned devices.

2.1 Describing light as a vector. Jones and Stokes vectors.

Light can be described as a transverse vector field with two independent polarisation components. I acknowledge that light can also be polarized in the longitudinal direction, i.e. the direction of propagation, for specific cases and in different waveguides, e.g. strong focusing [39]. That said we will limit our discussion on paraxial light beams. In order to completely control the vector components, it is necessary to modify the complex amplitudes of each orthogonal polarisation independently [8, 40]. When this condition is achieved it uncorks the access to all kinds of spatially varying polarisation states, from the simpler radial, azimuthal or spiral [41], hybrid polarization [42,43] to the full Poincaré beams [44–48] with no limit to the customization of the design [49–58], except the general constraints of the Maxwell equations[1]

The general formulation of a paraxial vectorial light beam can be written as

$$\mathbf{E}(\mathbf{r}_\perp) = \begin{pmatrix} E_H(\mathbf{r}_\perp)e^{i\phi_H(\mathbf{r}_\perp)} \\ E_V(\mathbf{r}_\perp)e^{i\phi_V(\mathbf{r}_\perp)} \end{pmatrix}, \tag{2.1}$$

where $E_{H,V}(\mathbf{r}_\perp)$ and $\phi_{H,V}(\mathbf{r}_\perp)$ are the spatially varying amplitudes and phases, respectively, of the two orthogonal polarisation components, e.g. horizontal and vertical. $\mathbf{r}_\perp = (x, y)$ marks the transverse position, while it is implied that $\hat{z}$ is the propagation direction. We already hinted at the liberty of choice for both the amplitude and phase in terms of the spatial profile. Thus we can omit the explicit dependence on the position. Hence the modified equation can be rewritten as

$$\mathbf{E}(\mathbf{r}_\perp) = E_0 e^{i\phi} \begin{pmatrix} \cos(\theta) \\ \sin(\theta)e^{i\,\chi} \end{pmatrix}, \tag{2.2}$$

to enhance some aspects of the physical interpretation. $E_0 = \sqrt{E_H^2 + E_V^2}$ represent the

[1]These constraints usually translate in the fact that a completely arbitrary polarisation and intensity profile can be generate only on one small segment of the propagation path. In other words all kinds of arbitrary beams can be generated but only some are properly propagating beams.

position dependent total amplitude of light, $\phi = \phi_H$ is the overall spatially varying phase. This representation of light is the one known as Jones vector.

The last factor is the local polarisation vector, determined by the two parameters $\chi = \phi_V - \phi_H$ which is the relative phase or ellipticity between the two polarisation and the orientation relative to the horizontal axis θ which derives from the amplitude ratio as $\tan\theta = E_V/E_H$. Something that should be kept in mind is that there is no constraint on which couple of orthogonal polarisation to use as a basis, in fact it is very advantageous to select the basis that best adapt to the problem at hand. As an example, it is usually preferable to use the two circular polarisations as a basis when dealing with atomic transition, since the spin selection rules discriminate between these two polarisations. On the other hand, in optical communication systems the basis used is usually linear since some optical elements used in these schemes, such as polariser and beam splitters, are designed to absorb light of the linear polarisation aligned with the instrument optical axis[2] [59].

Another popular way to represent the polarisation is to measure the Stokes parameters and construct the Stokes vector of the light. The four parameters of the Stokes vector are

$$\mathbf{S} = \begin{pmatrix} S_0 \\ S_1 \\ S_2 \\ S_3 \end{pmatrix} = \begin{pmatrix} I \\ H - V \\ D - A \\ R - L \end{pmatrix}, \tag{2.3}$$

where I is the total intensity of the beam, H, V, D, A, R, L, are horizontal, vertical, diagonal, anti-diagonal, right circular and left circular polarisation intensities respectively. In the case of fully polarized beam we have

$$\frac{\sqrt{S_1^2 + S_2^2 + S_3^2}}{S_0} = 1 \tag{2.4}$$

and the Stokes and Jones representation are equivalent. It is customary to normalize the vector by dividing the coefficients with total intensity I. By doing that and neglecting ${S_0}^3$, we can plot a vector with the remaining coefficient which lays in the Poincaré sphere. In the case of fully polarized beam the vector reach the surface of the sphere while for

[2]Of course circular polarisations are still used in many optical communication experiments and setups. It is only unusual to see the right and left polarisations as the light polarisation basis.

[3]Note that this is always equal to 1 after normalization.

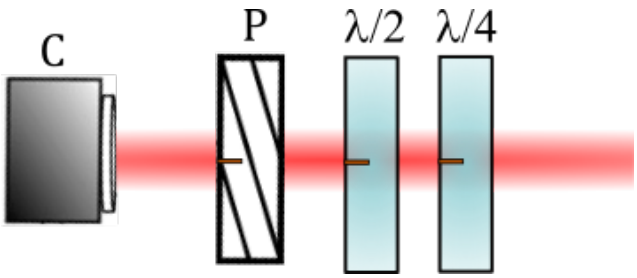

(a)

Polarisation	$\lambda/4$	$\lambda/2$
$\|H\rangle$	0°	0°
$\|R\rangle$	0°	22.5°
$\|V\rangle$	0°	45°
$\|L\rangle$	0°	67.5°
$\|A\rangle$	45°	67.5°
$\|D\rangle$	45°	22.5°

(b)

Figure 2.1: Stokes measurement scheme. The light passes through a quarterwaveplate ($\lambda/4$), a halfwaveplate ($\lambda/2$) a polariser (P) and is then recorded on the camera (C). In order to measure the 6 different polarisations the waveplates optical axis are oriented according to the angles shown in the table (b), while the polariser is kept fixed. In the scheme is shown the configuration to measure H.

unpolarised light it would lay inside. Fully unpolarised light, like the one coming from the sun, would be at the center of the sphere shown in Fig. 2.2 (a). The proper measurement can be done with a photodiode to measure all the different intensities listed in Eq. 2.3. However, using a photodiode has the disadvantage of integrating the whole signal, thus in the case of a beam with local polarization variation, it is better to acquire images of the 6 base polarisations with a camera. And actually to reconstruct the Stokes vector only 4 independent polarisations would need to be measured[4], but for simplicity it is sometime easier to measure all of them. In principle it is possible to measure all different base polarisations by rotating only two optical elements, a polariser and a quarterwaveplate. However this solution, perfectly fine in the case of homogeneous beams, is less than ideal for beams locally varying polarisation. This is the case because polarisers can refract light if their surface is not perfectly orthogonally aligned to the propagation axis[5]. Thus this can induce errors in the measurement when confronting the 6 different images to reconstruct the polarisation profile. Instead, in the setup that has been favoured by us the optical axis of the polariser is kept fixed and a halfwaveplate is added to obtain the necessary measurement. A scheme representing this setup is shown in Fig. 2.1. It is also possible to automatize the acquisition of the 6 Stokes measurement by placing a rotor on the waveplates, the rotation of which can then controlled remotely with a PC [60]. In our lab we have used this technique in various experiments [61–63] and has also been used by

[4]The number of degrees of freedom in Eq.2.2.

[5]Even if the alignment is perfect at the start of the measurement, there is an high probability of losing it since it will be needed to be rotated during the measurement.

me during the research shown in Sec. 2.6.

2.2 Generation of Vectorial Light Beams

There are many methods that have been developed for the goal of generating structured vector fields. These methods can be broadly categorized in two main classes. One class focuses on the generation of specific preset modes while the other provides flexible arbitrary modes generation. In the former can be found all the methods involving optical passive elements characterized by birefringent or dichroic properties, like plasmonic metasurfaces [64, 65], Fresnel cones [66, 67], s-plates and q-plates [68, 69], with the last being the vector beam source in our main experimental setup. All these methods tends to be highly efficient at generating the specific set of modes which they are engineered to shape. This of course is also their limiting factor as they are restricted to those specific subset of 2D modes in the otherwise infinite-dimensional spatial state space that encompass light propagating modes. As a typical example, it can be used in the generation of modes

$$E \propto e^{i\phi}\hat{\sigma}_- + e^{-i\phi}\hat{\sigma}_+, \tag{2.5}$$

where ϕ denotes the azimuthal angle, and $\hat{\sigma}_\pm$ are the two circular polarisation states. Furthermore, to extend the accessible state space and allow the manipulation within this subset, standard polarisation optics can be used thus providing for radial, azimuthal, hybrid and spiralling polarisation states. In many of these cases though the obtained modes are not eigenmodes of free propagation, thus requiring for the experiments to be performed in a limited image plane.

On the contrary, the generation of arbitrary structured vortex beams depends upon the independent manipulation of the complex amplitudes of two orthogonal polarisation, e.g. horizontal and vertical. And as an additional requirement, the manipulation of the amplitudes must not reduce the transverse coherence of the light field too much. Or in other words the relative phase between the two polarisation needs to remain defined. The two instruments associated with these technique are the programmable SLMs and DMDs placed within an interferometer configuration [34, 70–73]. The property of being controlled and programmed by software allows for on-demand and real-time arbitrary vector light

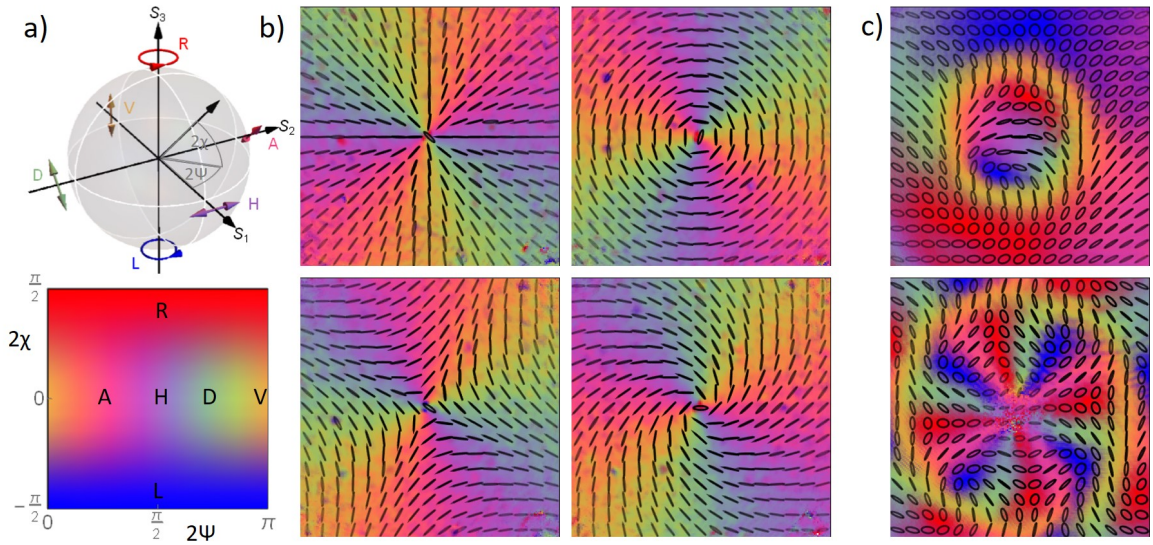

Figure 2.2: Vector beams polarisation structure. a) polarisation Poincaré sphere and the associated color legend, which associates each of the base Stokes vector states, (Horizontal, Vertical, Diagonal, Antidiagonal, Right and Left) to a unique color. b) Experimental images of radial, azimuthal and two hybrid spiral polarisation, made with a DMD setup as illustrated in Sec. 2.4. These polarisation structures together with homogeneous right and left circular polarisation, could be used as an alternative basis to the more widely used Stokes vector basis. c) two examples of experimental Poincaré beams, i.e. propagating beams that contains all the polarisations spanning the complete Poincaré sphere. Image taken from [7].

fields structuring and modification [74], with the limitation given by their specific spatial, which is higher for SLMs, and temporal, which is faster for DMDs, resolutions. The price for this vast degree of flexibility comes with their relatively low efficiencies, thus are more commonly used in the context of classical beams rather than in quantum optics environments, e.g. single photons experiments.

In Fig. 2.2 is shown an ensamble of polarisation structures experimentally realized with the method shown in Sec. 2.4. In a) is shown our choice color legend to display light polarisations with the symbolism of the Poincaré sphere, and its connection towards Stokes vector representation. The four polarisation patterns depicted in b) are a subsection falling in the modes group of the LG family that have the general form of

$$\mathbf{u}_p^\ell(r,\phi,z) = C_p^\ell \frac{w_0}{w(z)} \left(\frac{r\sqrt{2}}{w(z)}\right)^{|\ell|} \exp\left(-\frac{r^2}{w^2(z)}\right) L_p^{|\ell|}\left(\frac{2r^2}{w^2(z)}\right) \times \tag{2.6}$$

$$\exp\left(-i\kappa\frac{r^2}{2R(z)}\right) \exp(-i\ell\phi) \exp(i\psi(z)) \tag{2.7}$$

where w_0 is the Gaussian waist of the beam at $z = 0$, $w(z)$ is the beam width respectively, $R(z)$ is the radius of curvature and $\psi(z)$ is the Gouy phase and are the typical parameters that define a Gaussian beam. In addition here we have the generalized Laguerre polynomial $L_p^{|\ell|}$ and the normalization constant $C_p^{|\ell|}$. The modes present in the figure are formed by $LG_p^\ell = LG_0^0$ and LG_0^2. The resulting polarisation are equivalent to the more widely known radial, azimuthal, and hybrid polarisation canonically obtained from the superposition of $LG\pm 1_0$, but for a difference in the absolute phase term $\exp(-i\phi)$. In fact the shown beams carry a net amount of OAM per photon, in contrast to the latter case in which the OAM is balanced. That is to point out that within the contest of structured beams, the OAM carries an ulterior degree of freedom in addition to the one derived from the polarisation profile. The last two images in c) are two examples of Poincaré beams, i.e. beams that range over all the polarisations present in the Poincaré sphere effectively mapping it onto the beam transverse profile. These were built by the superposition of $LG_0^1\hat{H} + LG_1^{-1}\hat{V}$ on top and $LG_0^2\hat{H} + LG_1^{-3}\hat{V}$ on bottom.

2.3 Phenomena for light manipulation: dichroism and birefringence

Many materials used in a structured light setup and in the general optics lab environment base their properties on either of these effects: dichroism and/or birefringence. Dichroism refers to the differential absorption in a material of two orthogonal polarisations of light, relatively to orientation of the optical axis of the material. Instead the birefringence, which is the presence of two[6] refractive indices on different optical axes of the material. The polarisations aligned with these optical axes travel with different phase velocity modifying the relative phase between the polarisations.

Historically[7] both of these effect where first discovered and described in the context of homogeneously polarized light beams. However they acquire a much higher potential number of applications when applied in the context of light with a structured polarisation

[6] At least.

[7] The discovery of birefringence in calcite was crucial to allow the navigation of early Scandinavian populations across the northern seas, were the sun is usually shrouded by cloud cover and in a historical period precedent of the development of the first magnetic compass. It was first scientifically described by the Danish scientist Erasmus Bartholin in [75].

profile. Both these effect can occur naturally in materials, due to their peculiar crystalline structure, or can be induced by the action of external forces, e.g. mechanical stresses, external electromagnetic fields or a combination of both. The materials that manifest naturally this kind of anisotropy are the core ingredient for the production of the polarisation optics elements of the passive kind, e.g. polarisers (dichroism) and wave retarders (birefringence).

Between the various materials with polarisation altering effects, liquid crystals have taken prominence for their versatility in the manipulation of vector light field, being the constituent part of SLMs and q-plates. Q-plates are optical elements with spatially varying birefringence. Their main use is to interchange between the spin and orbital state of light, since the particular phase retardation induced by the birefringence affects the circular polarisations causing the formation of a corked phase front (starting from a flat one) which is commonly associated to OAM.In other words q-plates are like waveplates where the induced phase delay between the polarisations is dependant on the azimuthal position of the instrument and varies continually which adds up after one loop around the center to $2\pi\ell$. The q number corresponds to the quanta of phase delay built in the liquid crystal strata[8], converting into OAM quantum number with a ration $\ell = 2q$. For this purpose of OAM generation, we use one of the q-plates in our main experimental setup as described in Sec. 3.3.

However, the materials which is studied in many experiments for its polarisation sensitive anisotropies are atomic media. Atoms are inherently isotropic, but when under the effect of external fields, such as magnetic fields or when optically pumped the atoms can lose their isotropic nature and show all the properties that we mentioned before such as dichroism and birefringence. Hence it is usually advantageous when modelling these systems to select the quantization axis that are correspondent to either the direction of propagation, or the polarisation of those external fields. These effects find application in atomic magnetometry [12,76–78] and polarisation sensitive absorption spectroscopy[9] [81–84]. Optical pumping experiments usually involve a strong pump laser to induce the anisotropy in the atoms in the form of a spin alignment of the atomic gas. This is followed by the

[8]Not dissimilar to the naming convention for quarter waveplates and half waveplates, that induces a delay of $\lambda/4$ and $\lambda/2$ respectively

[9]Molecules, some of which possess higher degrees of anisotropy, can also been used in these contexts [79, 80].

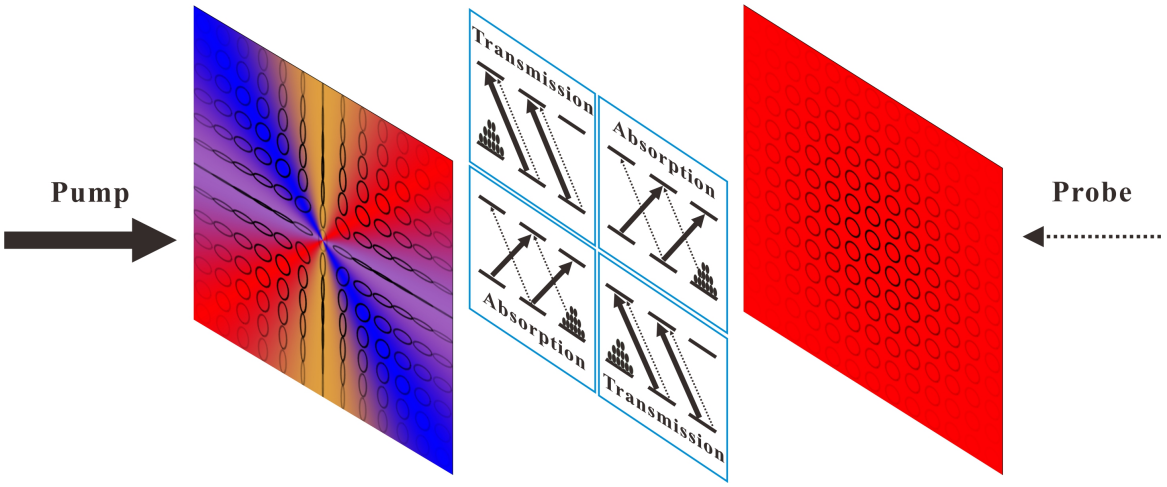

Figure 2.3: Inhomogeneous dichroism in an atomic medium induced by a spatially structured pump light beam. When atoms are exposed to a pump beam with spatially varying polarisation (left), optical pumping, thus atomic states populations, differs locally. The spatially varying atomic population distributions (center) can then be probed by a weak uniform (counter propagating) beam (right). In areas where the polarisation of the probe matches the one of the pump, i.e. the helicity in the reference system of the atoms are opposed, the probe is absorbed, whereas areas with opposite polarisation (same helicity) transmission is enhanced. This is defined as spatially dependent absorption spectroscopy. Image taken from [7].

investigation of various property of the medium with a weaker probe laser, that can be oriented in different ways in respect to the stronger beam. It is the polarisation of the strong pump that determines the spin alignment of the atoms. This in turn will influence the outcome of the interaction with the probe [85]. In general there are three kinds of optical transitions: if the spin quantum number does not change between the connected levels we have a π transition and it takes place when linear polarisation of the beam is parallel to the quantization axis of the atoms; instead when there is a change of $+1$ or -1 in the atomic spin, the transition are called σ_+ and σ_- respectively and they result from beams with linear polarisation, which is a superposition of $\sigma_\pm$ polarisations, perpendicular to the quantization axis [86]. To clarify optical polarisation is defined with respect to the beam's propagation axis, while atoms are sensitive to optical helicity defined with respect of their proper quantization direction. To summarize, optical pumping induces circular dichroism in the atoms, thus they behave like a polariser for circular light. This has a lot of potential applications since there is no optical element behaving like a single piece circular polariser.

Naturally, from homogeneous pump beams arise homogeneous dichroism. Of more

interest for us are polarisation-structured pump beams which cause in the atomic media a spatially varying dichroism. Such a case is shown as an example in Fig. 2.3.

As I mentioned above, the other external field that can cause anistropy in the atomic media is an external magnetic field. In general, from a magnetic field will arise a Zeeman shift in the hyperfine sublevels of the atoms, thus resulting in a difference in the transition frequency for the opposing σ transitions. This in turn will cause a difference in the refractive indexes for the two light polarisations, hence a phase delay and a kind of birefringence commonly known as Faraday rotation. The combination of circular dichroism and circular birefringence can be achieved with the combined action of structured light beams and magnetic fields [87] enabling in theory for the realization of an optical isolator for radially polarized light with a very narrow frequency window[10].

The concepts and notions mentioned in this section provide both a preview and a context for the idea behind the main *atomic compass* experiment highlighted in the rest of this thesis (Chap. 4 and 5).

2.4 Generating light beams with the DMD setup

In this section I will describe the DMD setup which is one of the most useful and well suited experimental system to generate arbitrary vector beams. As the name suggest the main element involved for this technique is the *Digital Micromirror Device*: this is a $2D$ array of μm-sized mirrors mounted on individual actuators that allow to orientate independently the micro mirrors in two different directions [88]. This "binary" reflection screen thus can act on the amplitude of a beam incident to the device, in contrast to the phase modulation typically associated to the SLM. The main use of the DMD is in *Digital Light Processing* or DLP technology for video projectors, since the higher rate of modulation (on the order of kHz) allows for a reasonably fast and high resolution video definition for a small device. Anyway this is not the properties that we require in our setup and the reason we are interested has more to do with what was said previously about the difference with the SLMs. In fact since the DMD affects directly the amplitude of the incident light, the surface can act on the light independently of the polarisation[11],

[10] Compare to conventional isolators and polarisers which are more broadband

[11] Unlike the SLM.

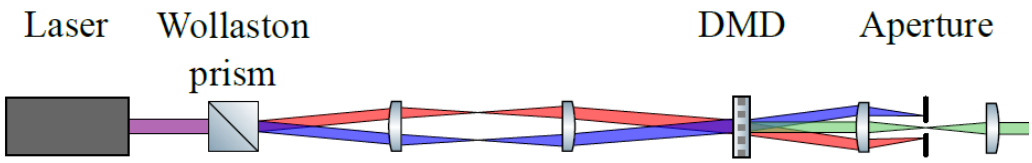

Figure 2.4: Polarisation shaping setup with a DMD. Diagonal light is separated by a Wollaston prism into a vertically and horizontally polarised beam. These are then focused on the DMD surface. Two overlapping diffraction orders can then be filtered from the others for use. Note that this image is a simplified scheme and the actual setup relies on a reflective grating. Image taken from [89].

it is possible to generate any polarisation pattern that can be written as a linear sum of two light beams with orthogonal polarisation[12].

The complete description of the setup, how the hologram are constructed and the procedure that underlines the generation of the various beams can be found in the technical paper [90] or in the Ph.D. thesis [89] of the former member of our group Ádam Selyem. Here I will present a brief overview on the principles on which is built on. The first thing to mention is that is not so easy to just reflect the desired amplitude and phase for each polarisation in a naïve way. The DMD surface is not wide enough that it can be used as two separate reflecting surface for the two beams that would then be overlapped on the image plain. Instead it is much more convenient to project two different diffraction grating mask on the whole semiconductor surface with a technique known as multiplexed grating. Those two independent grating will generate many diffraction orders[13] based on the profile of their parent diffraction hologram. From the high number of diverging diffraction orders, we select one from each of the orthogonally polarised beam and that are generated by the two different grating, filtering all the other orders. This means that after filtering we have two orthogonal polarised beams that have amplitude and phase dictated independently by the holograms that we generated, i.e. the linear sum of the two beams can generate arbitrarily any polarization structure that we need, as long as it does not violate Maxwell equations. The simplified scheme of the setup is shown in Fig. 2.4.

[12]And thus create any beam since the two beams form a complete base.
[13]In addition to the diffraction generated by the pixellation of the device.

2.5 Skyrmion project: Experimental application of the DMD setup

The flexibility of the DMD and the access that it provides to the mode space of vectorial beams found its use in many research projects [34, 62, 90] performed by the Optics group at Glasgow University. A project in which I was directly involved revolved around the possibility of realizing paraxial skyrmionic beams [91] with the DMD setup, which I want to give a brief outline here.

Skyrmions are a topological solution of a stable field for a certain class of non-linear equations [92, 93]. Here I do not want to delve too deeply into the particular properties of skyrmions or in which fields they have found their application. I will only limit the discussion to a general description of what is a skyrmionic optical beam and how such beam can be obtained experimentally with a setup like the one presented in Sec. 2.4.

Skyrmions can only be found in light fields if both the polarisation and the field amplitude are spatially varying, they are a subclass of the light fields being featured in the whole Chap. 2. In particular, it can be of interest to categorize the different Poincaré beams in different classes characterized by the skyrmion number [94].

By using the same Jones vector notation presented in Eq. 2.2 we can rewrite the expression of a paraxial beam as

$$|\Psi(\mathbf{r})\rangle = u_0(\mathbf{r})\,|0\rangle + e^{i\theta_0}u_1(\mathbf{r})\,|1\rangle\,, \tag{2.8}$$

where $|0\rangle$ and $|1\rangle$ are just any two optical polarisations that are used as bases, $u_0(\mathbf{r})$ and $u_1(\mathbf{r})$ are two orthogonal spatial modes and θ_0 is the phase difference between the two modes. The skyrmion field number depends only on the spatial variation between the two polarisations, so it is more convenient to rearrange the above equation as

$$|\Psi(\mathbf{r})\rangle = \frac{|0\rangle + v(\mathbf{r})\,|1\rangle}{\sqrt{1+|v(\mathbf{r})|^2}}, \tag{2.9}$$

where I have expressed $v(\mathbf{r}) = e^{i\theta_0}u_1(\mathbf{r})/u_0(\mathbf{r})$.

The skyrmion field can then be defined in terms of an equivalent magnetization $\mathbf{M}$ vector, which is also equivalent to the local direction of the Stokes vector as seen in Fig.

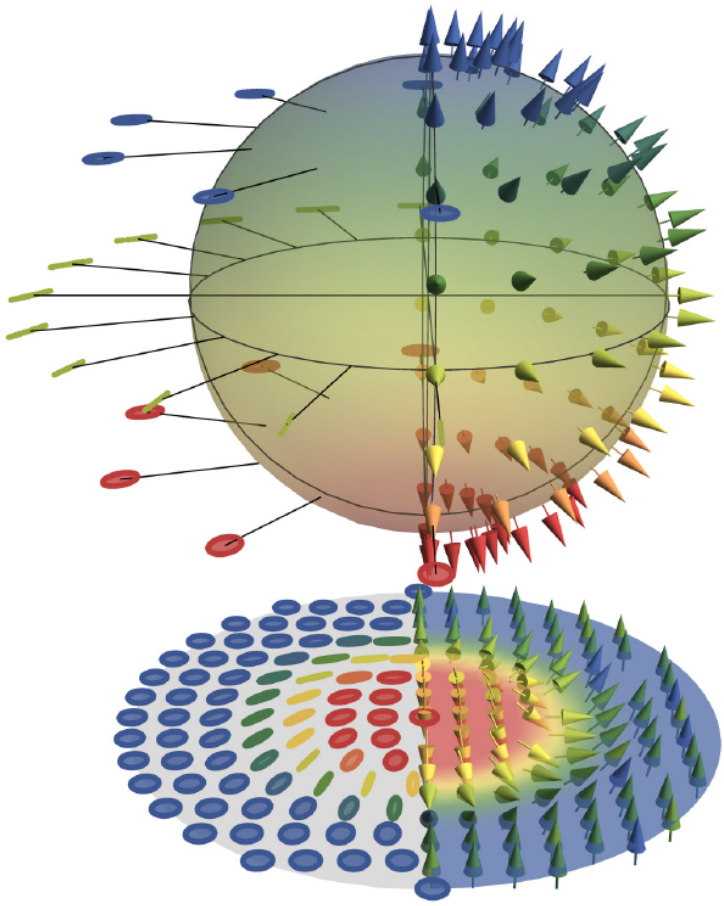

Figure 2.5: Stereographic projection of the magnetization onto the Poincaré sphere. The color scheme confront the S_3 component of the Stokes vector, i.e. ellipticity, and the z component M_z. Image taken from [91].

2.5. The relation between $\mathbf{M}$ and the light field is

$$\mathbf{M} = \langle \mathbf{\Psi(r)} | \, \boldsymbol{\sigma} \, | \mathbf{\Psi(r)} \rangle \, , \tag{2.10}$$

where σ a vector operator with the Pauli matrices as Cartesian components. Thus, in the case of a light beam, the Cartesian components of $\mathbf{M}$ correspond to the familiar Stokes parameters S_1, S_2 and S_3 introduced in Sec. 2.1. With this little definitions in mind I will stop the discussion on the technicalities and properties of skyrmions, referring the reader to [91] for more detailed information on the underlying theory, since I am not an expert on this topic. I rely more on the qualitative and visual analogy of the magnetization with the vector of the local beam polarisation, and for the vector vortex beam the skyrmion number will be the difference of handedness between the center of the beam ($|r| = 0$) and the external part of it ($|r| = \infty$) multiplied by their difference in angular momentum ℓ.

With this in mind it is easy to think of how to realize the simplest skyrmionic beams as a superposition of two orthogonal polarisations, each characterized by a spatial LG mode, with a common focal point and the angular momenta differing by an integer value $\Delta\ell$. After having selected the modes, as well as the other beam parameters, this will be translated as an hologram to be displayed on the DMD, obtaining the desired skyrmionic beam. A theoretical example of such a beam is shown in Fig. 2.6. In Fig. 2.7 is shown the experimental realization of such beam made with the DMD setup.

2.6 Holoeye project: SLM layer thickness measurement

In this section I will talk about the work done during my secondment in Germany. This work has nothing to do with atom optics, which is the main topic of my PhD project, but concerns more the application of polarized light, complex light fields and *Spatial Light Modulators* (SLM). From November to December 2018, I completed one of my period of study abroad in Holoeye Photonics. This is a company based in Berlin that specializes in the production of SLM and diffraction optics. There I investigated a novel scheme to deduce the surface layer thickness of an SLM device.

To better understand why this is important, it is useful to illustrate in short words how

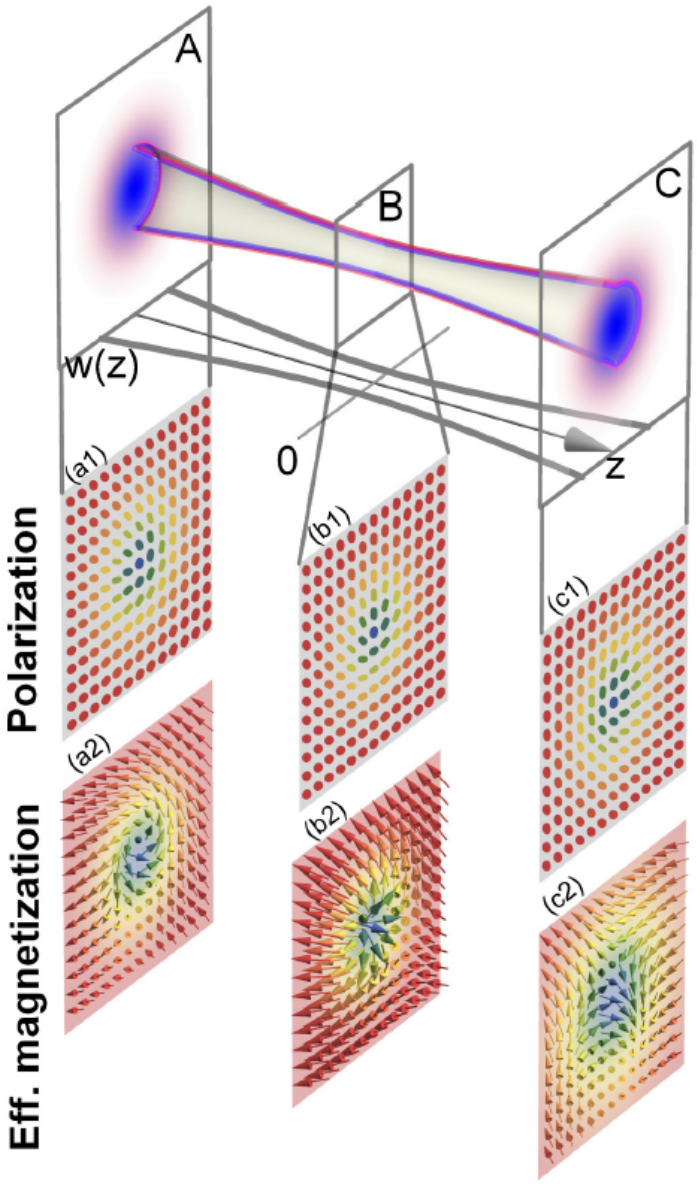

Figure 2.6: Polarisation structure for a superposition of LG modes with $\ell_1 = 1$ and $\ell_0 = 0$ focused at $z = 0$. The beam surface on top separates the regions in which the modes are dominant over the other, i.e. u_0 is stronger at the center (blue) and u_1 on the exterior (red). The three different cross sections are shown since the polarisation (a1, b1, c1) and effective magnetization (a2, b2, c2) vary significantly and are not symmetrical in respect to the focal point. Notice the typical chiral and "hedgehog" form of the magnetization field, typically associated with the skyrmions. Image taken from [91]

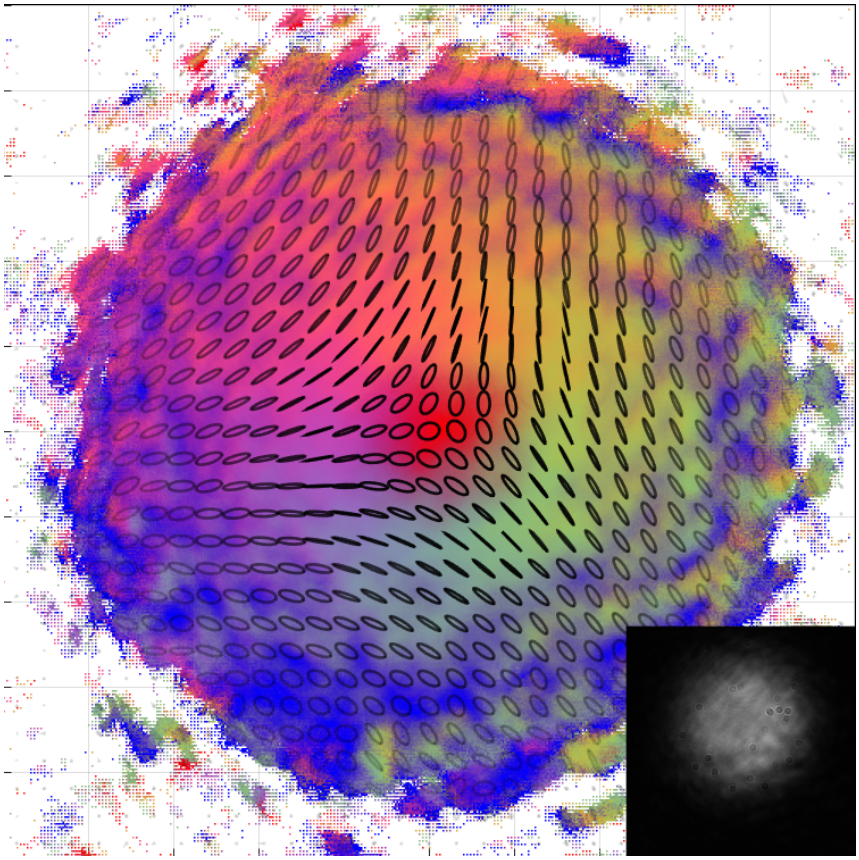

Figure 2.7: Polarisation structure of the experimental realization of a skyrmion beam. It is a superposition of orthogonal polarisations with LG modes with $\ell_1 = 1$ and $\ell_0 = 0$. In the inset is shown the intensity profile. Data taken by Amy McWilliam.

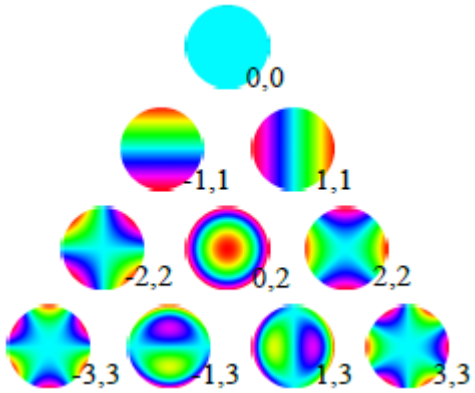

Figure 2.8: Zernike polynomials with indices n,m. Each of these polynomials can be identified with a particular kind of stress applied to a surface during fabrication. Thus the surface analysis on a stock of display could be used to correct any defective procedure involved. Image courtesy of Ádám Selyem.

an SLM works. SLM are either transmissive or reflective devices formed by a display filled with strata of liquid crystal chains. As mentioned briefly in Sec. 2.3, liquid crystals are birefringent materials, meaning that light passing through them will acquire a different phase depending on which axis the light is oscillating, i.e. the phase velocity of light is polarisation dependent in birefringent media. The display of an SLM, is divided in pixels which can be singularly controlled electronically by applying a DC voltage. The generated electric field defines the alignment of the liquid crystal chains and with this mechanism, SLMs spatially shape the phase of light beams [88].

To determine more quantitatively the phase delay induced by an SLM, which can also be called retardance, there are some factors to take into account other than the voltage applied by the user. These factor are mainly the layer thickness of the device, that due fabrication process is never perfectly flat (at least not at the nm level) and the voltage to electric field conversion on each pixel. The latter is the different electric field between pixels when the digital input voltage is the same. It has a stronger effect at the border of the device and thus can be mostly ignored by using just the central part of an SLM. On the other hand the difference of layer thickness characterize the whole surface and differs from one device to another. The aberrations which are caused by those factors can be described in terms of Zernike polynomials Z_n^m [95].The more common ones are the lower orders ones which can be seen in Fig. 2.8.

Taking account of these effects, in order to obtain the wanted phase and amplitude profile after the SLM, one should first apply a compensation mask which "flattens" the

phase surface of the SLM on top of the mask required for the desired beam. For the same reasoning, if we need a corrective mask to obtain a flat phase response from the SLM, by using no mask at all, i.e. using the SLM as a passive reflective object without even turning it on, a linearly polarized beam would acquire a phase profile that maps the layer thickness across the different locations of the display. This idea lead to the development of the experimental setup that I am going to describe. The first part of the setup comprises the light field preparation: from a He-Ne laser the beam passes from polariser1 to obtain diagonal polarisation $\mathbf{S} = (1\,0\,1\,0)$ where the horizontal and vertical axis are determined by the axis of the SLM display. The choice of the diagonal polarization as input is justified by the following consideration: since the refractive index has the biggest difference between the E_x and E_y components of the light field, when passing through the SLM the two component of the beam will acquire a phase delay, thus transforming the polarisation from diagonal to elliptical, depending on the local layer thickness. The beam is then filtered with a 10 μm pinhole. The pinhole has also the use of diffracting the beam to the desired diameter of 20 mm which is reached approximately after 20 cm. The final element of this first part is Lens1 ($f = 200$) which is used to collimate the beam. After this first part the beam is now larger, collimated and polarized and is going to fully illuminate the display. The angle of incidence θ should be measured since it is used in the estimation of the retardance. The second part of the setup is where the measurement of the polarization is performed, with the same Stokes measurement technique described in Sec.2.1. After the reflection on the display back surface [14] the beam coming from the display is focused by Lens2 ($f = 300$) and passes though the waveplates mounted on the rotation stages, with $\lambda/4$ being the first and then $\lambda/2$, and then passes through the polariser2. After these 3 elements the Lens3 ($f = 75$) is placed to form a telescope with Lens2 that collimates the beam before reaching the camera. Since the camera sensor is approximately 4 times smaller than the LC display, the telescope had a magnification factor $M = 0.25$. The setup is summarized in Fig. 2.9.

The retardance [96] between the two component of the electric field can be expressed as

$$\eta = \frac{4\pi\Delta n d}{\lambda \cos\theta} \tag{2.11}$$

[14]Note that the liquid crystal only reflect a small percentage of incoming light. This means that for reflective SLM, the light beam passes twice in the solution and the angle of incidence influences the optical lenght, hence the retardance.

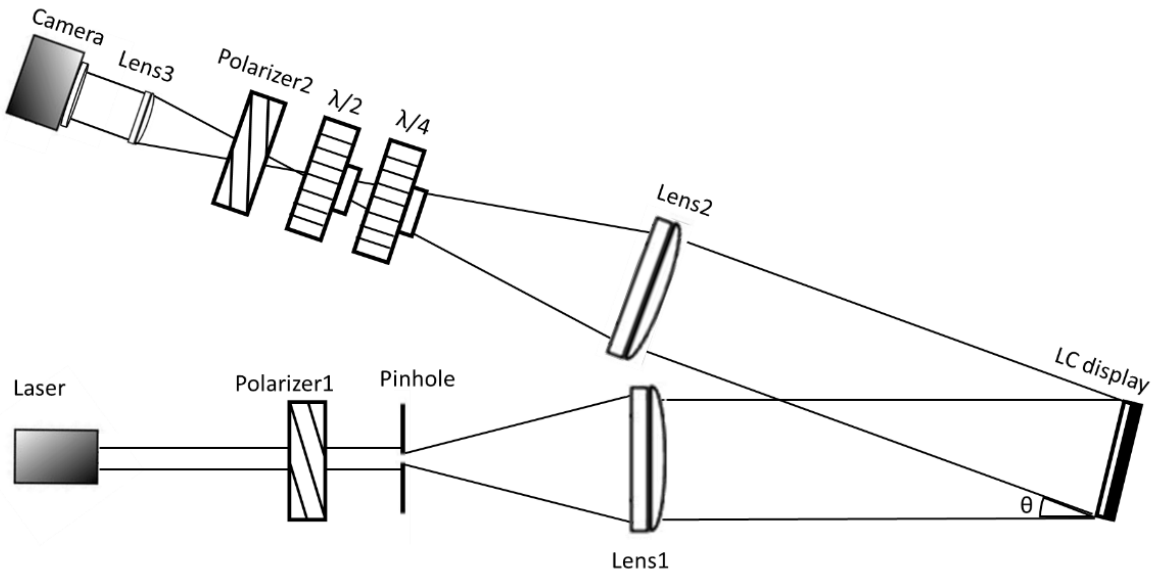

Figure 2.9: Experimental setup scheme for the measurement of the SLM layer thickness

where Δn is the difference of refractive index between the x and y optical axis of the display, d is the layer thickness, λ is the wavelength of light and θ is the angle of incidence. By plotting a map of the phase values on the different part of the display one can derive the difference in the layer thickness d. Is important to remember that the phase can have a value only between $[-\pi, +\pi]$. This means that whatever the value of the retardance the system will measure η mod 2π. Consequently the absolute value of the layer thickness can not be measured if the total retardance is bigger than 2π. Nevertheless the layer thickness variation is given by

$$\Delta d = \frac{\lambda \cos\theta \, \eta}{4\pi \, \Delta n} \tag{2.12}$$

which was used to generate the layer thickness map of the display on Fig. 2.10.

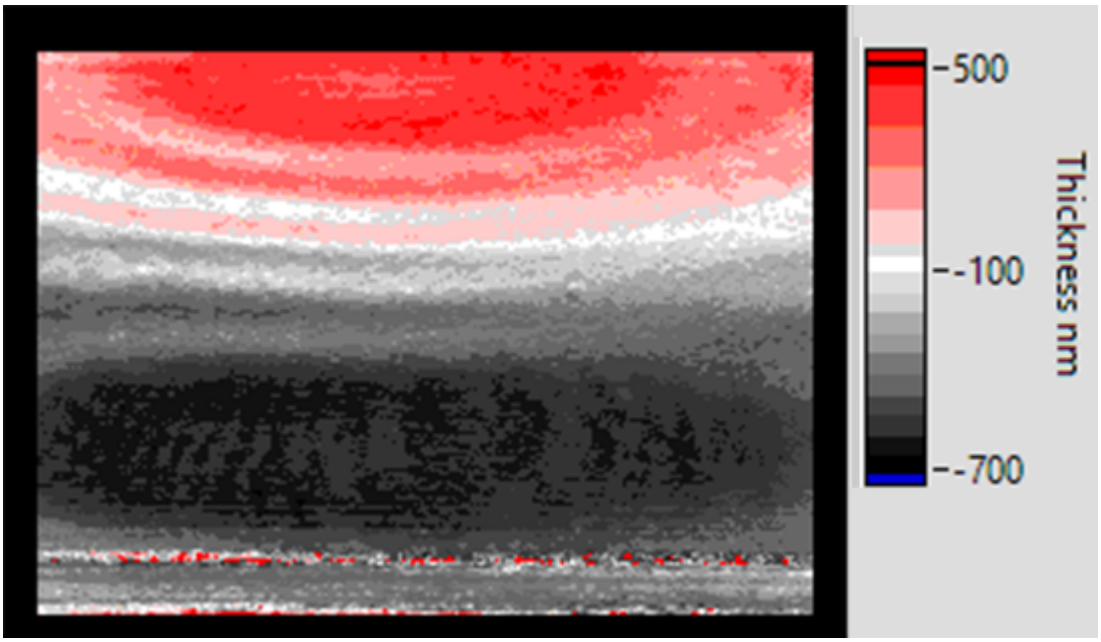

Figure 2.10: Example of layer thickness for a display 20×10 mm^2. Note that the 0 represents an actual layer thickness that would generate multiples of 2π phase delay, hence no retardance. The display in the image is mainly affected by a vertical coma kind of distortion.

Chapter 3

Ποίησις (Poíesis)

I decided to call this chapter *ποίησις*, which means "the activity of making something from nothing", as it nicely describes the practical experimental work carried out in the lab which is presented in this chapter. All of these techniques, systems and methods are well established either in the atom optics and wider optics communities worldwide. They can be easily found in review articles [97–100] as well as books [101, 102], hence are not uniquely developed in our experiment, unless stated otherwise. To help with the descriptive discourse of the chapter, I structured it as an ideal voyage of the light from the semiconductor gap of the laser diode to the chip of the camera, passing through the various stages of the experimental setup such as the saturated absorption used by the locking system or the diffraction grating of the Spatial Light Modulator (*SLM*). My intention with this chapter is to make the reader familiar with all the different techniques and aspects necessary to handle the experiment successfully, which was often the daily challenge for me and the other PhD students who worked with it, in the hope that this few pages would be useful for the future students operating the setup.

The bulk of the topics that will be discussed revolve around the necessity of "trapping and cooling" atoms. This is achieved mainly through the handling of laser light (Sec. 3.1). This particular aspect of the experiment, the precise selection of a narrow frequency of emission takes the prevalence in experimental techniques, electronics instruments and optical components, thus it can be considered one of the distinguishing trademark of an atom optics experiment. The other "field" of expertise that is required for trapping is the control of the magnetic field, which is discussed in Sec. 3.2 and more specifically 3.2.2. Furthermore, in the specific case of our experiment the manipulation of the light

and magnetic field goes even further the standard techniques employed in the atom optics community, both for our necessity of an uncommon kind of trapping beam shape (Sec.3.2.4) and the requirement for a vectorial electric (Sec.3.3) and keenly compensated magnetic (Sec. 3.2.3) fields employed in the actual execution of the experiment.

3.1 Laser light, creation and manipulation

In the first chapter regarding the experiment I will talk about the various aspect of laser light, which is one of the two main media used in our research [1]. Here I will describe the various techniques used in our setup, some of which are fairly common to a lot of other cold atoms experiments and others which are less widespread in that research area. Probably the most peculiar characteristic of cold atom experiments is that they require a high level of stability in terms of frequency of the emission, comparable with the natural linewidth of the atomic transition which is typically in the orders of MHz. In comparison, if the source of the emission is a common diode laser, which has a typical emission that spans around a nm, or in other words a linewidth of THz, then it will be necessary to add an external cavity in order to narrow the emission spectrum (Sec. 3.1.1). Since we are working with atoms, the best way to determine the frequency of the emission is to use the absorption of other identical atoms of the same species. In doing so it needs to be addressed the additional broadening introduced by the Doppler effect, which is the main source of line broadening at room temperature (Sec. 3.1.2). After having found the correct frequency it is important to keep the emission stable by neutralizing other sources of frequency instability, like temperature, current noise or vibration. Those are dealt with by the use of a lock-in feedback system that reads the photodiode signal of a saturated absorption cell and the use of a temperature control system based on the Peltier effect (Sec. 3.1.3). After the generation of the desired laser light, another necessity is to control it. The optical path is controlled spatially by means of mirrors and lenses, but the temporal control is also crucial. In order to do this it would be impractical to physically switch on and off the diode. Instead another device called *Acousto-optic modulator* (AOM) is used (Sec. 3.1.4). AOMs can also implement small frequency changes, on the orders of MHz, which helps to lower the number of required diode lasers, since the light coming from the same

[1] The other being the atoms

laser source centered around the same transition can be divided and tuned to different hyperfine transitions. The timings of the AOMs activity, together with the SLM, magnetic coils and camera which will be exposed in Sec. 5, are what properly constitutes the data acquisition and thus are digitally controlled by a *Data Acquisition* (DAQ) connected to the main computer.

3.1.1 External cavity diode laser

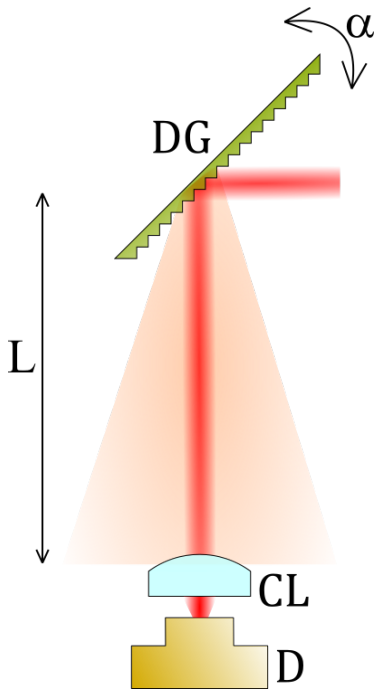

Figure 3.1: ECDL in Littrow configuration. **D** diode laser; **CL** collimating lens; **DG** diffraction grating. Only a selected part of the broad spectrum of the diode emission will be diffracted back to the gain medium of the laser, while the other is dispersed and therefore suppressed. The resulting range of frequencies is dependent on the length L of the cavity and the central frequency can be changed by varying the horizontal tilt α.

As mentioned briefly in the introduction, the diode lasers itself are unsuited for direct use on atom optics. The typical emission of the most common infrared diode laser is 100s of MHz in linewidth and also the frequency of the emission can vary greatly due to changes in current or temperature. To overcome this, one can use an external cavity to provide a frequency-selective feedback. There are a lot of cavity configuration that can be used, but I will describe only the one present in our lab which is the Littrow configuration based on the design in [103]. Let me specify here that in our lab we have developed a reasonable level of expertise that allowed us to assemble "home built" laser system, e.g. simple cavities and laser support structure. Thus we can have the two advantages of customising and eventually upgrading the design to our own needs and saving funds avoiding the need for expensive commercial laser blocks.

The first element to consider is that the diode laser is encapsulated in a diode holder with a collimation lens with the obvious goal of collimating the emission, otherwise the light would be dispersed at a large angle. Then, by putting a diffraction grating (1800 lines/mm) at 45° in respect

to the direction of the beam, some of the light will be reflected at 90° and some will be diffracted back to the laser. The diffraction is frequency dependent and that means that by fine tuning the angles of the diffraction grating, one can select which frequency to feedback inside the diode, thus narrowing the emission. Note that also by varying the length of the cavity the selected frequency to be feedback would change. Hence in the tuning of the cavity, the length is also a parameter that is changed to obtain the desired feedback frequency. However, after the first tuning the length is fixed and the finer stage of the tuning is done only by varying the angles. In principle, the larger the cavity the narrower the emission, but one must also take account of the free spectral range of the cavity $\delta\nu = c/2L$, where c is the speed of light and L is the length of the cavity, which is the range at which the cavity can be tuned before a mode-hop. To be more specific, the laser frequency can be increased (or decreased) but only for the free spectral range. After that the frequency "jumps" back to the start of the interval, as it starts lasing on another spatial mode of the cavity, thus the name mode-hop or mode jump. This limits the scannable range of frequencies. A graphical representation of the setup is shown in Fig. 3.1. Our solution to balance these two effects has been to place the diode as close to the lens as possible and the lens at a distance of about 20mm from the diffraction grating. The resulting linewidth is on the order of up to 1 MHz and the tunability range is around 7 GHz, which is enough to span the Doppler dip of Rb, the importance of which will be clear in Sec. 3.1.2. The alignment of the cavity in order to obtain the feedback is quite a delicate procedure that can be very challenging, especially to the students and researchers that approach it for the first time. Thus we have established a reliable step by step experimental procedure:

- Set the laser diode input current at the laser threshold value (~ 40 mA).
- The output value of the laser would start at 1 mW/cm^2 before alignment of the cavity.
- Search for the vertical tilt angle of the diffraction grating at which the output rises sharply up to ~ 5 mW/cm^2.
- Increase the laser diode input current up to 160 mA and check that the emission is at least 100 mW/cm^2.

- Confirm that feedback has been achieved with a suitable spectrometer (we use *Ocean Optics HR4000* with a linewidth resolution of 1 nm) and check that the emission is a single linewidth with no multiple peaks.

- Finally, span the horizontal angle tilt of the diffraction grating and check that it should be possible to vary the emission linewidth by at least 5 nm without a mode-hop.

If all these requirements are satisfied then we can be positive that the laser cavity is operating as required and we can finally set the linewidth to the value of 780 nm, by varying the same horizontal tilt angle mentioned above. There is a small disadvantage in using the Littrow configuration though: the output angle of the beam changes for the different frequencies. Nevertheless this is usually not a big issue since each laser is tuned always at the same frequency (different frequency for each laser). It is relevant though if for any reason some realignment of the cavity is necessary and another angle of the diffraction grating would result in the correct frequency being emitted. To resolve this problem it is enough to have two mirrors after the laser. Anyway, it needs to be considered that many of the different beam paths in the experiment end with a back reflecting mirror. Thus it is possible, especially if everything is nicely aligned, that the light can backtrack along the optical path returning to the cavity and the diode. This would surely affect the stability of the emission since the intensity of this "returning" beam is changed by any of the air currents or speck of dust present anywhere in the beam path. In turn this varying "feedback" would greatly affect the internal balance of the power, i.e. the emission of the cavity would not be stable. In order to block the back reflecting light we use a tool called Faraday isolator. The Faraday isolator is an device formed by three optical element pieces, two polarisers and a Faraday rotator, all placed inside a cylindrically shaped tube with two holes on the bases for optical access. The Faraday rotator is a crystal that in the presence of a magnetic field modifies the polarization of a beam passing through it, based on the principle called Faraday effect. For a specific length of the crystal, incoming vertically polarised light will rotate to diagonal. However, since the rotation direction does not depend on the direction, the back reflecting diagonal light will not rotate back to vertical, but will become horizontal. Hence with the two polariser arranged one before and one after and with their optical axis at 45° degree between each other, we stopped

the back reflecting light from returning into the cavity formed by the diffraction grating and the diode. The additional advantage of the isolator is that it can be used as an iris to guide the beam in the case of the above mentioned realignment of the cavity.

3.1.2 Doppler-Free spectroscopy

The procedure outlined above allowed us to obtain a laser beam with a stable power and narrow emission in frequency. However even if we know that the emission linewidth is in the appropriate nm range, it is not possible to confirm that is at the correct frequency for the atomic transitions. The above mentioned spectrometer [104] does not have a small enough sensitivity to resolve if we are at the frequency in tune with the transition used in our experiment. This is the optical transition from the ground state $5S_{1/2}$ to the $5P_{3/2}$ of ^{87}Rb, which is commonly known as $D2$ line and can be found in all alkali metals. It is at this point that one of the most useful characteristics of atoms comes into play: they are identical. So a frequency that would be absorbed by one atom of the ^{87}Rb isotope, will be absorbed also by another atom [2], so that the absorption profile provides a suitable frequency standard. The atoms are provided in a glass cell filled with low pressure Rb vapour at room temperature such as *Thorlabs GC25075-RB*. We pick off a small percentage of the beam from the main optical path and read the absorption of this beam passing through the cell on a photodiode.

The typical theoretical values associated with the ^{87}Rb D2 line, taken from the widely quoted Steck database [24], are $\Gamma \sim 6$ MHz for the natural linewidth and the ground state hyperfine separation is $\Delta_S \sim 6.8$ GHz while the excited state ones are between $\Delta_{P_{1/2}} \sim 70$ MHz and $\Delta_{P_{3/2}} \sim 270$ MHz[3]. Since we operate our cells at room temperature, those above mentioned frequency are all concealed behind the Doppler broadening that for every single transition frequency is $\Delta_{\text{Doppler}} \sim 80$ MHz and in an overall Doppler dip of the order of hundreds of MHz.

It is possible to circumvent this problem by using a technique called Doppler-free saturated absorption or hyperfine pumping spectroscopy [105]. This requires that two

[2] I would argue that this is one of the advantage of atom optics in respect to solid state physics experiments where small differences in the compositions or the presence of small defects in the structure or even the presence of border effects at the surface can vary the response between two samples that are supposedly the same.

[3] All frequency values are traditionally reported as angular frequency so to obtain the equivalent inverse period values it is necessary to multiply by 2π

laser beams with the same frequency, called pump and probe, propagate inside the cell in opposite direction. The role of the pump beam is to depopulate the ground state of the Rb atoms by exciting them when the laser is tuned to the transition frequency. Being at room temperature, the above condition will be satisfied for all the atoms with velocity along the beam axis

$$v_1 = \frac{(\omega - \omega_0)}{\kappa}, \tag{3.1}$$

where ω is the angular frequency of the radiation in the frame of reference of the lab, ω_0 is one of the angular transition frequencies for the atom and $\kappa = \omega/c = 2\pi/\lambda$ is the wavevector of the laser light. At the same time the probe beam will interact with the atoms in a similar way, but with the slight difference that since the probe is propagating in the opposite direction, the velocity that will match the condition of absorption for the same transition is

$$v_2 = \frac{-(\omega - \omega_0)}{\kappa}. \tag{3.2}$$

Due to the Maxwell velocity distribution, for any given frequency of the laser in the proximity of the transition there will be some atoms with same absolute velocity but travelling in the opposite direction that will absorb it. But for $\omega = \omega_0$ also $v_1 = v_2 = 0$, so the same atoms can interact with both beams[4] causing the absorption of the probe to be reduced, since the amount of atoms is finite.

In our case though there is not just one transition frequency in the scan range of the laser. For example let us take two transition frequencies ω_1, ω_2 with $\omega_1 < \omega_2$. Then there will be a velocity which satisfies

$$\begin{gathered} v_1 = \frac{(\omega - \omega_1)}{\kappa} = \frac{-(\omega - \omega_2)}{\kappa} \\ \text{which occurs at the frequency } \omega_{1,2} = \frac{\omega_2 + \omega_1}{2} \end{gathered} \tag{3.3}$$

and it is defined as crossover frequency of the transitions. At the same frequency also the atoms with velocity $v_2 = -v_1$ will satisfy the same condition by swapping the two transitions ω_1 and ω_2 in the equation, which is equivalent to inverting the role of the pump and the probe in the equation. Hence, overall an higher percentage of the population of atoms will absorb crossover lines, which tend to be more pronounced than single resonance

[4]The atoms do not need to be at rest since the velocity component that matters is the one along the axis of propagation of the light. The above formula is only valid for non relativistic velocities.

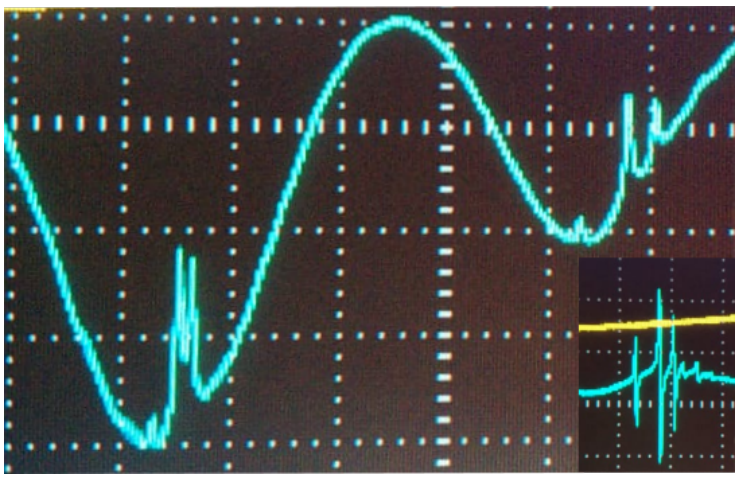

Figure 3.2: Example of the transmission signal acquired by the photodiode. The two larger Doppler dips corresponds to the transition $5S_{1/2}, F = 2 \rightarrow 5P_{3/2}$ for ^{85}Rb (on the left) and ^{87}Rb (top right). Note that the difference in depth of the transmission is due to the relative population of the two isotopes. Inside the Doppler dips are found the transmission peak and cross-overs. The inset (bottom right) shows the corresponding derivative signal of the ^{87}Rb.

lines. To explain this with a few words: at the crossover frequency the atoms going at positive velocity v_1 will absorb both the pump, which they see redshifted towards the transition frequency ω_1, and the probe, which they see blueshifted towards the transition frequency ω_2. At the same time, the atoms travelling in the opposite direction at the equal velocity will also absorb both the pump and the probe but for the opposite reasons, with the pump blueshifted and the probe redshifted. By scanning the frequency of the laser and checking the absorption of the probe there will be increased absorption for each transition frequency and each of the possible cross-overs. In our experiment the pump and the probe are the same beam back reflected. This can be easily achieved by adding a mirror at one end of the cell and a non polarizing beam splitter at the other, which redirect parts of the light towards a photodiode. I need to specify that all the above equations are usually reported in the literature [106] by assuming the probe to be weak in respect to the pump, as this simplifies notably the equation. However in the experimental realization of the setup, even with probe powers of the same order of the pump we obtain a spectra that is qualitatively the same. In the end what we measure is the final transmission after the double passage, and in this signal, shown in Fig. 3.2, we look for the "dip" which are the inverse corresponding to the absorption peaks of the atomic transitions. The scheme can be seen in the Fig. 3.3.

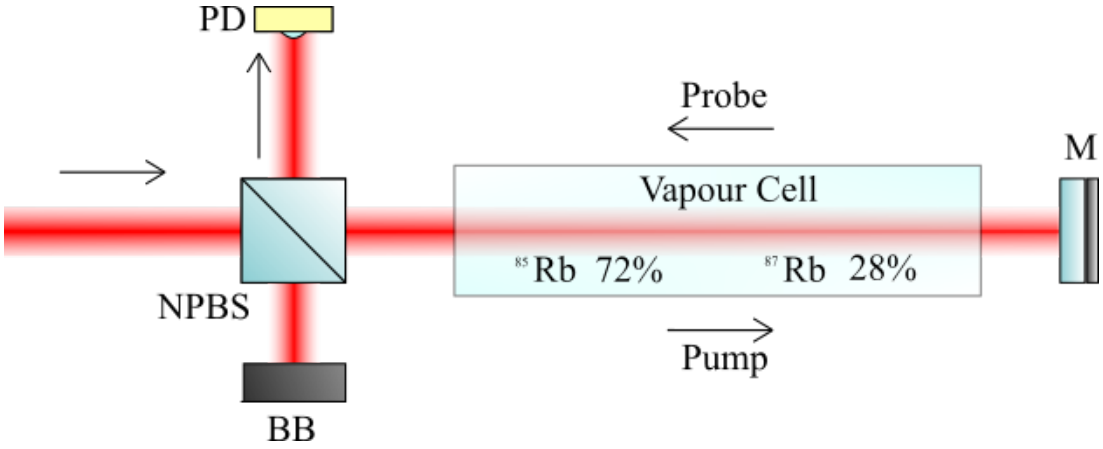

Figure 3.3: Doppler-free absorption setup. Light gets in from the left and pass through the non polarizing beam splitter. The light that gets reflected is sent to a beam block. After passing twice in the Rb cell the transmitted light is measured by the photodiode. The percentages of Rb isotopes are the natural occurring ones.

3.1.3 Laser locking

In the previous two sections I described how is it possible to narrow the emission of a laser diode and detect its frequency in respect to the desired transition frequencies. In principle this is enough but unfortunately the emission of a laser diode is too unstable to passively remain at the correct frequency. The sources of noises and drift can be related more to the cavity, like air currents and vibrations, or can affect directly the emission of the diode, like electrical current and temperature.

Regarding air current, their presence will change the effective refractive index of the cavity thus causing a shift in the optical length and changing the emission. This can be mitigated by enclosing the cavity in a box in addition to enclosing also the whole optical table. Vibrations of the support can be also a source of noise but in our case they are sufficiently mitigated by a passive vibration stabilised optical table, and hence seem to be not crucial unless there is an operator manipulating objects in the setup, which is not the case while taking data anyway.

The other two sources of noise affecting the diode are more of a problem. Although a laser diode is highly efficient at converting electrical power into light compared to other laser sources, it will still heat up while operating. The change in temperature will then result in a drift of the emission due to the change in the effective gap of the gain medium. To dissipate the excess heat and control the temperature we use a Peltier unit in combination with a temperature sensor. These two objects are placed below the holder of the diode

and thermally connected with it with thermal paste. The Peltier is then controlled by the laser diode drivers *Thorlabs ITC-102 with ITC-100D* which are the same drivers that provide the current. Theoretically by setting a temperature on the drivers the Peltier unit will actively heat or cool the diode support until the temperature sensor reads the desired set temperature. In reality the Peltier unit will continuously cool the support reaching an equilibrium with the heating generated by the diode and the resulting equilibrium temperature is some decimal of °C above the set temperature. To further stabilize the temperature, the whole lab is kept at a constant temperature with an air conditioning unit and also the above mentioned enclosing of the setup helps with the temperature stability of the experiment.

There is not much to say about current noise, apart from the fact that is it not really useful to address the diode drivers supply independently. Instead it is much more convenient to actively fight the drift caused by all sources of noises at the same time by setting up a lock-in amplifier system with active feedback by using the photodiode signal. This can be done by obtaining the derivative of the transmission signal, which has the characteristic of crossing zero at any frequency corresponding to a transition or cross-over[5] with high slopes at the side of it even if in the actual signal, the "peak", is not so very pronounced. To obtain the derivative signal we introduce the last ingredient of the diode laser support, which is a piezoelectric actuator. By setting the piezo so that it produces a small variation of the diffraction grating angle, a frequency of the order of kHz[6], this produces a small scan in frequency that probes the photodiode signal. Even by scanning the laser frequency for small quantities the extent of the signal will vary greatly depending on the gradient. By using this signal as input for a lock-in amplifier, such as *EG&G 5208 Two Phase Lock-in Analyzer*, all detector noises can be reduced by filtering the frequencies other than the piezo modulation. By carefully selecting the phase, time constant and strength, the lock-in can then provide a feedback voltage to the piezo depending on the sign of the derivative signal and thus following any drift of the "peak" to which the signal is locked.

In combination to this lock-in operation mode of the system, the laser requires a scan mode. This is also provided by the piezo movement, driven by a triangle wave of low

[5]Lock-in of the signal at a side of the peak is also possible but is not used in our experiment.

[6]This value is chosen so that the variation is faster than any sources of noises and drifts but small compared to the atomic linewidth, to avoid interference.

frequency, usually 30 Hz, generated by a signal generator. This scan mode is useful in the initial phase of setting up the experiment to check if the laser is operating at the right range of frequency by identifying the transmission signal shape[7]. So the usual procedure to set the laser frequency to the required value involves first varying the current input in the scan mode and looking for the correct transition. After this is found, the scan is turned off and the voltage of the piezo is manually set so that the signal is on the selected peak and the lock-in feedback loop is turned on.

3.1.4 Acousto-optic modulator

In our experiment there are four different transition frequencies required, and two of them are used both as a probe for the imaging system and as well as for the actual cooling and trapping of the atoms. This would require four different laser diode all with independent current drivers and lock-in system. Also for reason that are explained in Sec. 3.2.1 the trapping beams should not be exactly at resonance with the $5S_{1/2}, F = 2 \rightarrow 5P_{3/2}F = 3$, but are red detuned by ~ 15 MHz from the transition, so we can not just use the frequencies arising from locking the laser to one of the transitions. In addition to this issue, it needs to be taken into account the fact that, as we said earlier, due to the intrinsic characteristic of ^{87}Rb and the dipole matrix coefficient strength, the proper transition frequency peaks are less prominent than the cross-over frequencies peaks as observed in the transmission signal. All these consideration suggest that it might be more advantageous to lock the lasers on the more pronounced cross over peaks and then apply some additional means to modify the beams frequencies to the desired values. And thanks to the proximity of two of the transitions that we need, this would also allow us to use one fewer laser system.

As mentioned in the introduction to this chapter, the object to achieve this goal is the AOM. These devices are formed by a crystal that has high photoelasticity, i.e. the material permittivity ϵ changes when a mechanical strain is applied, that is in mechanical contact with a piezo transducer. By driving the piezo with a radio frequency, the crystal will behave as a Bragg grating for light that passes through it[8]. When the radio frequency is applied, the device will output different orders of the input light: these orders will

[7] In the typical range of frequency of our interest there are four Doppler dips corresponding to the two different $D2$ lines of the two different isotopes of Rb.

[8] In actual AOMs the efficiency of the grating is significant only for a selected range of input beam linewidth and a small range of radio frequencies in the tens of MHz.

have their frequency shifted by $\nu_{n^{th}} = \nu_{in} + n^{th}\nu_{RF}$ where ν_n is the frequency of the n^{th} order[9], ν_{in} is the input frequency and ν_{RF} is the radio frequency. In other words, the whole process can be interpreted in terms of three wave mixing between a photon of the light and a phonon of the crystal, and it is important to notice that the light does not only exchange energy with the crystal but also momentum. This change in momentum means that the output orders are going to be separated by a fixed angle that corresponds to the momentum shift given by the scattering with the phonon field.

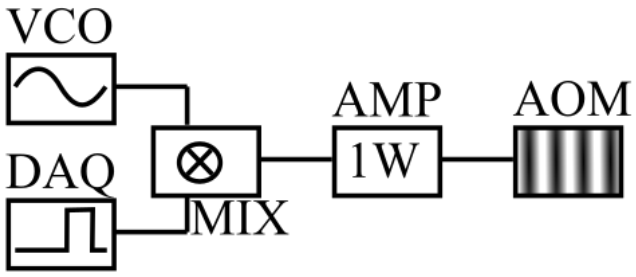

Figure 3.4: Digital control scheme of the AOM. The radio frequency is generated by a voltage controlled oscillator (VCO), and mixed with a digital signal coming from the DAQ. The effect of the mixer (MIX) is equivalent to the multiplication of the two input signal. When the signal from the DAQ is "high", i.e. 5 V, then the signal follows the sinusoidal coming from the VCO. The signal is then amplified up to 1 W with an amplifier (AMP). The resulting amplified signal generates a Bragg diffraction grating for the light inside the crystal of the AOM. When the DAQ signal is "low", i.e. close to 0 V, the output signal is as well close to 0 even after amplification.

In the experiment we use the shift in frequency to tune all the beams at the appropriate transition frequencies, which is usually some tens of MHz away from the frequency at which the laser are locked. In addition the shift in momentum allows us to use the AOMs as sort of fast "switch" that can turn on and off the laser further down the optical path. The control is done by an amplifying electronic circuit that varies the amplitude of the radio frequency and the general scheme of the system can be seen in Figure 3.4.

The AOMs are not able to completely scatter all the light in just one of the order and the one that are used in our lab achieve a typical efficiency of 75% at 80 MHz. To achieve the best degree of efficiency for the desired order, which we remind can be either positive or negative, the light is focused on the crystal and the inclination angle has to be fine-tuned to successfully achieve the phase matching condition necessary for the three wave mixing process. One thing that is worth addressing is that since the angle of the diffraction depends on the radio frequency, any change of it[10] would require realignment of the beam. This can

[9]The order can be both positive or negative.

[10]Changing the frequency can be required for experimental reason like performing different experiments with varying detuning of the probe.

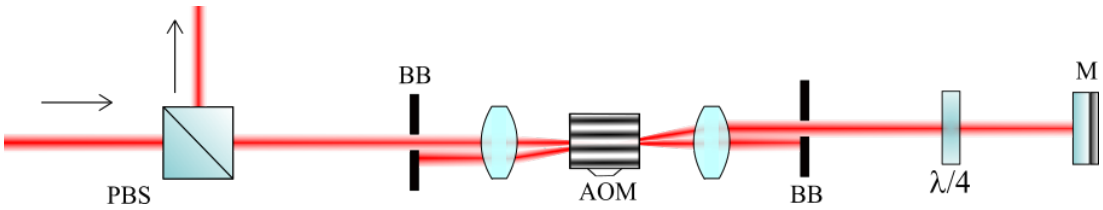

Figure 3.5: AOM Double passage configuration. In this example the radio frequency is added twice to the input frequency of the output. The beam blocks (BB) are placed so that the 0^{th} orders are blocked in both directions.

be avoided by using the AOM in a double-pass configuration [107]. This setup requires that the radio frequency is set to half the frequency of the required shift from the lock frequency to the final frequency value. First a polarizing beam splitter is placed before the AOM. As the horizontally polarized light is diffracted as previously described, the 0^{th} order path is blocked while the 1^{st} order is back reflected and its polarisation is changed to the vertical. Then the 1^{st} order is made again to pass through the AOM and the resulting 1^{st} will be reflected on the polarizing beam splitter. The geometry of the setup is such that the resulting beam will have the frequency increased by twice the radio frequency but with the resulting momentum being opposite of the input beam and independent of the radio frequency value. A visual representation of the double-pass setup is shown in Fig. 3.5.

It can be beneficial to the future students as well to the reader to outline the full procedure to align the AOM in a double-pass configuration as it requires a good amount experimental effort as much as it is crucial for the positive outcome of the experiment[11].

- Clear the optical path of the lenses, AOM, and beam block and leave only the back reflecting mirror and the polariser.
- Place an iris at the selected beam height from the table at a small distance from the polarizing beam splitter.
- Change the tilt of the back reflecting mirror so that the light will pass through the iris in both direction.
- Arrange the two lenses in a telescope configuration and adjust their position so that

[11]Specifically is the most important factor, after the cavity feedback, to achieve the maximum possible power for the trapping beams, which in turn is the main factor to determine the amount of atoms that will be trapped with the *Magneto Optical Trap* (MOT) described in Sec. 3.2.1.

the beam passes at the center of the lenses. This will automatically be if the beam position did not change at the iris location.

- Place the AOM at the focus of the telescope realized by the two lenses.
- Turn on the radio frequency and measure with a power meter the intensity of the desired order. This should be optimized by changing the angle between the AOM and the beam, as well as the AOM position itself.
- After having optimized the first passage, block the 0^{th} order and insert the $\lambda/4$ wave plate QWP between the beam block and the back reflecting mirror, so that only light generated by the selected order will have the correct polarisation to reflect at the polarizing beam splitter.
- Measure the power at the output of the polarizing beam splitter and optimize the intensity by changing the optical axis of the QWP as well as fine tuning again the inclination and tilt of the AOM.

If this procedure is successfully implemented, up to 56%[12] of the original input power will be converted into the new frequency and it is ready to be used in the proper experiment as a probe or as trapping beam.

3.2 Atom trapping

The cooling and trapping of atoms has always been of interest for researchers, especially in the fields of spectroscopy and statistical physics: disposing of a sample of identical atoms at low temperature allows to address electron transition on the fine structure, which has been made experimentally easier especially after the development of the laser, and to study collective behaviour of degenerate states of matter like *Fermi gas* or *Bose Einstein Condensate* (BEC). Thanks to the development of many trapping techniques [108–113], it was possible to obtain the experimental realization of those concepts. Although it was postulated the existance of these exotic states of matter as early as the 30's, they were only realized in a lab only in the 90's with the experiments at JILA [114] and MIT [115]

[12]Naturally the efficiency of the double passage is the square of the single passage.

for the BEC, and the experiment at LENS in Florence [116] for the Fermi gas.[13] These experiments, as well as others in the same period that are not cited here, have pioneered the path of modern atom optics.

For the purpose of the experiments in my group, we are not required to reach the density and the temperature typical of a BEC. Since our interest and expertise lies mainly on spatially structured light we require extended atomic clouds with small enough *Optical Density* (OD) to observe the variation in light propagation. For this is sufficient, and in some cases even better, to only apply the cooling technique called the *Magneto Optical Trap* (MOT) which will be described in the section Sec. 3.2.1 following the procedure described in [118]. After this cooling stage we switch to a different trapping configuration called *Spontaneous force Optical Trap* (SpOT) Sec. 3.2.4 which has the main purpose of increasing the population of the atomic hyperfine level which will then be used in the main experiment. In the previous Sec. 3.1 I focused on the discussion about the light involved in the experiment and that is also a fundamental part of the trapping process. However the trapping of neutral atoms would be almost impossible without the manipulation of the magnetic field, and therefore I will discuss accordingly this aspect of the experiment in Sec. 3.2.2, focusing on the techniques and instrumentation that allow its generation and control.

In Sec. 3.2.4, I will also illustrate how we use the SLM in the main setup. I should note that the way the SLM is used in the main setup is limited in comparison to its potential. The SLM properties have been discussed in more detail in Sec. 2.6 and for more indication on its operation in our lab I remind on the Dr. Selyem Ph.D. thesis [89].

3.2.1 Magneto Optical Trap

I will illustrate in this section the concepts behind the working of MOTs. The discussion will be done in a one dimensional system but the application on the 3D case comes automatically by applying the same technique in 3 orthogonal directions and adding their effect linearly. This is not strictly required and there are many experiments with different MOT geometries. 1D MOTs are shaped like flat disks or "pancakes", 2D MOTs [119]

[13] I am aware that superfluid ^4He was achieved much before [117] the first experiment on the BEC at JILA and that can be considered as the first example of BEC in experiments, but anyway the applications of such system is rather small compared to the modern experiments with BEC. Similar consideration can be done for the early manifestation of fermionic gas.

are shaped as elongated tubes or "cigars" while 3D MOTs are more ellipsoid or droplet shaped due to the effect of gravity and the magnetic field gradients. The latter geometry is the one used in our experiment.

In mechanical terms, to "cool" a gas cloud means to reduce the mean kinetic energy of the individual atoms or in other words, slowing them down. One of the first notions encountered by physicists in their undergraduate studies is that to change the velocity of an object a force must be applied to it. In our case, since we only want to slow the atoms, the force that is best applied would behave like a friction, i.e. the direction of the force should always be opposed to the direction of movement. In the case of MOTs, the dissipative force that arises from the radiative pressure that has exactly this characteristic [120, 121]. There is another kind of force, usually referred to as reactive force, associated with the radiative pressure. Anyway, this component of the force cancels out when the field amplitude does not depend on the position relative to the light beam. In our experiment this approximation holds. We affirm this to be the case because, although the trapping beams have Gaussian profiles and the intensity has a spatial dependence as any experimental light beam should have, the waist of the trapping beams is much larger than the trapping area. Thus, in the theoretical overview of the technique, I am going to ignore the spatial dependence of the trapping beams, i.e. the beams will be approximated as plain fields when interacting with the atoms[14].

Let's consider a two level atom, $E_0 = h\nu_0$ being the energy difference between the two levels, with velocity $\mathbf{v}_i$ along $\hat{x}$ corresponding to a kinetic energy $E_i = v_i^2/2m$ and two counter propagating beams with frequency ν_l and momentum $\mathbf{k}_\pm$. The beams are red detuned in respect to the transition, i.e. $\Delta = \nu_l - \nu_0 < 0$. Due to the Doppler effect, in the inertial frame of reference concordant with the motion of the atom the frequency of the beams will be modified as:

$$\nu_{\text{dopp}} \sim \left(1 - \frac{\mathbf{k}_\pm \cdot \mathbf{v}_i}{|\mathbf{k}_\pm| c}\right) \nu_l \quad \text{for } |\mathbf{v}_i|/c \ll 1 \tag{3.4}$$

so that the beam going towards the atoms ($\mathbf{k}_+$) will be blue shifted by $+\frac{|\mathbf{v}_i|}{c}$ while the counter propagating one ($\mathbf{k}_-$) will be red shifted by $-\frac{|\mathbf{v}_i|}{c}$. The effect of this correction in the frequency is that the absorption probability of the two beam will depend on the

[14]This consideration applies mainly in regards to the radial profile of the individual beams. The longitudinal dependence of the beam intensity will be discussed later in the section.

speed and direction of movement of the atom, with the probability of absorbing the beam going towards it being higher. Hence, when an atom absorbs a photon belonging to this beam, possessing momentum $\mathbf{k}_{\text{photon}} = h\kappa = hc/\nu_l$ and energy $E_{\text{photon}} = h\nu_l$, the resulting momentum of the atom will change to $\mathbf{p}_{\text{atom}} = m\mathbf{v}_i - hc/\nu_l$, thus slowing the atom.

This energy and momentum can be re-emitted in two ways. If the re-emission is via stimulated emission mediated by the same beam from where the photon was absorbed from, the atom will lose energy E_{photon} and regain momentum p_{photon} resulting in no net change of both energy and momentum. The other possibility is that the photon is released via spontaneous emission and in this instance the probability of the emission is isotropic, i.e. the photon can be emitted in every direction with equal probability. In this case, after a number of cycles of absorption and emission the contribution of the spontaneous emission to the momentum will average to 0. So as time evolves, the result of the cycle of absorption and re-emission is a net loss of momentum in the initial direction of movement of the atom. In addition to the above considerations, it is important that the time evolution of the external variables of the atom is slower than the absorption-emission process, otherwise the process will not be efficient enough to cool the atoms in large enough quantities. In other words the atoms would traverse the trapping area with the beams without slowing enough to be captured. The validity of this assumption varies by the choice of the species to be cooled and for ^{87}Rb is fairly solid as the typical time evolution of the external degree of freedom is 3 orders of magnitude slower than the time evolution of the atomic transition which is used to cool it. In addition, the presence of the beam coming from the other direction ensures that this process works symmetrically for an atom with positive or negative velocity.[15]

This process would work in principle at any detuning but it is important to consider the distribution of velocities of the atoms as we did in Sec. 3.1.2 and the fact that for each velocity only a small range of detuning will be effective to cool the atoms. Since the linewidth of our trapping beam is narrow in respect to the speed distribution, the vast majority of the atoms are actually unaffected by the cooling process. In fact, in our experiment the trapping beams are red detuned at $\delta = 16$ MHz which translates to a capture velocity around 3 m/s, that is possessed only by a small fraction of the slower

[15]The Zeeman slower is an example of a cooling system that works only for one component of the velocity which uses also the Doppler cooling principle explained above [122].

atoms. This is the most rational choice of detuning because the radiative force is linear around 0 m/s with negative gradient, so that any atom within the capture velocity range will be effectively slowed[16]. In more detail regarding the choice for the value $\delta = 16$ MHz. The value of the optimal detuning[17] that can be theoretically calculated of $\Gamma/2$ is very close to the experimental optimal value that we found. Our value is however found empirically as it is the value that produces the largest atomic cloud and that its stability is not affected by the noise present in the trapping beams. For smaller detuning in fact the cloud is much less stable, as it appear to "move around". This is due to the fact that the atoms do not lose enough energy during the radiative processes and end up moving in and out of the trap at a high rate, hence giving the impression of a turbulent atomic cloud when watching the fluorescence on the camera.

So far we have seen how the radiative force can be used to slow, and thus cool, a consistent portion of ^{87}Rb atoms. The reader will probably note though that laser cooling is not spatially dependent. Save for the effect given by inhomogeneous intensity of the beam, which we said is negligible in our case, the cooled atoms will just slowly scatter in the vacuum cell and their density will be too low to use in most experiments. To increase the density of atoms and trap them as much as cool them, the slowing effect must also have some kind of spatial dependence. In the MOT, the ingredient used for this is a magnetic field generated by a pair of Anti-Helmholtz coils. Let us consider a system as in Fig. 3.6 in which we have a linear magnetic field in the proximity of $x = 0$ and 0 value in the middle. This is an approximation that holds up close to the 0 of the quadrupole magnetic field generated by the above mentioned Anti-Helmholtz coils. This magnetic field acts as a spatial modulation of the Zeeman splitting of the atomic levels and this generates the desired effect of a spatial dependence to the Doppler cooling. The variation of the Zeeman splitting caused by the variation of the magnetic field, changes the resonance condition of the beams and thus the range of velocities that are effectively cooled in each position. The spatial dependence is such that only at the place of zero magnetic field the radiative forces from the two counter propagating beams are balanced, while one prevails over the other anywhere else. This is achieved by using beams with circular polarisation so that

[16]There is a limit to how much atoms can be cooled in a MOT which is due to the combination of the effects of Doppler cooling and recoil heating. Nevertheless it is not really necessary in our work to achieve lower temperatures than the ones reached with MOT.

[17]Optimal as it gives the limit coldest temperature.

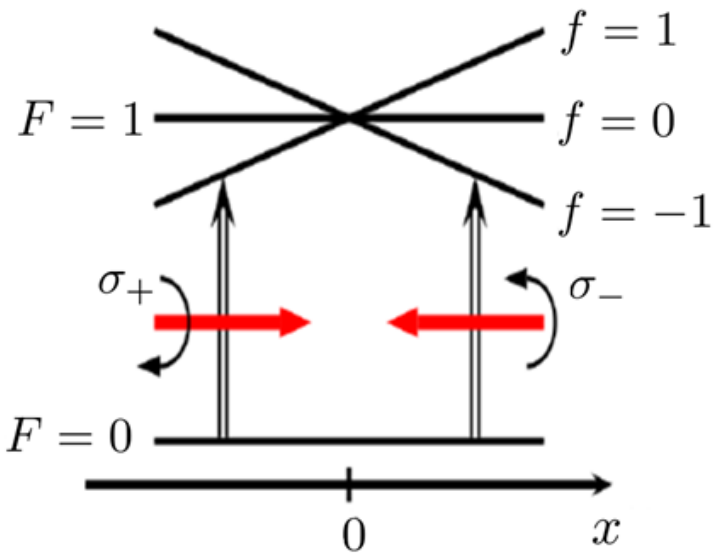

Figure 3.6: Magnetic gradient induced Zeeman splitting. The Zeeman splitting of the upper level structure in the presence of a magnetic field gradient gives rise to an enhancement of the absorption probability for the beam that is coming towards the atom. The resulting effective trap force drives the atoms towards the 0 of the field.

the atom is optically pumped towards one of the extremes of the Zeeman substates. In Fig. 3.6 the process is simplified due to the level structure, but the principle holds as well for ^{87}Rb where the resulting pumping favours the absorption towards $F = 3, m_F = \pm 3$ sublevels. To extend this technique to 3D we just need 6 counter propagating beam in 3 orthogonal direction with the proper polarisation.

For the atomic species ^{87}Rb the most used trapping transition possesses the level scheme illustrated in Fig. 3.7. The atoms undergo the cooling cycle driven by the trap laser between $F = 2, 5S_{1/2} \rightarrow F' = 3, 5P_{3/2}$. However, roughly once every 100 transition, the atom can instead be excited from $F = 2, 5S_{1/2}$ to $F' = 2, 5P_{3/2}$ and then decay to $F = 1, 5S_{1/2}$ thus exiting from the cooling cycle outlined before. To avoid that, we use an additional laser field, called repump, resonantly driving the transition $F = 1, 5S_{1/2} \rightarrow F' = 1, 5P_{3/2}$, from which then the atoms can decay back on either of the ground states but will eventually re enter the cooling cycle. With this technique we reach temperatures of hundreds of μK and densities up to 10^{10} atoms/cm^{-3}.

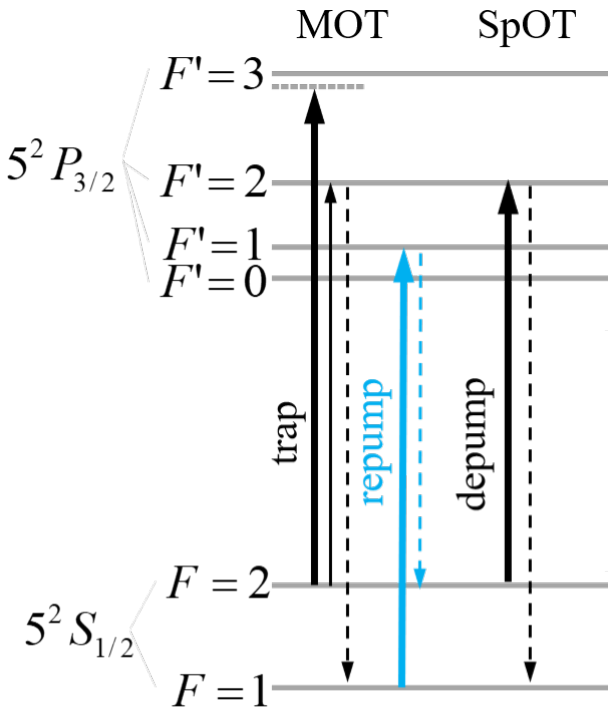

Figure 3.7: Level scheme of ^{87}Rb for atomic trapping with the optical transition employed in the MOT and SpOT techniques. The mechanism behind the SpOT, as well as the role of the depump beam which has not been mentioned until now, will be explained later in Sec. 3.2.4.

3.2.2 Magnetic Field Generation

I hope it has been established in the mind of the reader, how crucial is the magnetic field in the efficient trapping of the atoms. In addition, our experiment revolves around the interaction of the magnetic field with the atoms, and its measurement through the absorption of a structured beam. Thus it should not surprise that the generation and control of the magnetic field takes substantial attention and effort in the overall workload of the daily activity, especially when taking data.

The handling of the magnetic field is controlled by 4 sets of coils, which can be distinguished in two different systems. In our system, one is made with a pair of circular coils operating in the anti-Helmholtz configuration, and is fundamental in the preliminary trapping and cooling stages of the experiment. To be more specific the Helmholtz and anti-Helmholtz configuration for magnetic coils refers to the current circulation direction in the coupled coils, concordant in the former opposite in the latter. In the idealized case, using Ampere's law for circuit loop is then easy to verify that the Helmholtz configuration will produce a linear magnetic field, while the magnetic field generated by the

anti-Helmholtz configuration is a quadrupole field with zero at the central point between the coils. The other is formed by three pair of rectangular coils, mainly due to considerations of optical axis and ease of mechanical construction, and the relative electrical equipment, and is responsible for the cancellation of any spurious field from the environment and for the generation of the linear magnetic field, which is one of the primary ingredient in the absorption experiment.

The magnetic field is generated by the coils based on the current driven in their circuit. Generally, it is the voltage that can be changed and is set to a particular level, and as a consequence sets a value for the current[18]. However due to the high currents that are necessary and the fact that the magnetic field is not kept constant throughout the experiment, the coils undergo a change in temperature that is enough to bring unwanted instability and require additional care. In our case this has been solved by adding an additional current driver system, which were developed in the earlier stages of the setup and are discussed more in detail in [89]. In this circuit the current in the coil is monitored with a 1 Ω resistor. When the coils generate the magnetic field, driven by a signal from the control program of the experiment, the voltage related to the coil current is compared to a reference voltage set as a parameter. The difference between the monitored voltage in the coils and the reference wanted voltage is passed through a low-pass filter to avoid sharp oscillation[19] and then used to control the resistance of a FET placed in series with the coil. This creates a feedback for the current through the coil.

Due to the constraints given by the geometry of the trapping beam, it is not possible to place the rectangular coils such that each coil independently acts only on one of the axes of the system. For this reason the two coils acting on the plane $x - z$ are rotated by 25° on this plane. By keeping in mind the coordinate system and frame of reference used in the experiment, the resulting linear magnetic field can be expressed as:

$$\mathbf{B} = \begin{pmatrix} B_x \\ B_y \\ B_z \end{pmatrix} = \begin{pmatrix} B_1 \cos 25^\circ - B_2 \sin 25^\circ \\ B_3 \\ B_1 \sin 25^\circ + B_2 \cos 25^\circ \end{pmatrix}. \tag{3.5}$$

Since in the experiment we actually control the current in those coils, it is useful to invert

[18] Based on the relation given by Ohm's law $V = IR$

[19] To be specific this is defined as ringing

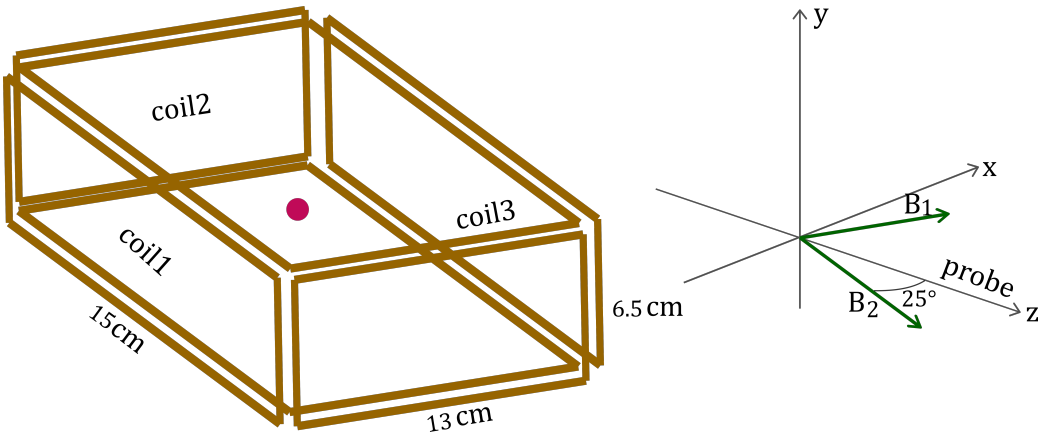

Figure 3.8: Schematic representation of the rectangular coils and their orientation respect to the atomic cloud (red dot). The origin point of the coordinate system on the right is also the atomic cloud, but here is shifted for better readability. Note that the name of the coils refer to opposite facing pairs.

Eq.3.5 to obtain the field for coils 1 and 2 [20]

$$B_1 = B_z \sin 25° + B_x \cos 25° \tag{3.6}$$

$$B_2 = B_z \cos 25° - B_x \sin 25°. \tag{3.7}$$

Now we need to determine the current to generate those fields. For such rectangular coils, placed in a Helmholtz configuration, with N turns, dimension a, b and separation h the current I required to generate a particular $\mathbf{B}$ along their axes is given by [123]:

$$I = \frac{5}{8}\frac{B}{N}\frac{(a^2+h^2)(b^2+h^2)\sqrt{h^2+a^2+b^2}}{ab(h^2+a^2+b^2)} \tag{3.8}$$

In our experiment these parameter are $N = 30$, $a = 13$ cm, $b = 15$ cm, $h = 6.5$ cm and the usual values for I are of the order of 1 A. An equivalent visual scheme of the background coils orientation is shown in Fig. 3.8. By using this expression and the one above we can choose the desired $\mathbf{B}$, which is composed by the sum of the $\mathbf{B}_{\text{exp}}$ and the field necessary to compensate for the $\mathbf{B}_{\text{back}}$, and the PC control will automatically generate the necessary currents for the three pairs of rectangular coils.

The magnetic field is generated by the circular coils with an analog mechanism but due to the anti-Helmholtz configuration, the expression and the shape of the magnetic field

[20] Since they are intermingled. Generating the field in the y direction is easier since it involves only one coil.

changes substantially. Here I will just present the Taylor-expanded expression truncated to the 3$^{\text{rd}}$ order at the origin:

$$\mathbf{B}_{\text{quad}}(r,y) = (B_r(r,y), B_y(r,y)) = B_{1st} I \left(\frac{-1}{2}, y\right) + B_{3rd} I \left(\frac{3r^3}{8} - \frac{3r^2 y}{2}, y^3 - \frac{3r^2 y}{2}\right), \tag{3.9}$$

with

$$B_{1st} = \frac{24\pi N d^2 s}{5(d^2+s^2)^{5/2}}, B_{3rd} = \frac{96\pi N d^2 s(4s^2-3d^2)}{(d^2+s^2)^{9/2}}, \tag{3.10}$$

where I is the current flowing through the coils, N is the number of turns of the wire, d cm is their diameter, s cm is how much they are separated. The term r in the above equation is the distance from the origin in the plane x-z. The placement and cylindrical symmetry of the circular coils translates in the quadrupole field showing cylindrical symmetry. Another important property to note is that at the point $(0,0)$ the field is in a minimum $\mathbf{B}_{\text{quad}}(0,0) = (-B_{1st}I/2, 0)$. The second is that in the area of interest of the atomic trap, the magnetic field can be assumed to be linear, as expected if we want to optimize the MOT. By inputting the experimental parameters $I = 2.5$ A, $N = 80$, $d = 8$ cm and $s = 7$ cm it turns out a gradient close to 4 Gcm^{-1} for the y direction and 2 Gcm^{-1} for the other two dimensions.

Empirically the higher or lower value of the gradient can be seen to affect the atomic cloud causing two opposed effect. We notice that for higher gradient the cloud is more dense and "pinned in place", while at the same time the atomic cloud has a smaller size and a smaller area of trapping potential for the atoms, thus reducing the overall atom number. On the opposite, for a smaller coils current, e.g. 1.5 A, the atomic cloud is more disperse, occupying a larger area with overall more atoms. With currents below 1.5 A, the trapping potential becomes too shallow for our purposes, and only some fluorescence from the trapped atoms is observed at the position where the MOT cloud should form, but with a unstable nature similar to what happens when the frequency of the trap laser is not detuned enough from the $5S_{1/2}, F = 2 \rightarrow 5P_{3/2}, F = 3$ transition. Fig. 3.9 shows the different atomic clouds that forms with the different quadrupole coils current mentioned above.

It must be noted that due to the timed nature of the experiment we must verify that the transient times for the coils, both rectangular and circular, is taken into account. In particular it is important that the quadrupole magnetic field is turned off between the

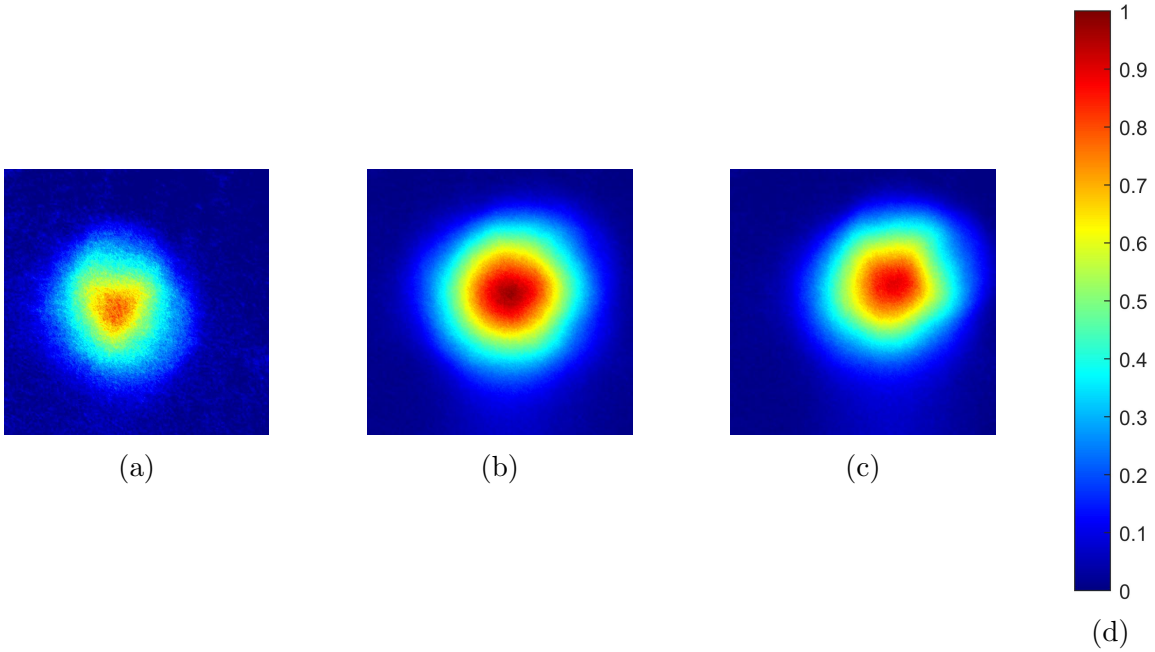

(a) (b) (c) (d)

Figure 3.9: Fluorescence images of cold atomic clouds formed under different quadrupole coils currents. (a) 0.5 A. (b) 1.5 A. (c) 2.5 A. (d) Fluorescence intensity, arbitrary scale.

trapping phase and the taking of the absorption image. We estimate that this transient time accounts for ~ 2 ms and ~ 1 ms for the quadrupole field and the compensation field respectively. In our setup this is taken care of as we allow the atomic cloud to expand for at least 3.5 ms between the two phase of the experiment, thus ensuring that the magnetic fields are the desired ones.

3.2.3 Background Magnetic Field

Before concluding the discussion regarding the generation of the magnetic field, it needs to be noted that the only parameter that we can directly affect while operating the coils is their current: the value that we input is obtained through the various calculation using Eq. 3.5, 3.7 and 3.8 so that we obtain the desired magnetic field in the system. However any independent direct measure of the resulting magnetic field is quite challenging in our experiment. For example the fact that there is a glass cell to keep the atoms under vacuums implies that we cannot use an Hall probe at the position that we are interested to measure the magnetic field. Other experimental ways to measure the magnetic field, like measuring the Larmor shift or the Larmor frequency of the atoms with a resonant beam, can not be used as the trap and probes present in the setup are not optimized for this kind of measurement. In the end the most reliable way that we have to measure the

values of the magnetic field that we use in the experiment, is the magnetometry through the absorption experiment itself. In this section I will discuss this substantial issue and how we can calibrate the magnetic field to compensate the background magnetic field with the tools at our disposal in the absorption experiment, especially since this has been an important part of the development of our research and occupied a large portion of my involvement during the realization of the experiment.

First of all in every MOT configuration it is important, although not strictly necessary, to cancel the background magnetic field B_{back}. This field includes the Earth magnetic field, which in the Kelvin building in Glasgow is ~ 0.5 G, as well as other sources inside and outside the lab. In this regard, we believe that the main component is due to the vacuum pump, mainly because it operates at high voltage and its proximity to the experimental glass cell. Overall the total compensation that is applied is

$$\mathbf{B}_{\text{comp}} = \begin{pmatrix} 0.68 \\ 2.42 \\ 1.15 \end{pmatrix} \text{G}, \tag{3.11}$$

which adds up to a total $B_{\text{comp}} = 2.77$ G[21]. A standard technique to optimize $\mathbf{B}_{\text{comp}}$ is as follows:

- Get a large enough atom cloud in the MOT
- Block for a short time one of the paths of the trapping beam[22]
- Observe how the MOT dissipates and then reforms, taking note if it seems to "move"
- Change one component of $\mathbf{B}_{\text{comp}}$ to cancel the unbalance outlined by the "motion" of the cloud
- Repeat until the cloud grows and dissipates in an isotropic fashion.

This technique is quite useful to optimize the density and atom number of the atomic cloud in a MOT, but it is not ideal to completely compensate the background magnetic

[21]Note this is the compensation field. The background field $\mathbf{B}_{\text{back}}$ is equal and opposite.

[22]Ideally you would want to block all the paths at the same time, so that there are no remaining beams to exercise a directional scattering force. This would be very frustrating to do properly so for the sake of simplicity, I usually performed the outlined procedure blocking one path, and then checked that blocking the orthogonal path the atomic cloud would still grow and dissipate isotropically.

field, which is crucial for our experiment. In fact, there is an intrinsic reason that the above technique will suggest a $\mathbf{B}_{\text{comp}}$ that is not really compensating $\mathbf{B}_{\text{back}}$ and the reason behind this is the geometry of the trapping configuration. The necessary 6 orthogonal beams are in reality 3 orthogonal beams that are reflected again inside the glass cell with mirrors. Each one of the back reflected beam will have less intensity than the counter propagating beam since it passed already inside the atomic cloud, being slightly absorbed by them. An additional term of loss is at the glass surface of the cell, which the back reflecting beam needs to pass 4 times more than the counterpart to reach the atoms, as well as losses due to the double passage through the quarter waveplate and the reflection from the mirror. In the end what this means is that the technique that balance the "motion" of the atoms not only compensates for $\mathbf{B}_{\text{back}}$ but also for this unbalance in the trapping beam[23]. At first we tried to take account of this issue by placing a focusing lens on the path of the trapping beam. The reasoning behind this is that in the space where the cloud forms the back reflected beam will have a higher intensity, due to being smaller, and thus should match the power of the opposite beam and our calculation showed that using the above mentioned focusing lens would compensate so that the two counterpropagating beam would have equal power at the center of the trap. By calibrating the $\mathbf{B}_{\text{back}}$ with the procedure outlined above with the addition of the lens had the good result of producing a bigger cloud with more atoms arranged in a more symmetric fashion. More specifically, it was calculated that with a converging lens ($f = 2500$ mm) would be able to compensate all the losses, and consequently the two counterpropagating beams would have the same intensity at the center of the trap. However in the experiment it was still evident that there was a residual $\mathbf{B}_{\text{back}}$ that induced noise in the generation of the desired $\mathbf{B}_{\text{exp}}$, since the interaction between the vector vortex beam and atoms in our experiment is much more sensitive to the magnetic field than the MOT optimization process. Hence it was not possible to properly compensate $\mathbf{B}_{\text{back}}$ to the level that we needed to achieve.

In the end, we resolved to just focus on the effect that $\mathbf{B}_{\text{comp}}$ shown in the absorption image. At the same time this meant that we would not have the ideal magnetic field to optimize the MOT, but we decided that it was acceptable due to the small decrease in size of the atomic cloud. To show how the compensation through the absorption image is achieved, let us first assume a perfect $\mathbf{B}_{\text{comp}}$. In these condition we should get the same

[23]Which unfortunately results in a radiative pressure in the same overall direction of $\mathbf{B}_{\text{back}}$

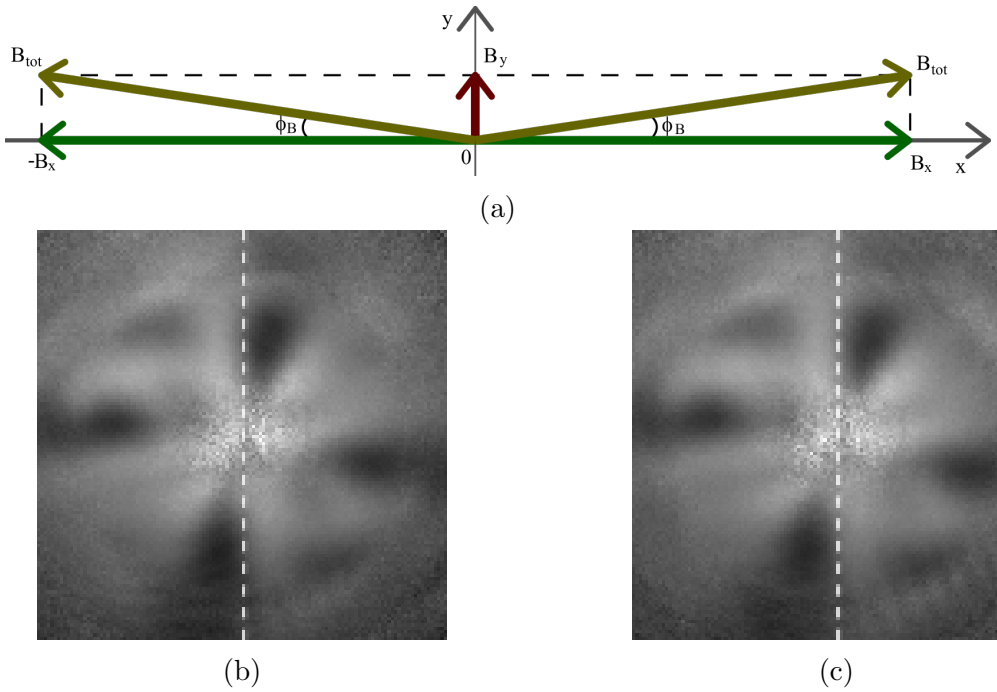

Figure 3.10: Compensation of spurius magnetic fields. (a) In this example there is a residual $B_{\text{back}} = B_y$. To detect it, we apply $B_{\text{exp}} = \pm B_x$ in two absorption experiment. The total field B_{tot} will point at different angles, thus the two absorption images (b-c) will be rotated one with respect to the other. The dashed line is present to help notice the difference. The full experimental procedure to acquire the absorption image is shown in detail in Sec. 5.1.4

absorption image by applying a transverse $B_\perp$ or $-B_\perp$ of small magnitude[24] in either the $\hat{x}$ or $\hat{y}$ axis. For example, consider the case in which the field applied is $B_x = \pm 0.02$ G. If the two absorption images are different, .i.e. are "rotated" one with respect to the other, it means that there is a B_{back} component along the $\hat{y}$ axis so that the total **B** field will not be along the same line in the two experiment.

3.2.4 Spontaneous Force Optical Trap (SpOT)

The first stage of cooling allowed us to collect the atoms in a dense cloud from the background vacuum concentration inside the glass cell. After having cooled and trapped the atoms with the MOT, base on the particular needs of our experiment we need to accumulate most of the atoms in the state $5S_{1/2}, F = 1$, as we prefer to use this state. The reason for this choice will be exposed in Chap. 3 and in more detail in Sec. 5.4 where we draw the parallel between two similar experiment with one of the difference being the choice of

[24] of the order of 0.01 G, which is 2 orders of magnitude smaller than the outlying B_{comp}

the ground level involved in the probe absorption. For now it is sufficient to mention that the $F = 1$ has fewer sublevels than the $F = 2$, reducing complexity for simulation and modelling.

Before going into the detail let us present the general idea behind the SpOT [124]. While the atoms are trapped in the MOT configuration, they constantly undergo cycles of absorption and re-emission, which is necessary to maintain them cooled and trapped continuously. Instead in a SpOT the atoms are spontaneously left to populate a dark state, in respect to the trapping beams. This has the advantage that the atoms in this state, by not interacting with the trapping light, are capable to reach much higher atomic densities. In fact the scattered radiation in a normal MOT, results in an effective repulsive force between atoms. In addition in a SpOT, since the atoms do not get to the excited state, they do not collide with other atoms, which is a channel of loss for the atoms in the trap. Anyway it should be clear that an atomic cloud can be stably trapped in a MOT indefinitely, provided the laser frequency is locked and the vacuum pump is working, a SpOT will gradually lose all the trapped atoms and would need to be reformed again with the procedure that will be explained in detail in the next pages.

We start by reminding the function of the repump beam, mentioned briefly in Sec. 3.2.1, which is used to keep the atoms in the cooling cycle of the MOT. This mechanism is the central keystone of the SpOT procedure. The trap laser frequency is red detuned in respect to the $5S_{1/2}, F = 2 \rightarrow 5P_{3/2}, F' = 3$ transition by $\delta = 16$ MHz. Due to this detuning there is a chance that the atom would be excited to the $5P_{3/2}, F = 2$. This probability is small, in average 1 in every 500 absorption cycles this could happen, but not so small that it does not affect the MOT. In fact when the atom re-decays to the ground state it could fall in the $5S_{1/2}, F = 1$, becoming invisible to the trap light. In practical terms this would translate in a substantial loss rate for the MOT atom numbers, so since the first experiments demonstrating the technique of the MOT, a *repump* beam was added to "bring back" this lost atoms inside the cycle: the repump frequency is set to a transition from the $5S_{1/2}, F = 1 \rightarrow 5P_{3/2}, F' = 1$ [25] so that it eventually re-decays in the $5P_{3/2}, F = 2$ and continue to be trapped by the MOT. The standard MOT for ^{87}Rb has the advantage that only one of this repumps are needed but there are other MOT schemes for other elements or molecules that require more.

[25] This would work also if the target state was $5P_{3/2}, F' = 2$.

Now that we established how important is the repump for a MOT to work and form a stable cold atom cloud, the reader would have guessed that to fulfill the objective of transferring the atoms in $5S_{1/2}, F = 1$ we just need to "turn off" the repump somehow. The first naïve option of just not having the repump in the first place is not particularly good as one can imagine because of what we just said earlier of the repump importance for a good MOT to work. We can think of removing partially the repump in two ways: temporally and spatially [125]. By removing the repump temporally we mean that after a phase of ~ 10 s in which the standard MOT scheme is in place, we can turn off the repump beam and just let the atoms accumulate in the dark state $5S_{1/2}, F = 1$ [26] for ~ 100 ms and then perform the experiment with those atoms. This could be achieved easily enough by using the AOM techniques described in 3.1.4 thus would not require anything more in terms of the experimental setup. The numbers of atoms available for the experiment is increased in respect of the "no repump" case but not by much. In fact, since the atoms in the dark state are not being affected by the trap laser means that are not trapped anymore. Any residual thermal velocity that they possess would translate in the cloud expanding. This can be seen as a loss rate that would counter the rate of transition to the dark state thus limiting the number of atoms in that state. The other option of removing the repump spatially is by removing light in the central part of the repump beam or "making a hole". The idea behind this is that the atoms in the dark state "floating away" will eventually encounter the remaining part of the repump beam, absorb it, and re-enter the trapping cycle. So instead of having a constant loss of the hotter atoms in the cloud, they will be "recovered". This process is exemplified in Fig. 3.11.

The desired repump light pattern can be realized by blocking an area on the optical path[27]. The disadvantage of modifying the repump in this manner can be found in the MOT. It should not surprise that the efficiency of the MOT drop significantly, i.e. reduced number of atoms trapped and at a slower rate, if the repump is not present in the same region of the MOT where the trap light is most intense. The typical size of the subtracted light circle is ~ 1 cm in diameter[28].

To overcome this disadvantages, in our experiment we combined [126] the desired effect

[26] For the trap beam.

[27] For example adding black paint on the centre of a mirror.

[28] The "hole" size dimension is chosen in an empirically process of optimization, i.e. higher density and number of atoms in the dark state. Note that the sizes for the optimal values are significantly larger than the cloud of atoms in the MOT or SpOT phase.

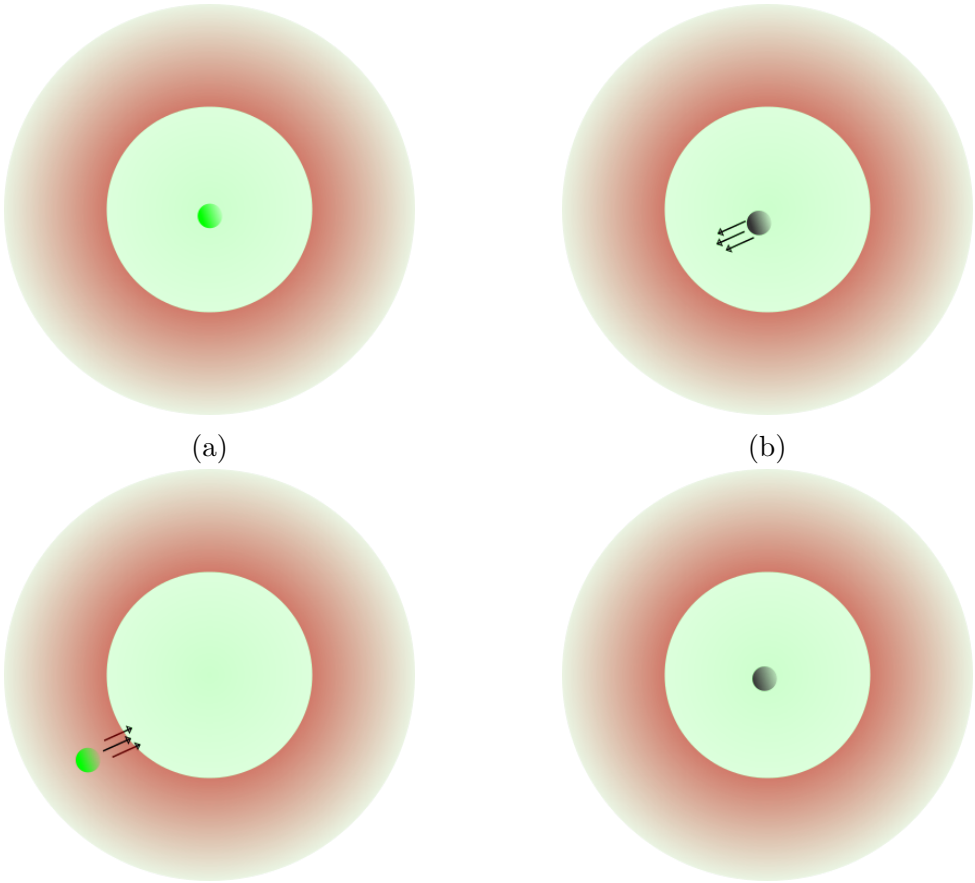

Figure 3.11: Repump "hole" technique for SpOT. (a) The atom in the $5S_{1/2}, F = 2$ state (green) is cooled by the MOT with the trap light (green). (b) The atom eventually decays in the $5S_{1/2}, F = 1$ state (grey). Since there is no repump light (red) at its location, it is effectively in a dark state and not trapped and it will drift if it possess any residual thermal motion. (c) After some time it will re-enter in an area with repump light, transition to the $5S_{1/2}, F = 2$ and trapped again towards the center of the MOT. (d) Eventually, after some cycle it will decay to the dark state with almost zero thermal motion. To enhance this process, in the "hole" area there is another beam "depump" to increase the rate of decay to $5S_{1/2}, F = 1$.

of the temporal and spatial approach by modifying the repump light beam with a Spatial Light Modulator. As an active optical device, the SLM can be used to modify the beam shape and phase at a set time interval.

The experimental procedure is as follows: first the cloud is formed with a standard MOT for $\sim$ 10 s, reaching densities up to 10^{10} atoms/cm^{-3}. Then the optical phase structure of the SLM is modified so that the repump gets a circular "hole" with zero intensity in the middle. The holograms involved in this can be seen in Fig. 3.12 The atoms in the MOT cloud starts to decay in the $5S_{1/2}, F = 1$. At the same time another beam is added that we call *depump*. The depump is resonant with the transition $5S_{1/2}, F = 2 \rightarrow 5P_{3/2}, F' = 2$ and it has the effect of increasing the decay rate into the dark state, since it adds another transition path to that state. Furthermore the depump beam is shaped in the "negative" of the repump, i.e. the depump light occupies the "hole" left in the repump. This is because we only want to increase the decay to $5S_{1/2}, F = 1$ in the center of the trap where the repump is not present. This phase of the experiment last 300 ms. The resulting atomic cloud is formed by $5 \cdot 10^7$ atoms in the $5S_{1/2}, F = 1$[29] state with density $5 \cdot 10^{10}$ atoms/cm^{-3} but that in previous experiments reached values up to 10^{12} atoms/cm^{-3}, which to our knowledge are the higher densities ever measured for a SpOT [126]. All the relevant transitions energy levels for the SpOT process are shown in Fig. 3.7.

The SpOT phase is the last stage of the preparation before the proper experiment takes place. At this point, the atomic cloud will be slowly expanding due to the low temperature, while the atoms are in the desired dark state. Thus I can conclude the section on atom trapping and introduce the light beams which are used by us to probe the atoms and perform the experiment.

3.3 Orbital Angular Momentum generation with Q-plate

In the previous Sec. 2 I have introduced the concept of vectorial light fields and presented the research topic of the interaction of this kind of light with atomic systems. Here I

[29] A percentage between 10% and 20% of the atoms are in the other state $5S_{1/2}, F = 2$ that due to the random nature of the spontaneous decay cannot be completely transferred to the dark state.

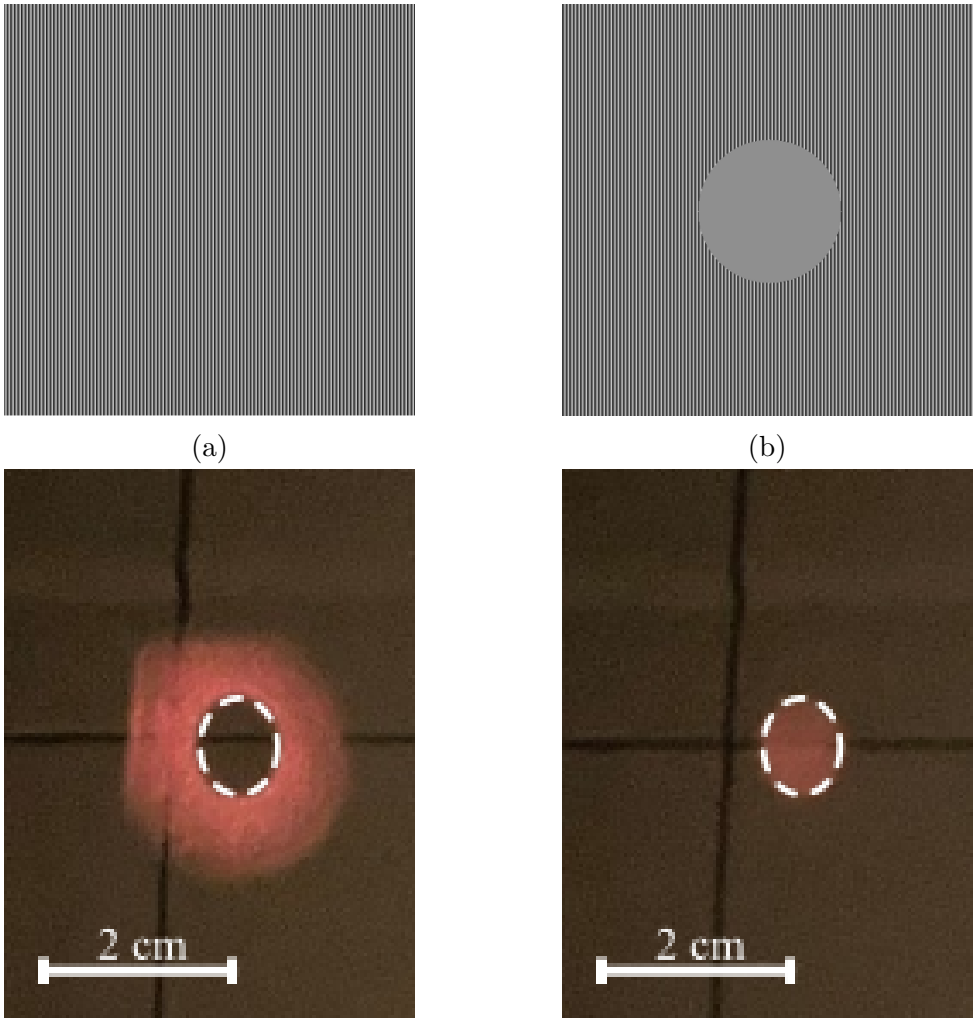

Figure 3.12: Holograms acting on repump and depump beam. The optical path is so that the repump light that reaches the atoms is the 1^{st} order of diffraction from the SLM, while the depump light is the 0^{th} order. (a) Regular hologram with diffraction grating pattern. The repump beam is unmodified and the depump is blocked. (b) Grating with circle. The area with no grating subtracts light to the repump and allows the depump to go through. (c-d) Image of repump and depump just before glass cell. Note how the depump fills the "hole" of the repump.

will focus just on the properties of the beam that was used in the experiment and the experimental configuration responsible for its generation, the *Q-plate*.

A Q-plate [68] is a liquid crystal passive optical element that modifies Spin Angular Momentum in a beam so that it generates Orbital Angular Momentum. It is characterized by the q number that imprints a phase onto the two circular polarisation such that they acquire $+\ell = 2q$ and $-\ell = 2q$, for σ_+ and σ_- respectively. The principle of operation is similar to an half-wave plate in which the orientation changes azimuthally, i.e. the optical axis varies continuously going around the center. And similarly to wave plates, the effect of Q-plates is wavelength dependent so they need to be crafted for specific light frequency usage[30].

The input beam that we send to the Q-plate is just a standard linearly polarized beam. However any linearly polarized beam can be expressed as an equal sum of two circularly polarized beams:

$$\mathbf{E}_{\text{in}}(r,\phi) = E_0(r)\hat{x} = \frac{E_0(r)}{\sqrt{2}}(\hat{\sigma}_+ + \hat{\sigma}_-), \tag{3.12}$$

where the amplitude $E_0(r)$ is standard Gaussian profile. In addition, for our purposes it does not matter the actual polarisation orientation, as long as it is linear. After passing through the Q-plate

$$\mathbf{E}_{\text{q}}(r,\phi) = \frac{E_q(r)}{\sqrt{2}}(e^{-i2q\phi}\hat{\sigma}_- + e^{+i2q\phi}\hat{\sigma}_+). \tag{3.13}$$

The amplitude profile $E_q(r)$ is not equivalent to $E_0(r)$. In fact, due to the spatial distribution of the phase which has a singularity in the middle [127], the field propagates so that the amplitude distribution assumes the form of a toroid or in colloquial terms a "doughnut", which is typically associated to a LG beam[31] [37,38]. The transformation of the amplitude from Gaussian to LG is also the main factor to determine the efficiency of the Q-plate. As we mentioned previously, since the Q-plate is only a passive element it can not generate light, so it is the overlap between the amplitude of $E_0(r)$ and the various LG modes present in $E_q(r)$ that dictates the efficiency of the transformation: as a general rule of thumb for the higher ℓ generated by Q-plates with the larger beam waist the efficiency

[30] Another possibility is to apply an AC voltage through the Q-plate to modify the liquid crystal orientation in order to create the specific phase delay to match with the wavelength used. In our case this was not necessary as the Q-plates were custom made in the University of Naples by the group lead by Prof. Marrucci [68] for our light frequency.

[31] More specifically in our case is a collection of LG fields with the same OAM but different radii

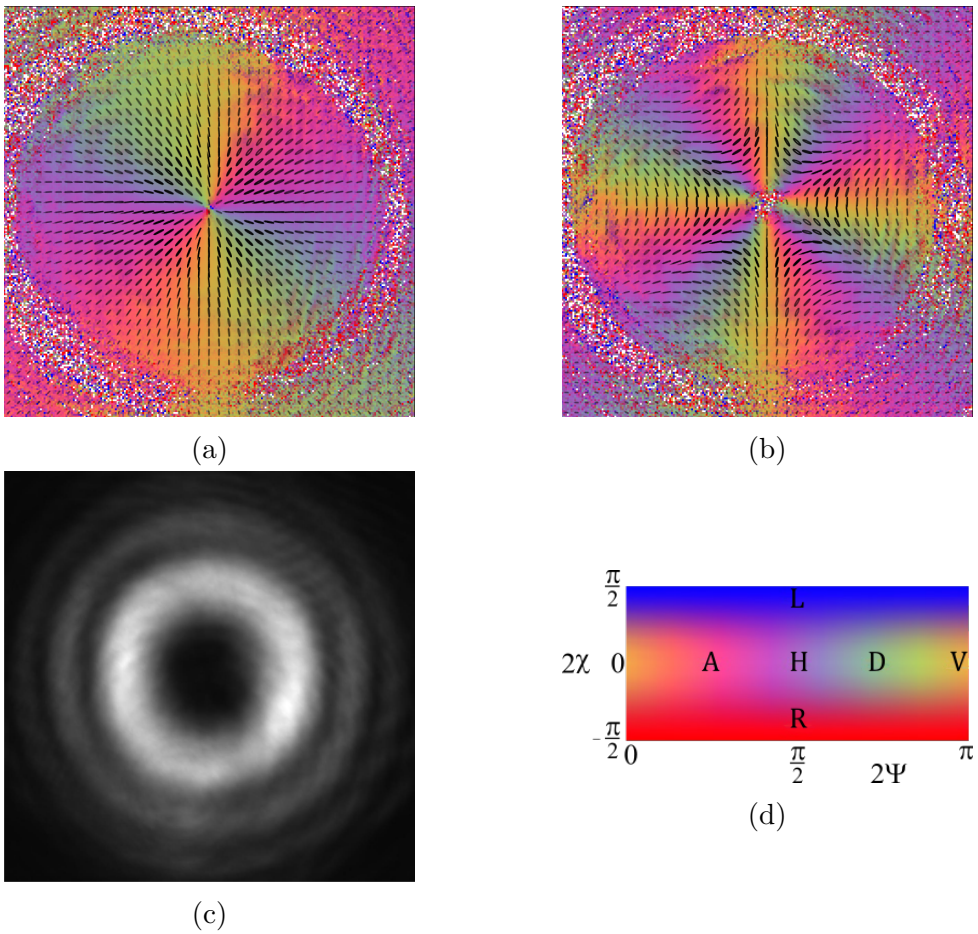

Figure 3.13: Polarisation pattern of Q-plate generated beams calculated with 6 Stokes measurement. (a)q=1 (b)q=2. (c) Intensity image. (d) Colour map for the polarisation.

decreases.

In Fig. 3.13 it is shown an example of the electric field polarisation pattern associated to the Q-plate generated beams.

In this section I described the setup that generates the probe light, which is the last of the experimental ingredients that I needed to introduce. Now the reader should have knowledge of all the necessary elements present in the setup and that will be combined to perform the experiment[32]. In Fig. 3.14 are shown all the elements forming the lab setup, as well as the optical path of the many different beams, to give a visual idea of the experiment to the reader. Fig. 3.15 is the equivalent real life image of the optical setup.

[32]Like a sort of a scientific "ritual".

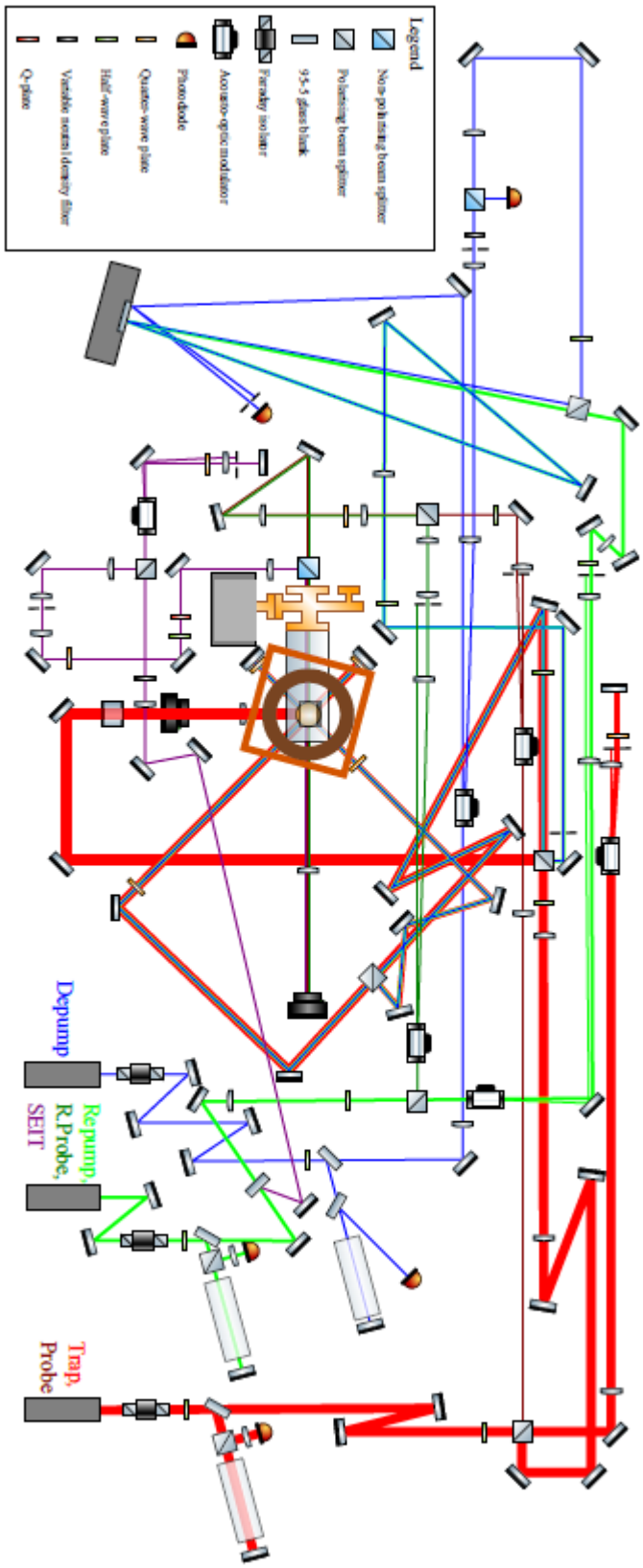

Figure 3.14: Diagram of the experimental setup. All but one of the optical path are at the same elevation, the other being one of the trap beam responsible for the trapping in the vertical direction. Image made by Ádám Selyem, taken from [89].

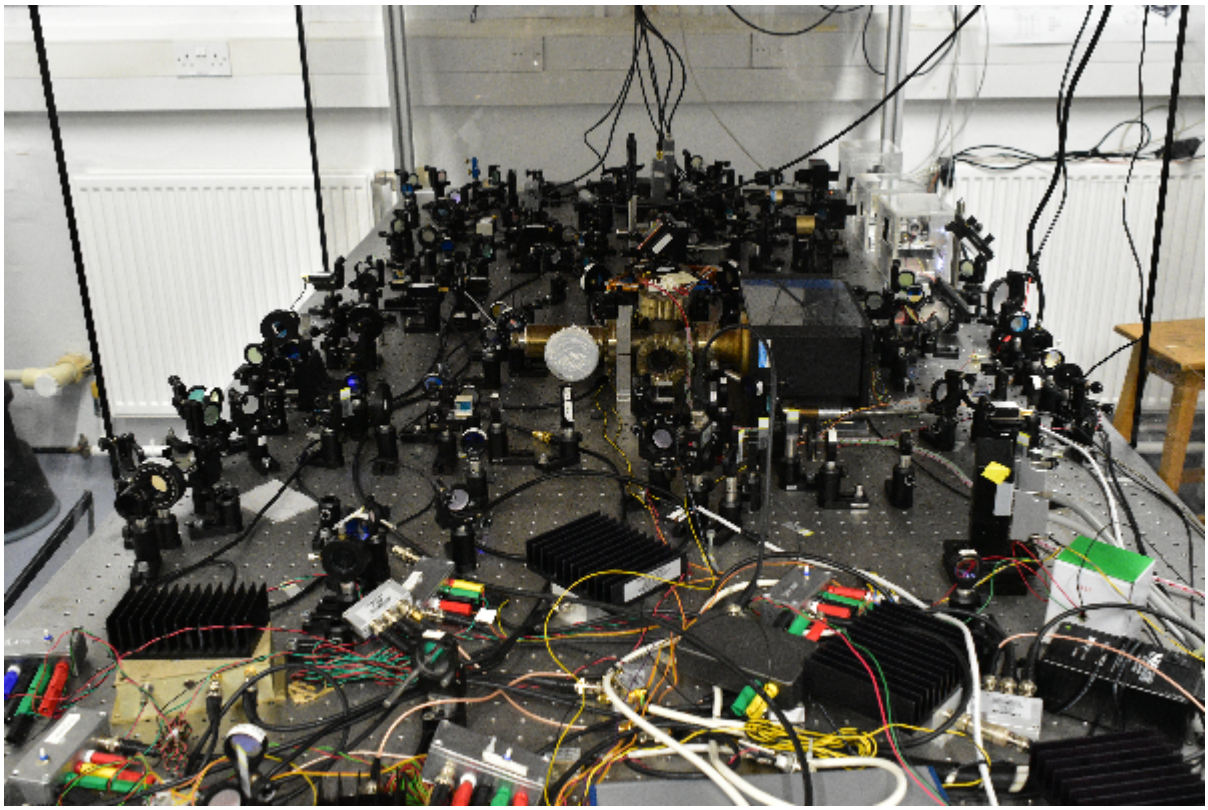

Figure 3.15: Photo of the optical table. At the center can be noticed the vacuum cell with the ion pump on its right.

Chapter 4

Θέσιζ (Thesis)

In this chapter I want to summarize the main part of the theory and supporting models for the experimental system and phenomena at the center of my research. In Sec. 4.2 I will first talk about the interaction between coherent light and atoms. The strong interaction that atoms manifest when subjected to coherent radiation on resonance is the main reason why this branch of research is so well studied [106]. In addition, the fact that atoms of the same element species and isotope are indistinguishable from one another has the double advantage of ensuring reproducibility of the experiment[1] and that the interaction is enhanced further by collective effects [129].

In particular I will be focusing on the element of rubidium. I mentioned early in Sec. 3.2.1 why this particular kind of atom is so commonly used in experimental atom optics. Being the easiest to cool and trap is due firstly because Rb atoms possess an hydrogen-like structure [24]. Meaning that there is only one electron in the most external shell and thus the atom can be approximated as an "heavier" hydrogen atom, especially when interacting with light frequencies in the visible and IR spectral range. But then Rb has an advantage over all the lighter alkali metals as well as hydrogen given because the heavier nucleus decreases the velocity linked to the recoil energy in the MOT process. Lastly, the final advantage related to the use of RB, is that the coherent laser sources emitting in the range of the frequency of the Rb MOT transitions are cheap and more easily available due to the development of semiconductor diode laser[2].

[1] Apart from corrections due to general relativity, the frequency of a cesium atom is the same in Glasgow or in Buenos Aires. That is why atomic clock are the standard for time measurement [128].

[2] In particular, the linewidth of the diode for the DVD reader is at 780 nm, conveniently close to the Rb lines.

After the introduction of the light matter interaction we will discuss how the information on the interaction can be extrapolated through the analysis of the absorption of light Sec. 4.4. This will set the stage for the introduction and of the two different predicting model used in the experiment, the Fermi's Golden Rule (Sec. 4.5) with the Optical Bloch equation. Both those models of the system have been developed by a former Ph.D. student of our group, Thomas Clark, and discussed extensively in his thesis [130]. The dark states derived from the Hamiltonian can be spatially located with the absorption images of the probe beam. The distinction between the dark states can also be intuitively suggested, as we shall see by looking at the local orientation of the optical polarisation of the probe. At the end of this chapter, the importance of the relative alignment of the light polarisation and the magnetic field will also been shown as a significant simplification of the model Hamiltonian could be obtained by placing the quantization axis to be always collinear to the magnetic field direction Sec. 4.5.1.

4.1 Energy levels of rubidium

There are two isotope of rubidium that are naturally found: ^{85}Rb and ^{87}Rb with $72,2\%$ and $27,8\%$ relative abundance respectively. In our experiment we make use only of ^{87}Rb so whenever rubidium is mentioned we refer to this isotope, unless explicitly mentioned.

The simplest way to treat rubidium, or any other hydrogen-like atom, is as a nucleus with one electron orbiting it. The rest of the electrons fill the inner shells completely and for the scopes of our research only two orbits, or more correctly orbitals, of the same energy levels are necessary to be considered. These are the $5S$ and $5P$, with the angular quantum number L being 0 and 1 respectively. The S orbital acts as the ground state with lower energy and is separated in energy from the P by $2.6 \cdot 10^{-18}$ J. This way of measuring the energy difference is not really used in optics and it is much more common to refer the frequency or the wavelength of the correspondent photon with the same energy, that in this case translate to ~ 380 THz or ~ 790 nm.

In addition to the angular quantum number of the orbitals, the energy levels are also affected by the internal spin of the electron so the spin angular quantum number can take the values of $S = \pm 1/2$. This additional spin couples with the angular momentum giving rise to the spin-orbit coupling. The total electronic angular momentum is then expressed

as $\mathbf{J} = \mathbf{L} + \mathbf{S}$ [3]. The quantum number $|\mathbf{J}|$ can take values between $|L - S| \leq J \leq L + S$. This means that the S state can only $J = 1/2$ value. However the P state splits in two different levels with $J = 1/2$ and $J = 3/2$. This is commonly referred as fine splitting, that in the same units of measure expressed before is in the order of 7 THz or 15 nm[4].

The last spin that needs to be taken into account is the one that arises from the nucleus of the atom $\mathbf{I}$. This also couples together with the other angular momentum leading to the total atomic angular momentum $\mathbf{F} = \mathbf{J} + \mathbf{I}$, which follows the same rules as J and can take again values between $|J - I| \leq F \leq J + I$. The sublevels for the different F values cause an additional splitting of the energy levels which is called hyperfine splitting. For ^{87}Rb the nuclear quantum number is $I_{87} = 3/2$ [5]. The effect on the states that we mentioned previously are that the ground state $5S_{1/2}$ splits in two different hyperfine state $F = 1$ and $F = 2$ that are separated by 6.8 GHz in frequency. The $5P_{1/2}$ also splits in two states while the $5P_{3/2}$ has 4 different sublevels. The typical energy separation for the P sublevels is of the order of a few hundred of MHz.

The splitting mentioned until now are all due to the internal variables and components of the atoms. But there is an additional factor that can modify the energies and also the quantity of atomic levels in the form of the external magnetic field[6]. Each hyperfine level contains $2J+1$ magnetic sublevels which are commonly labeled with the quantum number m_F going from $-J \leq m_F \leq J$. In the absence of magnetic fields the magnetic sublevels are degenerate. But as the magnetic fields appear they start to split due to the Zeeman shift in energy. This shift is given by

$$\Delta E_{m_F} = \mu_B g_F m_F B_z, \tag{4.1}$$

where μ_B is the Bohr magneton and B_z is the magnitude of the magnetic field along the z direction. The Landé g-factor g_F is what changes the effect for the different levels and

[3]Here we remind that angular momenta are vectors

[4]To clarify, this wavelength value corresponds to the relative difference between photon wavelengths resonant with the transitions from the same starting state and the two P states as the final states. It does not mean that a photon with 15 nm of wavelength has the same energy of the fine splitting.

[5]The main differences between the energy levels of the two isotope of rubidium are mainly due to the difference in nuclear spin ($I_{85} = 5/2$). The other factor changing the energy separation between different levels is of course the weight of the nuclei.

[6]Note that electric field can also create splitting like in the Stark effect, but is not relevant in our investigation so we will not discuss it.

can be approximated as

$$g_F = g_J \frac{F(F+1) - I(I+1) + J(J+1)}{2F(F+1)} \tag{4.2}$$

with

$$g_J = 1 + \frac{J(J+1) - L(L+1) + S(S+1)}{2J(J+1)},$$

For the typical magnetic field strengths involved in our experiment, the Zeeman shift is much smaller than the other energies for the splittings that have mentioned before. Sublevels in the same manifold are separated by 0.5 MHz per Gauss on average and even the larger separation of the two extreme $5P_{3/2}, F = 3$ $m_F = \pm 3$ is less than 10 MHz at 1 G, which is comparable to the natural linewidth Γ of the transition. So when taking account of just the energy separation the magnetic sublevels are not resolvable by our laser sources, while all the other types of splitting can be addressed. But there is another parameter to take into account. In fact the polarisation of the light can be used to recover the distinction between m_F levels and takes a central role in our experiment.

This brief summary of the rubidium atomic level can be found in more detail in [24].

4.2 Light matter interaction Hamiltonian

The best instrument at our disposal to act on the atomic energy levels described above is through the light interaction, in particular the phenomena of absorption and emission. In the previous experimental chapter we discussed already on the practical aspect of the interaction between coherent light and rubidium atoms such as saturated absorption spectroscopy Sec. 3.1.2 and Doppler cooling Sec. 3.2.1. Thus here we are going to focus more on the theoretical aspect of the absorption.

Let us now consider an atom with two levels, ground with $F = 1$ and excited with $F = 0$, continuously exposed to laser light. These levels are further divided in magnetic substates that are degenerate or with negligible difference in energy. This sublevels can still be distinguished with the help of the polarisation of the incident field. If the beam light is unpolarized, then all the magnetic sublevels can absorb light and transfer to the excited state. Instead if only one specific polarisation is present, the atoms will be optically pumped and the system will be well approximated by a two-level system. As a bit of fore-

shadowing the interpretation is also valid if the polarisation is locally defined but spatially will be different in different parts of the beam, as it happens for the q-plate beam.

To describe analytically the interaction we can make use of the density operator. The general state to describe a two-level atom can be written as $|\Psi\rangle = c_g |g\rangle + c_e |e\rangle$, where $|g\rangle$ is the ground and $|e\rangle$ is the excited state with their respective probability amplitudes. The density operator is defined as $\hat{\rho} = |\Psi\rangle \langle\Psi|$. For clarity, it can be also expressed in matrix form:

$$\hat{\rho} = \begin{pmatrix} \rho_{gg} & \rho_{eg} \\ \rho_{ge} & \rho_{ee} \end{pmatrix} = \begin{pmatrix} c_g c_g^* & c_e c_g^* \\ c_g c_e^* & c_e c_e^* \end{pmatrix} \tag{4.3}$$

The diagonal elements of the density matrix, ρ_{gg} and ρ_{ee}, are known as *populations* of the states $|g\rangle$ and $|e\rangle$ respectively. They are the probability of the atom to be in that particular state in case of a measurement. Since the probability of finding the atom in any of the state is 1, the some of the diagonal elements must be 1. The other terms, ρ_{ge} and ρ_{eg}, are known as *coherences*. Those depends on the phases between the complex amplitudes of the states and are related to the transition probabilities between the states. These definitions are not limited to the case of two-level atoms but can be extended to the multi level scenario in a straightforward manner.

The density matrix only describes the system at a certain point in time. To take account of its evolution, especially the effect given by the absorption and spontaneous emission of light photons, the von Neumann equation is used:

$$\frac{d\hat{\rho}}{dt} = \frac{i}{\hbar} \left[\hat{\rho}, \hat{H} \right], \tag{4.4}$$

where $\hat{H}$ is the system Hamiltonian.

There is still something missing from the Hamiltonian to describe the system nicely. The spontaneous emission has surely an active and substantial effect on the evolution of the atomic populations but it cannot be described easily in the Hamiltonian form. Fortunately we can still incorporate its effect in terms of the density matrix. The spontaneous emission can be written as a rate of decay for the population of the excited state, using the inverse of the lifetime of the state Γ as its value. Since the excited state population will decay to the ground state so the rate of decay is a growth for the ground state population. So in addition to the terms that we have already considered, we have in the density matrix the

terms:

$$\frac{d\rho_{ee}}{dt} = -\frac{d\rho_{gg}}{dt} = ... - \Gamma\rho_{ee}. \tag{4.5}$$

The coherences as well are affected by a rate of decay[7]:

$$\frac{d\rho_{eg}}{dt} = ... - \frac{\Gamma}{2}\rho_{eg} \text{ and } \frac{d\rho_{ge}}{dt} = ... - \frac{\Gamma}{2}\rho_{ge}. \tag{4.6}$$

Now we can combine Eq. 4.4, 4.5 and 4.6 to express the entire evolution time evolution for the density matrix:

$$\frac{d\hat{\rho}}{dt} = \frac{i}{\hbar}\left[\hat{\rho}, \hat{H}\right] + \begin{pmatrix} \Gamma\rho_{ee} & -\frac{\Gamma}{2}\rho_{eg} \\ -\frac{\Gamma}{2}\rho_{ge} & -\Gamma\rho_{ee} \end{pmatrix}. \tag{4.7}$$

Now we should find an expression for the system Hamiltonian. First of all we can write the time evolution of the state $|\Psi\rangle$ with the Schrödinger equation:

$$i\hbar\frac{\partial\Psi(\mathbf{r},t)}{\partial t} = \hat{H}\Psi(\mathbf{r},t) \tag{4.8}$$

with the atomic wavefunction being

$$|\Psi\rangle(\mathbf{r},t) = c_g(t)|g\rangle + c_e(t)|e\rangle e^{-i\omega_0 t}$$

The Hamiltonian terms that are relevant for us are the one that govern the interaction between atom and light, and in this regard the dipole interaction is sufficient, in addition to the interaction between the atom and magnetic fields.

Let us concentrate on the electric dipole first $\mathbf{D}\cdot\mathbf{E}$. The laser light that is being used can be considered monochromatic[8], so it can be written in the simple form $\mathbf{E} = E\exp[-i\omega t]\hat{e}$, ignoring the space dimension for now and concentrating only on the time oscillation. The photon absorption (stimulated emission) transfers the atom from the ground (excited)

[7] Causing the phenomenon of decoherence.

[8] At least in respect to the linewidth of the states

state to the other. So the time evolution for the complex amplitudes $c_{g,e}$ are:

$$\begin{aligned} i\hbar\frac{dc_g}{dt} &= -c_e \langle g| \mathbf{D}\cdot\mathbf{E} |e\rangle e^{+i\omega_0 t} \\ i\hbar\frac{dc_e}{dt} &= -c_g \langle e| \mathbf{D}\cdot\mathbf{E} |g\rangle e^{-i\omega_0 t} \end{aligned} \tag{4.9}$$

with the term $\langle g| \mathbf{D}\cdot\mathbf{E} |e\rangle$ being the compressed form of the expression

$$-\frac{\langle g| \mathbf{D}\cdot\mathbf{E} |e\rangle}{\hbar} = -\frac{\langle g| \left(\mathbf{d}^*_{ge} |e\rangle \langle g| + \mathbf{d}_{ge} |g\rangle \langle e|\right)\cdot\left(\mathbf{E}_0 e^{-i\omega t} + \mathbf{E}^*_0 e^{i\omega t}\right) |e\rangle}{\hbar} \tag{4.10}$$

$$= -\frac{\mathbf{d}_{ge}\cdot\left(\mathbf{E}_0 e^{-i\omega t} + \mathbf{E}^*_0 e^{i\omega t}\right)}{\hbar} = \Omega_R e^{-i\omega t} + \tilde{\Omega}_R e^{i\omega t} \tag{4.11}$$

with the Rabi frequencies $\Omega_R = -\mathbf{d}_{ge}\cdot\mathbf{E}_0/\hbar$ and $\tilde{\Omega}_R = -\mathbf{d}_{ge}\cdot\mathbf{E}^*_0/\hbar$. From the specular term $\langle e| \mathbf{D}\cdot\mathbf{E} |g\rangle$, we similarly obtain $\Omega^*_R = -\mathbf{d}^*_{ge}\cdot\mathbf{E}^*_0/\hbar$ and $\tilde{\Omega}^*_R = -\mathbf{d}^*_{ge}\cdot\mathbf{E}_0/\hbar$. The Rabi frequency can be interpreted as the effective strength of the light-atom interaction and is a frequency. It depends on the intensity of the light, since $I = |E|^2$, and the dipole matrix element. Since the latter is fixed for every transition, the Ω can be considered as an equivalent indication of the light intensity.

Rewriting Eq. 4.9 in terms of the various Ω_R we get:

$$\begin{aligned} i\hbar\frac{dc_g}{dt} &= c_e\hbar\left(\Omega_R e^{-i(\omega-\omega_0)t} + \tilde{\Omega}_R e^{i(\omega+\omega_0)t}\right) \\ i\hbar\frac{dc_e}{dt} &= c_g\hbar\left(\Omega^*_R e^{i(\omega-\omega_0)t} + \tilde{\Omega}^*_R e^{-i(\omega+\omega_0)t}\right), \end{aligned} \tag{4.12}$$

The usual next step to simplify is to consider the two oscillating terms with frequencies, $\Delta = \omega - \omega_0$, also called detuning and $\omega + \omega_0$, in Eq. 4.12. Close to resonance, i.e $\omega \sim \omega_0$, the former is very small whereas the latter doubles. When considering this in a time evolution, the counter rotating term $\tilde{\Omega}_R$ will perform many cycles that average to 0 and the evolution will follow slower oscillating term. This is well known as the *Rotating Wave Approximation* [131]. After this simplification, Eq. 4.12 takes a much manageable form

$$\begin{aligned} i\hbar\frac{dc_g}{dt} &\approx c_e\hbar\Omega_R e^{-i\Delta t} \\ i\hbar\frac{dc_e}{dt} &\approx c_g\hbar\Omega^* e^{i\Delta t}. \end{aligned} \tag{4.13}$$

The last passage to obtain the time-independent Hamiltonian is to modify the complex amplitude so that includes the oscillation term in the Eq. 4.13. This in practice means

that the complex amplitudes forms a new basis that is translated in a frame of reference that is co-rotating with the light field. To do this is sufficient to use the new definitions $c'_g = c_g$ and $c'_e = c_e e^{i\Delta t}$, rewriting Eq. 4.13 as

$$\begin{aligned} i\hbar\frac{dc'_g}{dt} &\approx c'_e\frac{\hbar\Omega}{2} \\ i\hbar\frac{dc'_e}{dt} &\approx c'_g\frac{\hbar\Omega}{2} - c'_e\hbar\Delta, \end{aligned} \tag{4.14}$$

where we also implied $\Omega = \Omega^*$, since we care only about local effect and can thus ignore global phases for now. Then we can express the time-independent Hamiltonian in matrix form:

$$\hat{H} = \frac{\hbar}{2}\begin{pmatrix} 0 & \Omega \\ \Omega & -2\Delta \end{pmatrix} \tag{4.15}$$

and then substitute it in Eq. 4.4 so that we can obtain the optical Bloch equation for a two level atom:

$$\begin{aligned} \frac{d\tilde{\rho}_{gg}}{dt} &= \frac{i\Omega}{2}(\tilde{\rho}_{ge} - \tilde{\rho}_{eg}) + \Gamma\tilde{\rho}_{ee} \\ \frac{d\tilde{\rho}_{ee}}{dt} &= -\frac{i\Omega}{2}(\tilde{\rho}_{ge} - \tilde{\rho}_{eg}) - \Gamma\tilde{\rho}_{ee} \\ \frac{d\tilde{\rho}_{ge}}{dt} &= -\frac{i\Omega}{2}(\tilde{\rho}_{ee} - \tilde{\rho}_{gg}) - i\Delta\frac{\Gamma}{2}\tilde{\rho}_{ge} \\ \frac{d\tilde{\rho}_{eg}}{dt} &= \frac{i\Omega}{2}(\tilde{\rho}_{ee} - \tilde{\rho}_{gg}) + i\Delta\frac{\Gamma}{2}\tilde{\rho}_{eg} \end{aligned} \tag{4.16}$$

where we modified the density matrix element with the same principle of using them in the same co-rotating reference frame, e.g. $\tilde{\rho}_{eg} = \rho_{eg}e^{i\Delta t}$. Note that since the sum of $\tilde{\rho}_{gg} + \tilde{\rho}_{ee} = 1$ at all times then the sum of the first two time evolution in Eq.4.16 is 0.

The solution of the optical Bloch equation is analytical in some special cases but usually the solution needs to be computed numerically. Unfortunately this is the case for the system at hand.

Usually the observable that is used to compare the experimental data and the model is the steady-state population of excited state $\tilde{\rho}_{ee}$, since it is linked by a proportional factor to the absorption of a probe beam. This is the case if the absorbed photons from the probe can only be absorbed and cause the transition to this state of the atom, which is the case for the transition that we use in the absorption experiment. In another instances, as for example to check the atom number inside the MOT, we can use instead the fluorescence

of the atoms spontaneously decaying from the state. Setting $\dot{\tilde{\rho}}_{ee} = 0$ gives an expression for the steady state excited state population:

$$\tilde{\rho}_{ee}^{ss} = \frac{1}{2}\frac{I/I_{\text{sat}}}{1 + 4(\Delta/\Gamma)^2 + I/I_{sat}}, \tag{4.17}$$

where we have introduced the definition of saturation intensity

$$I_{\text{sat}} = \frac{c\epsilon_0\Gamma^2\hbar^2}{4|\hat{e}\cdot\hat{d}|^2} \tag{4.18}$$

derived from the equivalence $I/I_{\text{sat}} = 2(\Omega/\Gamma)^2$. The fluorescence/scattering rate R_f is simply obtained by multiplying the expression of $\tilde{\rho}_{ee}^{ss}$ from Eq. 4.17 with the decaying rate Γ. Although the expression for R_f has been obtained from a system with a simplified level structure, it can be still used as a base to compare model and data, such as absorption images, if the time scale evolution of the excited state population is dominated by the decay, i.e. $\Gamma >> \Omega$, and the levels involved in the optical decay/absorption are unambiguously identified. The latter condition is met if there is only a single excited state, which is the case in the system at study.

After having introduced the equations and expression to conceptualize the interaction of light and atoms, we can apply them to build an abstract mathematical scheme that more closely resemble to our own experimental system. There are three main additions that needs to be included to reach this goal. A more realistic atomic level structure must be used, since the two-level atom is only an ideal approximation that seldom can be applied to real world elements and molecules. The interaction between atoms and external magnetic field needs to be included in the Hamiltonian since it is as important as the already mentioned electric dipole interaction. Luckily the Hamiltonian formalization helps in the task since the two kind of interaction are similar enough in essence that the addition of the effects of the magnetic field can be taken account without too much theoretical effort[9]. Lastly, the complexity of the electric field intensity, phase and polarisation used to probe the experiment needs to be properly taken into account. This is not conceptually novel but requires a certain degree of rigorous attention when the writing the models equations and matrices or when performing the various operations inherent in this kind of activity,

[9]A different story is the effort necessary to give a qualitative interpretation to the system, and will be unraveled in the following sections considering polarisation of light and magnetic field orientation.

like change of bases, simplifications or substitutions.

4.3 Lambda system

By including additional atomic levels in our study we need to take account of the phenomena that are linked to the mutual influence of the state. In the case of Λ-type level scheme like the one in Fig. 4.1, the phenomenon that occurs is called *Electromagnetically induced transparency* (EIT) [30–32]. In such systems are present two ground states ($|1\rangle\,|2\rangle$) that are not coupled directly to each other[10]. However, they can still indirectly coupled via the excited state $|e\rangle$ with two optical transition, p (probe) and c (coupling)[11]. Associated to the two couplings are the Rabi frequencies Ω_p and Ω_c, respectively, as well as the detuning Δ that is only applied to the probe.

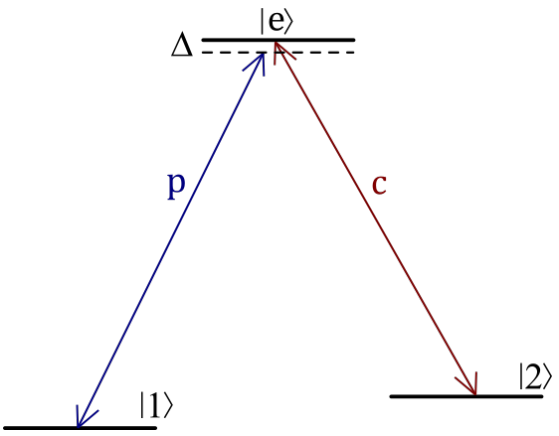

Figure 4.1: Level scheme in the Λ configuration. The two ground state $|1\rangle\,|2\rangle$ are connected only with the excited state $|e\rangle$ by optical transitions. The probe (p) is Δ detuned, while the coupling (c) is on resonance.

To express the evolution of the states we can use the instruments introduced in the previous section like the Hamiltonian. The added complexity though is that the states $|1\rangle\,|2\rangle$ and $|e\rangle$ are not always the eigenstates of $\hat{H}$. Starting from these state as base, the Hamiltonian in Eq. 4.15 can be extended to include the new levels

$$\hat{H} = \frac{\hbar}{2}\begin{pmatrix} 0 & 0 & \Omega_p \\ 0 & 0 & \Omega_c \\ \Omega_p & \Omega_c & -2\Delta \end{pmatrix}. \qquad (4.19)$$

The energy levels of the ground states can be generally different from one another, like in Fig. 4.1 but it does not affect the result other than affecting the frequency of the coupling transitions. Thus, in the discussion I considered the difference to be 0, which is the case for the absorption experiment, since the Zeeman splitting is less than the natural

[10]For now. Later down the track this will change with the introduction of the magnetic coupling.
[11]The name of the optical transitions are conventions descended from the earlier works on EIT and spectroscopy.

linewidth. It is possible then to obtain the eigenstates for $\hat{H}$ that take the form:

$$\begin{aligned} |c_+\rangle &= \sin\alpha \sin\beta\, |1\rangle + \cos\alpha \sin\beta\, |2\rangle + \cos\beta\, |e\rangle \\ |c_-\rangle &= \sin\alpha \cos\beta\, |1\rangle + \cos\alpha \cos\beta\, |2\rangle - \sin\beta\, |e\rangle \\ |g_{\text{unc}}\rangle &= \cos\alpha\, |1\rangle - \sin\alpha\, |2\rangle \end{aligned} \tag{4.20}$$

which are characterized by the mixing angles α and β, defined so that

$$\tan\alpha = \frac{\Omega_p}{\Omega_c} \quad \text{and} \quad \tan\beta = \frac{\sqrt{\Omega_p^2 + \Omega_c^2}}{\sqrt{\Omega_p^2 + \Omega_c^2 + \Delta^2} + \Delta}. \tag{4.21}$$

The calculated eigenstates are dressed state of the bare basis in the presence of light. It is useful to note that while two of them ($|c_+\rangle\, |c_-\rangle$) are a mix of all three state, thus coupling the whole system, $|g_{\text{unc}}\rangle$ is only formed by the ground states and has no link to $|e\rangle$. Therefore this state is a dark state for the light. In fact, in a realistic scenario there is a probability that atoms can be transferred to $|g_{\text{unc}}\rangle$ from the other states (in particular from $|e\rangle$) via spontaneous emission, but after that the atoms cannot interact with the beam anymore, thus becoming transparent, or in other words dark, to the coupling light. It is important to note that the presence of the dark state formed by the two ground states is intimately linked with the simultaneous presence of the two coupling and probe beams. In fact if one p or c was missing the dark state would be trivial, i.e. the ground state which is not coupled, and the balance of the two Rabi frequencies determines as well the proportion of each ground state in the expression of $|g_{\text{unc}}\rangle$. However, the confusing effect of this approach to the solution of $\hat{H}$ it is that is not quite obvious what is the physical interpretation of each of the dressed state.

Mainly, the study of the EIT is usually focused on the parameter of the detuning Δ. The more well known phenomena associated with EIT can be retrieved applying the formalism of the density matrix introduced in the previous pages and taking account of the spontaneous emission. Applying Eq. 4.4 with the Hamiltonian in Eq. 4.19, we can reveal the optical Bloch evolution of the Λ system, including the decay terms in the likewise

manner of Eq. 4.5-4.6:

$$\begin{aligned}
\dot{\tilde{\rho}}_{11} =& -i\frac{\Omega_p}{2}(\tilde{\rho}_{1e} - \tilde{\rho}_{e1}) + \gamma_1\tilde{\rho}_{ee},\\
\dot{\tilde{\rho}}_{22} =& -i\frac{\Omega_c}{2}(\tilde{\rho}_{2e} - \tilde{\rho}_{e2}) + \gamma_2\tilde{\rho}_{ee},\\
\dot{\tilde{\rho}}_{33} =& \, i\frac{\Omega_p}{2}(\tilde{\rho}_{1e} - \tilde{\rho}_{e1}) + i\frac{\Omega_c}{2}(\tilde{\rho}_{2e} - \tilde{\rho}_{e2}) - (\gamma_1 + \gamma)2\tilde{\rho}_{ee},\\
\dot{\tilde{\rho}}_{12} =& (-\gamma_{12} + i\Delta)\tilde{\rho}_{12} - i\frac{\Omega_c}{2}\tilde{\rho}_{1e} + i\frac{\Omega_p}{2}\tilde{\rho}_{e2},\\
\dot{\tilde{\rho}}_{1e} =& (-\gamma_{1e} + i\Delta)\tilde{\rho}_{1e} - i\frac{\Omega_c}{2}\tilde{\rho}_{12} + i\frac{\Omega_p}{2}(\tilde{\rho}_{ee} - \tilde{\rho}_{11}),\\
\dot{\tilde{\rho}}_{2e} =& -\gamma_{2e}\tilde{\rho}_{2e} + i\frac{\Omega_c}{2}(\tilde{\rho}_{ee} - \tilde{\rho}_{22}) - i\frac{\Omega_p}{2}\tilde{\rho}_{21},
\end{aligned} \tag{4.22}$$

and for the missing off-diagonal elements we have $\dot{\tilde{\rho}}_{ji} = \dot{\tilde{\rho}}^*_{ij}$.

It is rather hefty to solve the above equations without any additional approximations, on top of the ones already applied. It is beneficial to notice that if the intensity of the probe is significantly smaller than the coupling, then the dark state features predominantly the state $|1\rangle$, which is the state where the population is going to accumulate, i.e. $\tilde{\rho}_{11} \sim 1$ and $\tilde{\rho}_{22} = \tilde{\rho}_{ee} \sim 0$. In this limit, we can simplify Eq. 4.22 as

$$\begin{aligned}
\dot{\tilde{\rho}}_{12} =& (-\gamma_{12} + i\Delta)\tilde{\rho}_{12} - i\frac{\Omega_c}{2}\tilde{\rho}_{1e} + i\frac{\Omega_p}{2}\tilde{\rho}_{e2},\\
\dot{\tilde{\rho}}_{1e} =& (-\gamma_{1e} + i\Delta)\tilde{\rho}_{1e} - i\frac{\Omega_c}{2}\tilde{\rho}_{12} - i\frac{\Omega_p}{2},\\
\dot{\tilde{\rho}}_{2e} =& -\gamma_{2e}\tilde{\rho}_{2e} - i\frac{\Omega_p}{2}\tilde{\rho}_{21}.
\end{aligned} \tag{4.23}$$

The next step to get an approximate solution, is to notice that the last off-diagonal term $\dot{\tilde{\rho}}_{2e}$ depends linearly on Ω_p, which we assumed to be small. In addition, in the first equation consequently the term $+i\Omega_p/2\ \tilde{\rho}_{e2}$ depends quadratically on Ω_p and thus can be omitted. By doing this we essentially decoupled $\tilde{\rho}_{2e}$ from the other two terms which we can now focus on and try to find a solution for. At the steady state these solution are

$$\begin{aligned}
\tilde{\rho}_{12} =& -\frac{\Omega_c\Omega_p}{\Omega_c^2 - 4(i\gamma_{12} + \Delta)(i\gamma_{1e} + \Delta)},\\
\tilde{\rho}_{1e} =& \frac{2(i\gamma_{12} + \Delta)\Omega_p}{-\Omega_c^2 + 4(i\gamma_{12} + \Delta)(i\gamma_{1e} + \Delta)}.
\end{aligned} \tag{4.24}$$

The reason why the above expressions might indeed prove useful is that there is a relation of proportionality between $\tilde{\rho}_{ij}$ and the complex linear susceptibility of the atoms measured

by a light field coupling the same transition $i \to j$, which can be expressed as the medium refractive index. In particular the absorption of the light is related to the imaginary part of the susceptibility while the dispersion, from which the refractive index is derived, is obtained from the real part of it. To derive this let us consider a non-phase induced by the passing of light inside the atomic medium, then we can modify the oscillating part of the beam as

$$e^{i(\kappa z-\omega t)} = e^{i(\kappa_0 z-\omega t+\phi(z))} = e^{i(n\kappa_0 z-\omega t)} \to n = 1 + \frac{\phi(z)}{\kappa_0 z} \tag{4.25}$$

where n is the refractive index, $\phi(z)$ is the explicit phase induced by the medium and κ_0 is the vacuum wavevector. We can explicitly divide the refractive index in its real and imaginary part $n = n_R + in_I$ then obtain

$$e^{i(n\kappa_0 z-\omega t)} = e^{i(n_R\kappa_0 z+in_I\kappa_0 z-\omega t)} = e^{-n_I\kappa_0 z}e^{i(n_R\kappa_0 z-\omega t)} \tag{4.26}$$

where the final result is a similar oscillating wave which is modulated in amplitude by both n_I and propagation. So by measuring the variation in z of E, our observable, we can extrapolate the refractive index of the medium. In particular

$$n_I = -\frac{1}{\kappa_0 E}\frac{dE}{dz} \text{ and} n_R = 1 + -\frac{1}{\kappa_0}\frac{d\phi}{dz} \tag{4.27}$$

where ϕ is the incoming light phase. Through the application of the Kramers-Kronig relations [130, 132], which are generally true even for fields more complex than the plane wave case presented here, is it also possible to get a relation between the absorption and the dispersion. In Fig. 4.2 is shown the behaviour of the imaginary and real components of $\tilde{\rho}_{1e}$, focusing on the effect due to the presence or absence of the coupling light. This is the main feature EIT, as well as the origin of the name. The atoms become completely transparent to the probe beam at resonance. At the same time the fast variation on the dispersion induces a substantial increase of the refractive index that has been used in the context of slow light [133].

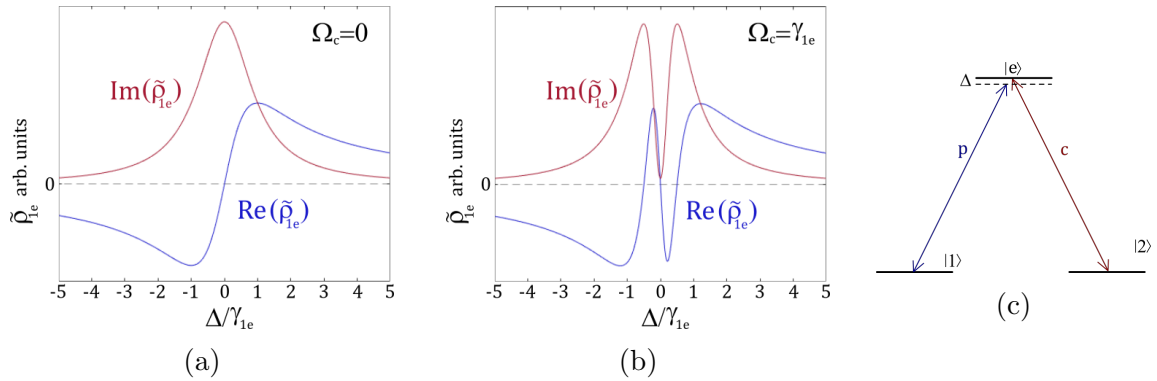

Figure 4.2: Plot showing absorption (proportional to $\mathrm{Im}(\tilde{\rho}_{1e})$) and dispersion (proportional to $\mathrm{Re}(\tilde{\rho}_{1e})$) of the probe light (a) with or (b) without the presence of coupling light on the other transition $|2\rangle \rightarrow |e\rangle$. (c) Level scheme of the lambda system.

4.4 Spatially dependent EIT

Instead of focusing more on the detuning and the temporal domain of the interaction, from this point on we shall diverge from the usual approach of EIT. Part of the difference is inherent to the inclusion of an additional energy-level to the scheme shown in Fig. 4.1. This is actually necessary in order to model a system with close resemblance to the experimental atomic cloud that was "trapped" in Sec. 3.2.4. In the new model system, there are no change for the excited state $|e\rangle$. This is formed by one excited state $5P_{3/2}, F = 0$ and is optically coupled to the ground state in the same fashion as before. The ground state instead is composed by the multifold of three sublevel in $5S_{1/2}, F = 1$. These are distinguished by their Zeeman quantum number m_f: the levels $m_f = \mp 1$ are the analogs of $|1\rangle$ $|2\rangle$, respectively, present in the previous lambda system, while the $m_f = 0$ is the new addition. This level is not directly coupled with the excited state $|e\rangle$[12] although it has a magnetic coupling with the other state $|\pm 1\rangle$.

It is necessary now to have a sidestep discussion outlining briefly the magnetic interaction and how it is formalized in the system Hamiltonian. For an atom in an external electromagnetic field the Hamiltonian interaction can be written as:

$$\hat{H} = -\mathbf{D} \cdot \mathbf{E} - g_F \mu_B \mathbf{F} \cdot \mathbf{B}, \tag{4.28}$$

where $\mathbf{E}$ and $\mathbf{B}$ are the electric vector field and the external static magnetic field while $\mathbf{D}$ and $\mathbf{F}$ are the induced atomic electric dipole and atomic spin polarisation. The terms g_F

[12]In the quantization basis concordant with the propagation direction of the probe.

and μ_B are the Landé g-factor and Bohr magneton respectively. As should be expected, the magnetic part of the Hamiltonian, like the electric dipole one, is strongly dependent on the alignment between the atomic spin and the magnetic field, i.e. is vectorial in nature. That said, the vector representation of $\mathbf{F}$ is directly linked with the choice of quantization axis for the atomic system. In principle, we are free to choose wherever to lay the quantization axis but there are some obvious advantages that propel us towards two possible options. The first option, is to use the $\hat{z}$ axis as the quantization basis for the Zeeman sublevels. This way we retain the same orientation as the laboratory frame of reference and do not need to transform the Stokes vector for the probe polarisation, since it is in the same frame of reference. This option is also the one that was used for most of the modeling and testing of the experiment since it was the most natural approach to the quantization axis decision. In this frame of thought, the magnetic field can then be seen as either longitudinal or transverse in respect to the $\hat{z}$ axis, and the $\mathbf{F}\cdot\mathbf{B}$ interaction takes the form outlined in the following Eq. 4.29, 4.30. The second option is instead to always lay the quantization axis on the same direction as the magnetic field. The adjustments due to this choice will be laid out in Sec. 4.5.1 as we for now go forward in the explanation with the atomic levels quantized along $\hat{z}$.

4.4.1 Longitudinal Magnetic Field

We first consider the case of the magnetic field $\mathbf{B} = B\hat{z}$ aligned in the same axis as the atomic spin $\mathbf{F}$, i.e. the quantization axis and the magnetic field alignment coincide. It should not sound to unfamiliar to the reader since this configuration is the one from which arises the well known Zeeman splitting. To simplify, we can restrict ourselves on the ground state since for the excited state $|e\rangle$ the hyperfine-structure quantum number $F = 0$, hence the magnetic field has no effect on this state[13]. The resulting Hamiltonian accounting for a field directed along the quantization can be written as:

$$\hat{H}_{B_z} = -\frac{\hbar}{2}\Omega_L \left|+1\right\rangle\left\langle+1\right| + \frac{\hbar}{2}\Omega_L \left|-1\right\rangle\left\langle-1\right| \tag{4.29}$$

[13]This is true at least for the strength of the magnetic field that are applied in our investigation.

where we have introduced the Larmor frequency $\Omega_L = g_F \mu_B B$[14]. As it can be seen from Eq. 4.29, the influence of the longitudinal field is to change the energy of ground state sublevels without adding any additional coupling terms in the system. The consequence of this is a change in the resonant frequency for the optical coupling seen in precedent section, thus producing a similar effect as a change in the detuning Δ of the lasers[15], and would be measured as a variation of the absorption/transmission of the related laser light. Since in our system the probe and coupling beam are represented by two orthogonal polarisation of a single laser beam, and thus are both at the same frequency, any disequilibrium in the absorption would result in a net shift of the total polarisation of the beam. For example let us assume our probe (σ_+) and coupling (σ_-) are of equal intensity small respect to I_{sat}, resulting in a beam with overall linear polarisation and some detuning Δ. In the case of Zeeman splitting $\hbar\Omega_L = 2\Delta$ the coupling could be, at the extreme case, completely absorbed and the other would be mostly transmitted, thus the transmitted beam polarisation would change from linear to σ_+. This polarisation change due to differential absorption is commonly known as Voigt effect. However, as mentioned in Sec. 4.1, the energy shift induced by the typical magnitudes of the magnetic field applied in the experiment is small compared to the natural linewidth of the $5S_{1/2}, F = 1 \rightarrow 5P_{3/2}F = 0$ transition (0.7 MHz/G vs 6 MHz), hence this effect alone would not significantly shift from the result obtained from a typical lambda system.

4.4.2 Transverse Magnetic Field

Let us now analyze the presence of a transverse magnetic field in the system and explain how this break the symmetry of the atomic levels. Up to this point, $|0\rangle$ has been a dark state uncoupled to any other state. With the transverse field though a similar mechanism to the standard Larmor precession mixes the ground states. In the usual description for the Larmor precession, the magnetic field is parallel to the spin vector and it couples the external $m_F = \pm 1$ states, transferring the atomic population between them with the time scale given by the Larmor frequency Ω_L. A similar effect of coupling takes place with the transverse magnetic field but linking each state $|\pm 1\rangle$ only with $|0\rangle$. In the Hamiltonian

[14]For the $5S_{1/2}, F = 1$ state the Landé g-factor is $g_F = -1/2$

[15]However in this case the detuning affects both the transitions with opposite sign.

format this takes the form:

$$\hat{H}_{B_\perp} = \frac{\hbar\Omega_L}{2\sqrt{2}} e^{i\varphi_B}(|0\rangle\langle+1| + |-1\rangle\langle 0| + ...), \tag{4.30}$$

where the phase term $e^{i\varphi_B}$ depends azimuthal angle φ_B of the magnetic field on the transverse plane.

Combining Eq. 4.29-4.30 in the general case of

$$\mathbf{B} = B_0(\cos\theta_B\hat{z} + \sin\theta_B\cos\varphi_B\hat{x} + \sin\theta_B\sin\varphi_B\hat{y})$$

we can write the total magnetic interaction Hamiltonian in the matrix form:

$$\hat{H}_B = \frac{\hbar\Omega_L}{2}\begin{pmatrix} \cos\theta_B & \frac{-e^{+i\varphi_B}}{\sqrt{2}}\sin\theta_B & 0 & 0 \\ -\frac{e^{-i\varphi_B}}{\sqrt{2}}\sin\theta_B & 0 & -\frac{e^{+i\varphi_B}}{\sqrt{2}}\sin\theta_B & 0 \\ 0 & -\frac{e^{-i\varphi_B}}{\sqrt{2}}\sin\theta_B & -\cos\theta_B & 0 \\ 0 & 0 & 0 & 0 \end{pmatrix}, \tag{4.31}$$

where we have used the basis $|-1\rangle, |0\rangle, |+1\rangle, |e\rangle$. The important aspect to notice is that the magnetic field direction, rather than the magnitude, is the crucial aspect driving the various couplings and energy shifts.

4.4.3 Vectorial light fields

As we mentioned in the introduction section on EIT, we still need to characterize the complex structured light fields, which are the last element that sets apart our experiments from the more standardized examples of EIT. In particular, the presence of OAM in the light fields compels us to never simplify the polarisation and angular phase of the beams, as both are determining factors in the formulation for the spatial distribution of the vectorial interaction $\mathbf{D}\cdot\mathbf{E}$. And, in reality, it is always the case that is necessary to have the matching condition between the polarisation and atomic level for the transition to occur. However this is usually overlooked as, for homogeneously polarized light fields, that condition is either achieved or not, thus the focus is usually shifted on other parameters of the system, while in our case, to reiterate, this aspect is not so trivial.

After this initial consideration, here I write the expression from the light fields:

$$\mathbf{E}(r,\phi) = \frac{E_0(r)}{\sqrt{2}}\left(\sigma_- e^{-i\ell\phi} + \sigma_+ e^{+i\ell\phi}\right), \tag{4.32}$$

where the amplitude $E_0(r)$ is a toroidal shape amplitude, $\sigma_\pm$ are the circular polarisation each possessing $\ell\hbar$ orbital angular momentum represented by the azimuthal phase factor $e^{\pm i\ell\phi}$. A more comprehensive way to interpret these beams is as a single linearly polarized beam[16], with the polarisation orientation rotating azimuthally by the angular phase factor $e^{\pm i\ell\phi}$. As an example, for the simplest OAM with $\ell = 1$ the beam is radially polarized. Regarding the amplitude, ideally this approaches the LG form. In the experiment though it is more a combination of orthogonal LG mode and Bessel modes, which is the typical result when generating beams with OAM from an initial Gaussian beam.

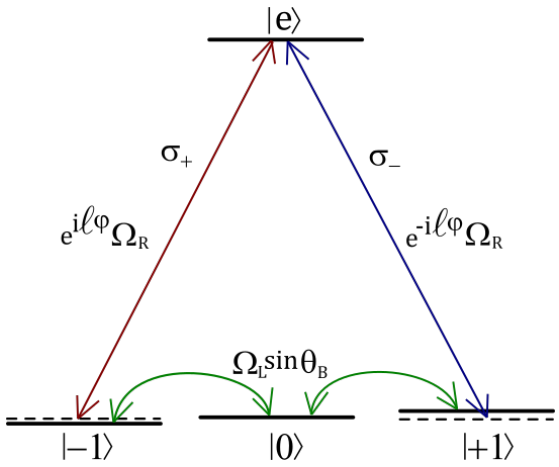

Figure 4.3: Level scheme of the SEIT. The light field only couples $|\pm 1\rangle$ to $|e\rangle$. It is the orthogonal component of the magnetic field that closes the transition cycle, connecting the remaining ground sublevel $|0\rangle$ to the others.

Nevertheless, from the beam intensity profile does not arise any particular effect manifested in the interaction, apart from the obvious requirement that the atom-light interaction occurs only where the light actually is[17]. For now we can leave in the "background" the field intensities, both for the magnetic and the light, as they do not change qualitatively the shape of the interaction and focus on the spatial parameters of the azimuthal phase and orientation of the magnetic field.

With the above consideration in mind, the Hamiltonian for the atomic dipole electric interaction can be written, evolving from 4.19 and including the additional level and

[16]The "single" beam representation follow naturally from the actual experimental generation applied described in 3.3

[17]There also exist atomic interaction with vectorial light fields in which the above requirement is not necessary [134] as the interaction can happen at the phase singularity. Nevertheless this is not the case in my experiments.

the azimuthal phase, as

$$\hat{H}_E = \frac{\hbar\Omega_R}{2}\begin{pmatrix} 0 & 0 & 0 & \frac{1}{\sqrt{6}}e^{i\ell\phi} \\ 0 & 0 & 0 & 0 \\ 0 & 0 & 0 & \frac{1}{\sqrt{6}}e^{-i\ell\phi} \\ \frac{1}{\sqrt{6}}e^{-i\ell\phi} & 0 & \frac{1}{\sqrt{6}}e^{i\ell\phi} & 0 \end{pmatrix}, \tag{4.33}$$

where we have assumed that both beams possess the same frequency, which is resonant with the transition, and the same intensity, i.e. same Rabi frequency Ω_R. The sum of Eq.4.31 and Eq.4.33 gives the total Hamiltonian of interaction

$$\hat{H}_{\text{int}} = \frac{\hbar}{2}\begin{pmatrix} \cos\theta_B\Omega_L & \frac{-e^{+i\varphi_B}}{\sqrt{2}}\sin\theta_B\Omega_L & 0 & \frac{1}{\sqrt{6}}e^{i\ell\phi}\Omega_R \\ -\frac{e^{-i\varphi_B}}{\sqrt{2}}\sin\theta_B\Omega_L & 0 & -\frac{e^{+i\varphi_B}}{\sqrt{2}}\sin\theta_B\Omega_L & 0 \\ 0 & -\frac{e^{-i\varphi_B}}{\sqrt{2}}\sin\theta_B\Omega_L & -\cos\theta_B\Omega_L & \frac{1}{\sqrt{6}}e^{-i\ell\phi}\Omega_R \\ \frac{1}{\sqrt{6}}e^{-i\ell\phi}\Omega_R & 0 & \frac{1}{\sqrt{6}}e^{i\ell\phi}\Omega_R & 0 \end{pmatrix}, \tag{4.34}$$

which is a rather complex Hamiltonian possessing lots of terms and with no obvious transformation to simplify it. In Fig. 4.3 are shown the levels and interaction present in Eq. 4.34. The Bloch equation that are derived from this Hamiltonian, even after those approximations, cannot be analitically solved. It is possible only to obtain a numerical solution as shown in [130], if provided with the appropriate experimental parameters.

4.5 Fermi's Golden Rule

There is however a possible path to simplify the Hamiltonian by selecting a new set of base states. This was first developed in [130] and reported in [9, 135]. In the new basis, the states in the system are connected in a sort of cascade: atoms can go from the lower state to the higher only passing through the other states consecutively. The new levels are $|\Psi_C\rangle$, $|\Psi_1\rangle$, $|\Psi_2\rangle$ and $|e\rangle$ such that:

$$
\begin{aligned}
|\Psi_{C,NC}\rangle &= \frac{1}{\sqrt{2}}\left(e^{i\ell\phi}\,|-1\rangle \mp e^{-i\ell\phi}\,|+1\rangle\right), \\
|\Psi_2\rangle &= \frac{1}{N(\phi)}\left(\cos\theta_B\,|\Psi_{NC}\rangle + \sin\theta_B \sin(\ell\phi-\varphi_B)\,|0\rangle\right), \\
|\Psi_1\rangle &= \frac{1}{N(\phi)}\left(i\sin\theta_B \sin(\ell\phi-\varphi_B)\,|\Psi_{NC}\rangle - \cos\theta_B\,|0\rangle\right),
\end{aligned}
\tag{4.35}
$$

which have the normalisation parameter $N(\phi) = \sqrt{\cos^2\theta_B + \sin^2\theta_B\cos^2(\ell\phi-\varphi_B)}$. There is no need to change the excited state $|e\rangle$, so the new Hamiltonian in the new basis $(|\Psi_1\rangle, |\Psi_2\rangle, |\Psi_C\rangle, |e\rangle)$ takes the form:

$$
\hat{H}'_{\text{int}} = \frac{\hbar}{2}\begin{pmatrix}
0 & i\Omega_L\sin\theta_B\cos(\ell\phi-\varphi_B) & 0 & 0 \\
-i\Omega_L\sin\theta_B\cos(\ell\phi-\varphi_B) & 0 & -\Omega_L N(\phi) & 0 \\
0 & -\Omega_L N(\phi) & 0 & \frac{1}{2\sqrt{3}}\Omega_R \\
0 & 0 & \frac{1}{2\sqrt{3}}\Omega_R & 0
\end{pmatrix}.
\tag{4.36}
$$

As stated above, the main advantage of this basis is that the transition naturally form pair of coupled states. The excited state $|e\rangle$ is optically coupled only with $|\Psi_C\rangle$. This in turn is coupled magnetically to $|\Psi_2\rangle$, but not with $|\Psi_1\rangle$ which only interact with the previous state. However, it needs to be notice that although $|\Psi_1\rangle$, $|\Psi_2\rangle$ and $|\Psi_C\rangle$ are ordered by the transition in a sort of hierarchy, they are not separated in energy. And all of them can be populated from $|e\rangle$ in the case of spontaneous emission. Furthermore, only the optical transition is independent of the angle ϕ, while the other couplings goes to 0 for certain angles $\phi - \varphi_B = (n+1/2)\pi/\ell$, with $n \in \mathbb{N}$. For these set of angles the states $|\Psi_1\rangle$ and $|\Psi_2\rangle$ become dark states producing the same effect of EIT seen in 4.3. The driving parameter of this phenomena is the phase dependence between the two circular polarisation, thus the name Spatially dependent EIT.

We notice that since the final transition to the excited state is light induced and that the excited state population remains negligible, especially in the weak probe approximation, then there is a proportionality between the absorption of the light and the transition probability. In these limit we can obtain a formula to estimate the probability to transition

from $|\Psi_1\rangle \rightarrow |e\rangle$ which can be derived by applying the Fermi's Golden Rule

$$T_{\text{initial}\rightarrow\text{final}} \propto \frac{2\pi}{\hbar}\left|\langle i|\,\hat{H}'_{\text{int}}\,|f\rangle\right|^2 \tag{4.37}$$

, where T is the transition probability rate. The individual transition probability are

$$T_{|\Psi_1\rangle\rightarrow|\Psi_2\rangle} \propto \frac{2\pi}{\hbar}\left|\frac{\hbar\Omega_L}{2}\sin\theta_B\cos(\ell\phi-\varphi_B)\right|^2, \tag{4.38}$$

$$T_{|\Psi_2\rangle\rightarrow|\Psi_C\rangle} \propto \frac{2\pi}{\hbar}\left|\frac{\hbar\Omega_L}{2}\sqrt{\cos^2\theta_B+\sin^2\theta_B\cos^2(\ell\phi-\varphi_B)}\right|^2, \tag{4.39}$$

$$T_{|\Psi_C\rangle\rightarrow|e\rangle} \propto \frac{2\pi}{\hbar}\left|\frac{\hbar\Omega_R}{4\sqrt{3}}\right|^2. \tag{4.40}$$

By applying the FGR, the product of the single transition probabilities become the total transition,

$$T_{|\Psi_1\rangle\rightarrow|e\rangle} \propto \left(\frac{2\pi}{\hbar}\right)^3\left|\frac{\hbar\Omega_R}{4\sqrt{3}}\right|^2\left|\frac{\hbar\Omega_L}{4}\right|^4|\sin\theta_B\cos(\ell\phi-\varphi_B)|^2\,|N(\phi)|^2, \tag{4.41}$$

which can be rewritten as

$$T_{|\Psi_1\rangle\rightarrow|e\rangle} \propto \hbar^3\Omega_L^4\Omega_R^2\sin^2\theta_B\cos^2(\ell\phi-\varphi_B)(\cos^2\theta_B+\sin^2\theta_B\cos^2(\ell\phi-\varphi_B)). \tag{4.42}$$

We should now highlight the dependence of Eq. 4.42 in respect of the magnetic angles φ_B and θ_B. For $\theta_B \ll 1$, the probability varies as a squared sinusoidal function in the variable ϕ with a period of 2ℓ. For the light beams this translate in a transmission with 2ℓ lobes profile, that resembles the petals of a flower.

A change in the angle φ_B will rotate the absorption pattern shifting one lobe to the next, with the pattern returning back to the starting configuration after $\delta\varphi_B = B$. This is easy to understand as φ_B only appears in Eq. 4.42 in tandem with $\ell\phi$, and can be interpret so that the azimuthal angle of the magnetic field is the origin of the azimuthal component of the coordinate system. In fact the magnetic field is what breaks the cylindrical symmetry of the system.

It is somewhat less intuitive understand the alteration of the pattern when departing from the small transverse magnetic field approximation, i.e. when the condition $\theta_B \ll 1$ is not valid anymore. The transmission profile is still sinusoidal at $\theta_B = \pi/2$, which is

the case of magnetic field completely orthogonal to the probe propagation direction, and the number of lobes doubles to 4ℓ respect to the previous longitudinal magnetic field case. With intermediate values of θ_B the absorption pattern is in a transitional stage between the two cases and in particular the "depth" of the transmission is different for the lobes generated by the "splitting". This last effect and the actual profile of the absorption is unfortunately very sensible to the balance between the probe intensity, the OD of the cloud and the magnetic field strength. In Fig. 4.4 is shown a visual representation of the transition probability pattern with varying magnetic field angles and two different OAM values. Although the Fermi's Golden rule is a useful approximation to visualize the expected behaviour of the system, it remains a limit case that can be used to quantitatively predict the data only for certain experimental conditions, i.e. low beam intensity and high OD, which are somewhat inconvenient to obtain in our experiment.

4.5.1 Quantization basis along B

One of the drawbacks of the modified levels exposed in Eq. 4.35 is that besides from $|\Psi_C\rangle$, which is the standard optically coupled state of the typical three level scheme, the other two state $|\Psi_1\rangle$ and $|\Psi_2\rangle$ are not intuitively recognizable as a combination of the three ground states. Hence although we had a model from where to obtain an analytical formula to predict the absorption of the light, we did not have a clear cut physical representation of the dark and bright states for the various magnetic angles directions.

There is however another approach to the system which is intuitive and gives a reasonable prediction for the absorption, which has been explored in [89]. Here I will give the general qualitative idea.

To access this new prospective we first need to change the quantization axis. Instead of fixing it on the direction of propagation of the probe, i.e. the $\hat{z}$ axis, we rely on the direction of the magnetic field as the new quantization for the ground atomic levels. As a starting point let us write again the $\mathbf{B}$ and $\mathbf{E}$ in vector form based on the quantization used up to now:

$$\mathbf{B}(\varphi_B, \theta_B) = B_0 \begin{pmatrix} \sin\theta_B \cos\varphi_B \\ \sin\theta_B \sin\varphi_B \\ \cos\theta_B \end{pmatrix}, \ \mathbf{E}(r, \phi, z) = E_0(r, z) \begin{pmatrix} \cos\ell\phi \\ \sin\ell\phi \\ 0 \end{pmatrix}. \tag{4.43}$$

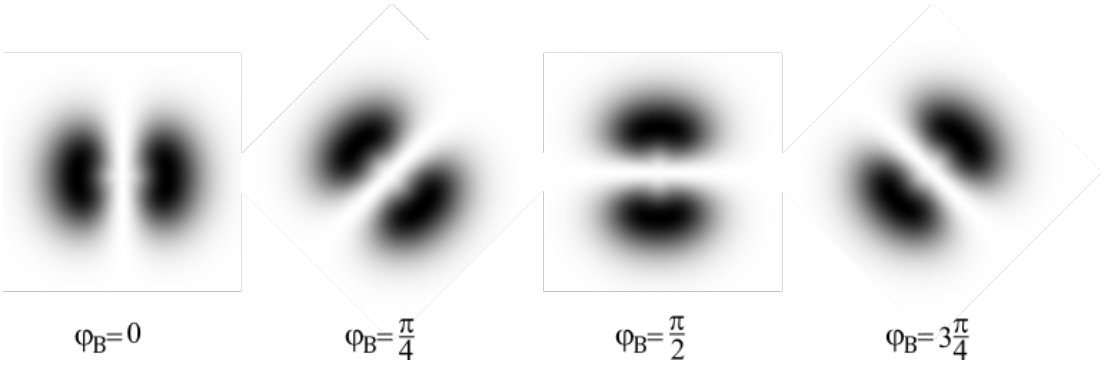

(a)

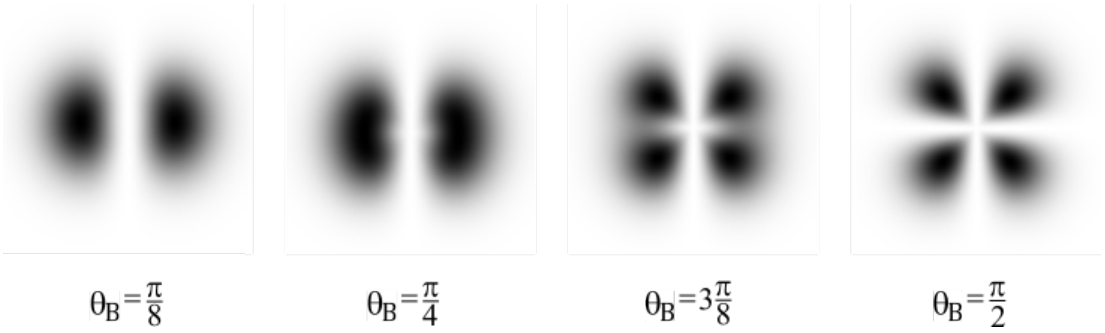

(b)

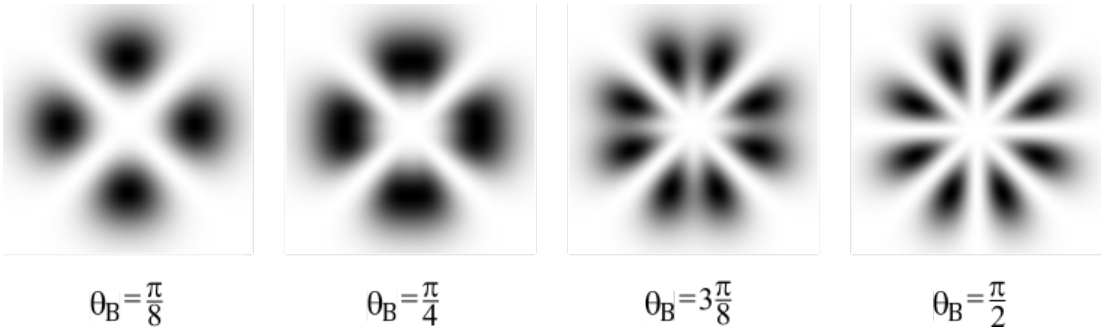

(c)

Figure 4.4: Plot showing transition probability in Eq, 4.42 for different magnetic field angles and probe OAM, with black being high $T_{|\Psi_1\rangle\rightarrow|e\rangle}$ (or in other words high absorption of the probe). In (a) the azimuth angle φ_B is varied while $\theta_B = \pi/8$ and with $\ell = 1$. Otherwise (b) shows varying polar angle θ_B for $\ell = 1$. In (c) as well the polar angle θ_B is varied but for a beam with higher OAM $\ell = 2$.

In this form the electric field completely transverse. This however does not always hold true when we shift the quantization axis based on the magnetic field direction. In general the electric field will retain a linearly polarized component that is transverse with respect to the new axis, which can be divided into a superposition of σ_+ and σ_- polarisations, driving the usual transition that we saw in Eq. 4.33. The addition is represented though by the remaining electric field component along the quantization axis, i.e. is π polarized, that drives the transition $|0\rangle \rightarrow |e\rangle$, since $\delta m_f = 0$ in this case. The strength of these different transitions is directly linked to the intensity of the field in either of the polarisation which can be calculated as,

$$\begin{aligned} I_{||} &= \frac{1}{2} c\epsilon_0 \left(\frac{\mathbf{E}\cdot\mathbf{B}}{B_0} \right)^2 = \frac{1}{2} c\epsilon_0 E_0^2 \cos^2(\ell\phi - \varphi_B) \sin^2\theta_B, \\ I_{\perp} &= \frac{1}{2} c\epsilon_0 \left(E_0^2 - \frac{\mathbf{E}\cdot\mathbf{B}}{B_0} \right)^2 = \frac{1}{2} c\epsilon_0 E_0^2 (1 - \cos^2(\ell\phi - \varphi_B) \sin^2\theta_B). \end{aligned} \tag{4.44}$$

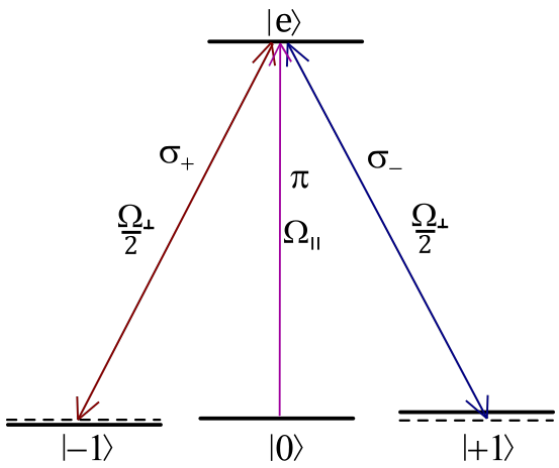

Figure 4.5: Level scheme of the SEIT in the new quantization. The ground state are not coupled by the magnetic state while the light is split into π and σ polarisation.

Although we have slightly complicated the equation for the electric field polarisations, we only need the simplest atomic level representation. In fact, when the quantization axis is aligned with the magnetic field, the ground states are not linked by the magnetic coupling. The only alteration due to the magnetic field is a Zeeman shift. This shift does not influence the optical transition a lot. Firstly the shift only affect the two states $|\pm 1\rangle$. Secondly the detuning added to the two σ transition is the same, although with a different sign. And finally, for the magnetic field strengths generated by us, the Zeeman shift is usually smaller than the natural linewidth of the optical transition. With all these factors in mind, is ad-

vantageous to consider the superposition states,

$$|+\rangle = \frac{|1\rangle + |-1\rangle}{\sqrt{2}} \text{ and } |-\rangle = \frac{|1\rangle - |-1\rangle}{\sqrt{2}}. \tag{4.45}$$

The state $|+\rangle$ is driven by the circular polarisations $\sigma_{\pm}$, while $|-\rangle$ is a dark state. Note that the two states are a simplified version[18] of the coupled and non coupling state $|\Psi_{C,NC}\rangle$ shown in Eq. 4.35.

Thus, we have a system in which we have only optical transitions that act on separate levels based on the ratio of the light polarisations. We can obtain the Rabi frequency of these transitions as:

$$\begin{aligned} \Omega_{||} &= \frac{\Gamma}{2}\sqrt{\frac{I_{||}}{I_{\text{sat}}}} = -\frac{\mathbf{E}\cdot\mathbf{d}}{\hbar}\cos^2(\ell\phi - \varphi_B)\sin^2\theta_B, \\ \Omega_{\perp} &= \frac{\Gamma}{2}\sqrt{\frac{I_{\perp}}{I_{\text{sat}}}} = -\frac{\mathbf{E}\cdot\mathbf{d}}{\hbar}(1 - \cos^2(\ell\phi - \varphi_B)\sin^2\theta_B) \end{aligned} \tag{4.46}$$

where $I_{\text{sat}} = c\epsilon_0\Gamma^2\hbar^2/(4|\mathbf{E}\cdot\mathbf{d}/E_0|^2)$. In Fig. 4.5 is shown the modified level scheme (compared to the one in Fig. 4.3) based on the new quantization.

To obtain a prediction for the absorption or transmission of light, we could then use the same line of reasoning used in the Sec. 4.5, i.e. the steady state population of the excited state $|e\rangle$ which is proportional to the absorption of the light, which can be obtained in the rate equations. This will be developed more thoroughly in a future publication of our group. For now I will just share the preliminary result obtained by Ádám Selyem from the rate equations, which we omit here,

$$P_{|e\rangle} = \frac{-3\Omega_0\cos^2(\ell\phi - \varphi_B)\sin^2\theta_B(-\Omega_L - \Omega_0 + \Omega_0\cos^2(\ell\phi - \varphi_B)\sin^2\theta_B)}{(\Omega_L + \Omega_0)\Gamma + \Omega_0\cos^2(\ell\phi - \varphi_B)\sin^2\theta_B(\Gamma + 3(\Omega_0 + \Omega_L - \Omega_0\cos^2(\ell\phi - \varphi_B)\sin^2\theta_B))}, \tag{4.47}$$

where $\Omega_0 = (\mathbf{E}\cdot\mathbf{d})/(\hbar)$ and Ω_L is the detuning derived from the Zeeman shift of the state $|+\rangle$. This result for the population $P_{|e\rangle}$ comes with a caveat. The Rabi frequency Ω_0 needs to be smaller than Γ, e.g. a good choice for this parameter is $10\Omega_0 \sim \Gamma$.

[18] Since they do not include the azimuthal phase of the light $e^{\pm i\ell\phi}$

Chapter 5

$\Sigma\acute{\upsilon}\nu\theta\epsilon\sigma\iota\zeta$ (Siùnthesis)

In this chapter I will summarize the work related to the main experiment, the details related to its realization, the analysis of the obtained data and a summary of the results, including the ones that were published in [9]. In essence, I will coalesce the work and knowledge described in the previous chapters that supported our principal investigation: the study of the interaction between non trivial atomic states induced by vectorial light fields and a linear magnetic field. In the introduction I explained the motivation and the possible applications that sparked this investigation. To remind the reader, we would like to develop a system that through the manipulation of the magnetic Zeeman states of the Rb atoms can absorb information in the form of either phase or polarisation carried by the light, with the subsequent goal to even store and retrieve later for some amount of time. The results presented in this chapter have helped develop and modify the models reported in the previous chapter, so that we can now have a deeper understanding behind the mechanism of how the atomic states are formed and can be used to infer the magnetic field orientation. Unfortunately, there has been many experimental difficulties not fully seen at the start of the investigation, which are now recognized as part of the complexity of the system. This experimental challenges prevented us to reach the more ambitious goal that was planned at the start of the project: being able to retrieve the atomic state imprinted by the probe light with a different beam from the one that generated it. We still believe that this is possible, and I will present some plans for the future of the experiment that should achieve this goal. I will also rewrite here the probability formula related to

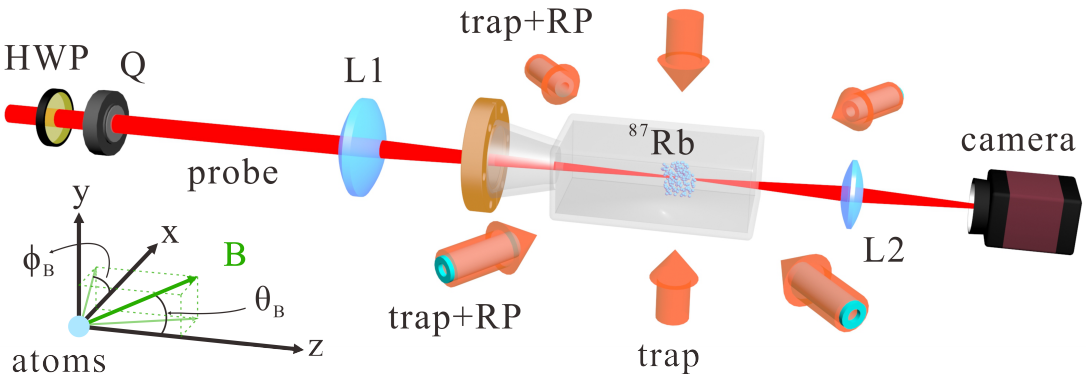

Figure 5.1: Simplified setup of the experiment. **HWP** Halfwaveplate, **Q** Q-plate, **L1**, **L2** telescope lenses. Highlighted are the different propagation axis of the probe beam and the trapping beams. On the left side is shown the frame of reference for the magnetic field **B**.

the absorption, Eq. 4.42

$$T_{|\Psi_1\rangle\to|e\rangle} \propto \hbar^3\Omega_L^4\Omega_R^2 \sin^2\theta_B \cos^2(\ell\phi-\varphi_B)(\cos^2\theta_B + \sin^2\theta_B \cos^2(\ell\phi-\varphi_B))$$

and add a simplified experimental scheme shown in Fig. 5.1 to help the reader in the comprehension of the ultimate discussion regarding the main experiment.

5.1 Experimental procedure

For the realization of the experiment we need a cloud of ^{87}Rb in the ground state $5S_{1/2}$ $F=1$, a probe beam with frequency in resonance with the $5S_{1/2}$ $F=1 \to 5P_{3/2}$ $F=0$ which also is characterized by a vectorial polarisation pattern and magnetic field with fixed orientation. The preparation of those ingredients has been discussed with more detail in Chap. 3, and here it is given for granted. It is still necessary to review them separately before presenting the data, as these elements represents the proper experimental parameters, thus remain crucial to understand the particular prepared setup.

5.1.1 Atomic cloud

Regarding the atomic cloud we try with the best of our knowledge and expertise to maintain a constant number and density of atoms between the different repetitions of the experiment. As a rule of thumb we only perform an experiment and start collecting absorption data if the number of cold atoms, at 100 μK, in the prepared state is on the order

of $0.5 \cdot 10^7$ with a density of $0.5 \cdot 10^{11}$ atoms/cm^{-3}, before expansion. The resulting cloud is quite small in size, ~ 200 μm. Due to the constraints in the geometry of the vacuum cell and the absorption imaging, it would be quite challenging to focus the probe beam to that size without incurring in phase distortions. Thus when performing the experiment we turn off the quadrupole magnetic field and the trapping laser beam to let the atomic cloud expand freely. The typical expansion time is 3.5 ms, which results in a doubling in size of the atomic cloud. This is sufficient to obtain a good contrast in the absorption image, allowing us to use a simple optics system for the probe imaging.

5.1.2 Magnetic field

After the quadrupole magnetic field is turned off, we generate a global $\mathbf{B}$ field with a fixed magnitude. In our experiment we varied this from 0.5 G to 2 G, and the main result that will be shown here was obtained with 1 G. The direction of this field is varied between each set of experiments and the angular direction of the variation is what distinguishes the two categories of data that can be acquired. When we perform a *rotation* experiment we fix the longitudinal component of the magnetic field and vary the azimuth projection, i.e. the component of the magnetic field which is transverse to the propagation direction of the light probe, in the xy plane going from $+x$ to $-x$ in steps of 2.5° to 10°, taking an absorption image at each step. The ratio of $\mathbf{B}_\perp/\mathbf{B}_\parallel$ is a parameter of the experiment. For most experiments we found that $1:1$, i.e. $\theta_B = 45°$, is the one that produces the results with the best clarity. In the other type of *inclination* experiment we fix the total magnitude of the magnetic field and vary its direction on a arc that start from the positive end of the z axis and ends on the negative side of it, i.e. varying the polar angle from 0° to 180°, again in steps of 2.5° to 10° with an absorption image taken at each step. In this case we can choose in which direction to increase the orthogonal component of $\mathbf{B}$ on the overall plane xy. We found that the chosen path does not affect the results and for most experiments we vary $\mathbf{B}$ on the xz plane[1]. The arching paths made by the $\mathbf{B}$ vector during the two kind of experiments can be seen on Fig. 5.2.

[1] In the example in Fig. 5.2b is shown a different path passing through the y axis because it is graphically clearer. But, as said above, the choice of the path does not affect the results.

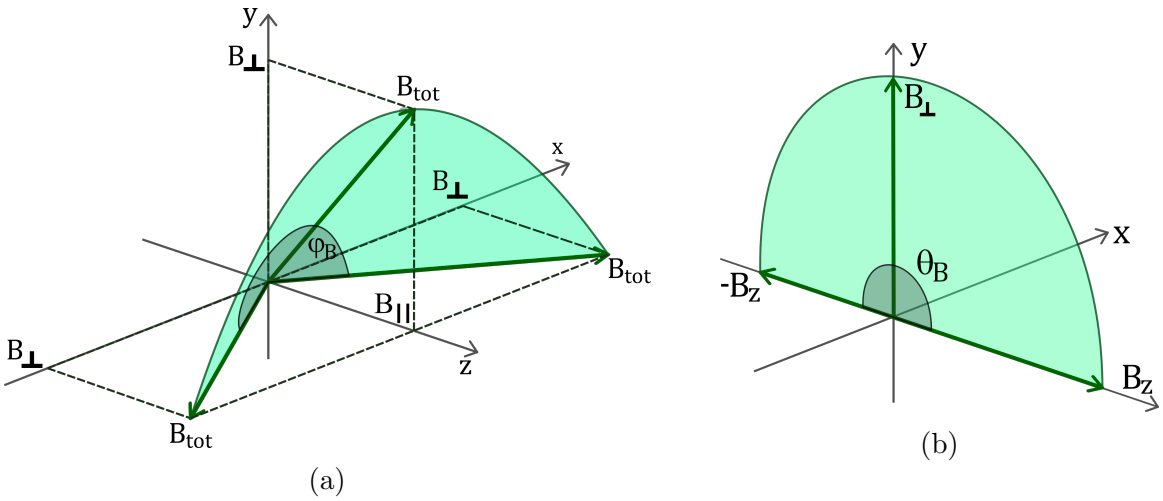

Figure 5.2: **B** field variation for experiments. (a) azimuth variation. (b) polar variation. The green arrows represents **B** at the start, middle and final position of the data set acquisition. In green shade is the surface area encompassed by the varying **B** vectors.

5.1.3 Spatially varying probe beam

To generate the vortex probe light and its polarisation structure, we have at our disposal q-plates of different q number that generate light with OAM $\ell = 1, 2, 4, 6, 10$. There is no fundamental difference in the mechanism of the absorption process by varying the OAM, and the main result summarized in this thesis and published in [9] were taken with $\ell = 2$, mainly because the correspondent q-plate generates the polarisation pattern with the least amount of ellipticity, which is a source of noise in the absorption process. Fig. 5.3 shows the polarisation pattern of the beam for that particular probe beam. Regarding the intensity of the probe, we had to operate in a range that was limited on the lower side by the background light, generating noise in the absorption images, and the upper constraint which was the bit depth of the camera causing image saturation for higher powers. This translated in a possible range of beam power from 0.03 μW to 0.5 μW. That said when we take account of the perturbative nature of the model outlined in Sec. 4.5, we find that the highest agreement with the prediction formula for the absorption of Eq. 4.42 is for the lower values of intensity. Hence the main results present in [9] and that will be shown later were taken with a total beam power of 0.13 μW. Due to the vortex structure of the beam it is required to consider the local intensity of the beam, rather than simply the total, when calculating the Rabi frequency. In fact, since the intensity is distributed on a ring, in the analysis of the data we concentrate on the areas of maximum intensity at a certain radius from the geometric center of the beam, i.e. between 100 and

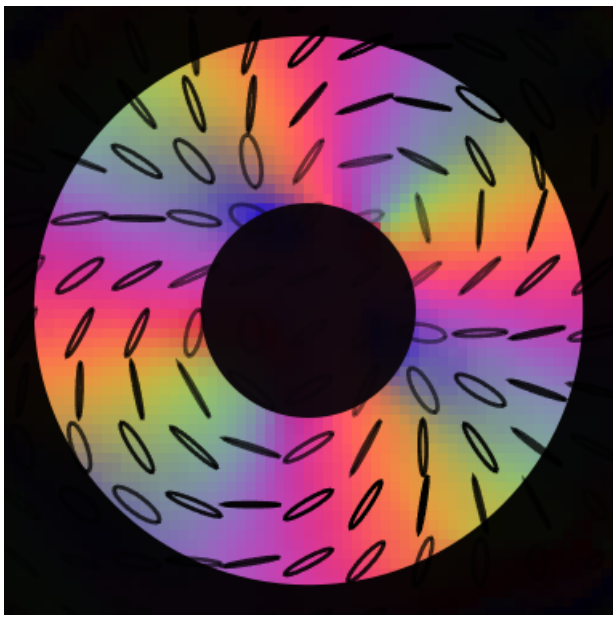

Figure 5.3: Polarisation pattern of the q-plate beam used in the experiments. The black ellipses represent the direction and ellipticity of the local polarisation, and the color map refers to the usual polarisation legend used throughout the thesis. It can be noted that the polarisation direction twists twice around the center, thus the OAM is $\ell = 2$.

160 μm from the center. For these areas the local intensity translate to a Rabi frequency of Ω_R=$2\pi \times 0.26$ MHz.

5.1.4 Absorption Imaging

The proper data acquisition is done via absorption imaging. After the probe has passed inside the cell and is absorbed by the atoms, it passes through a $2f$-imaging system with no magnification that projects the image plane of the atomic cloud onto a CCD camera, recording the transmitted probe light (I_{trans}). Subsequently, other two images are taken to generate the absorption image, one of the probe at a time after the atomic cloud has dispersed, thus providing an image of the original probe intensity profile (I_{probe}) and the last image captures the background light in the lab environment while all the experimental beams are turned off (I_{back}). I should report that the two images I_{probe} and I_{back} are obtained for every repetition of the interaction between probe and atoms, however they are pretty much identical for the entirety of the whole data set of a rotation or inclination experiment. Instead I_{trans} images can be different even between two repetition of the absorption for the same magnetic field as the number of atoms is the least stable parameter between the shots, relatively varying much more than the probe intensity and

polarisation or the background light. This is the main reason for the requirement to acquire multiple absorption for the same magnetic field, in order to average out the statistical noise generated by the eventual differences in the atomic population available.

These three images, and the intensity data they contain, are connected by the Beer-Lambert law:

$$(I_{\text{trans}} - I_{\text{back}}) = (I_{\text{probe}} - I_{\text{back}})e^{-\text{OD}},$$

hence we can obtain the OD of the cloud as

$$\text{OD} = \ln \frac{(I_{\text{probe}} - I_{\text{back}})}{(I_{\text{trans}} - I_{\text{back}})}. \tag{5.1}$$

The absorption images that make the data are just the Eq.5.1 applied to the images acquired in the experiment. Fig. 5.4 is an example of the images (a-c) obtained with this procedure and the absorption image generated (d).

To summarize, the product of the experimental procedure is a set of absorption images for the different magnetic field that was varied between them as outlined above and that are categorized by the variation as rotation and inclination data sets. A part of the absorption data sets can be seen in Fig. 5.5 and 5.6. In addition, some examples of absorption images with different OAM orders can be seen in Fig. 5.7.

One of the main concerns throughout my involvement in the investigation featured in this thesis has been to properly evaluate the experimental conditions underlying the data acquisition. In particular the already mentioned challenges with the background magnetic field in Sec. 3.2.3. This issue, together with the ellipticity noise in the probe polarisation are the main culprits that we identified as the cause for the disagreements between the experiment and the model when performing the data analysis.

The absorption patterns of Fig. 5.7 has some differences with the ones in Fig. 5.5 and 5.6. The reasons for this is the different ratio of the beam power employed (and the resulting Rabi frequency) and the resulting OD of the atomic cloud, which is higher. In addition the mentioned difficulties in the background magnetic field cancellation were more significant at the time of generation of the images in Fig. 5.7. Hence they are not going to be featured in the subsequent data analysis, as the resulting Fourier data obtained from them is characterized by high systematic error, especially the data with mostly longitudinal magnetic field.

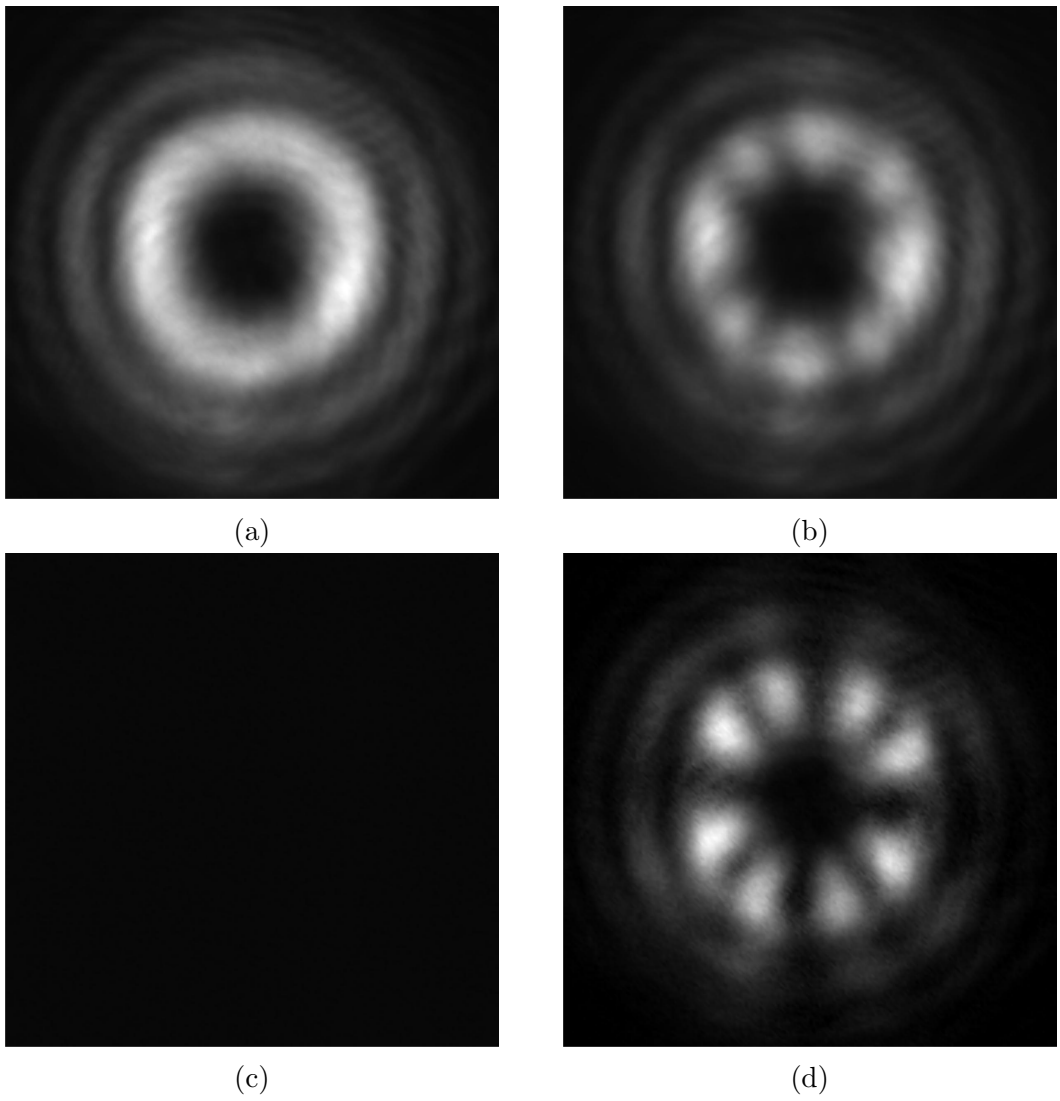

Figure 5.4: Example images (600×600 μm^2) of (a) the probe intensity, I_{probe}, (b) transmitted light, I_{trans}, (c) the background radiation I_{back} and (d) resulting absorption profile OD, generated by the other images using Eq. 5.1, with the black representing low and white representing high intensity (and OD). Let us remind here that the atom cloud after expansion is 400 μm, slightly larger than the probe beam which is $\sim 300\mu$m in diameter. Note that the convention for the OD is opposite in [9].

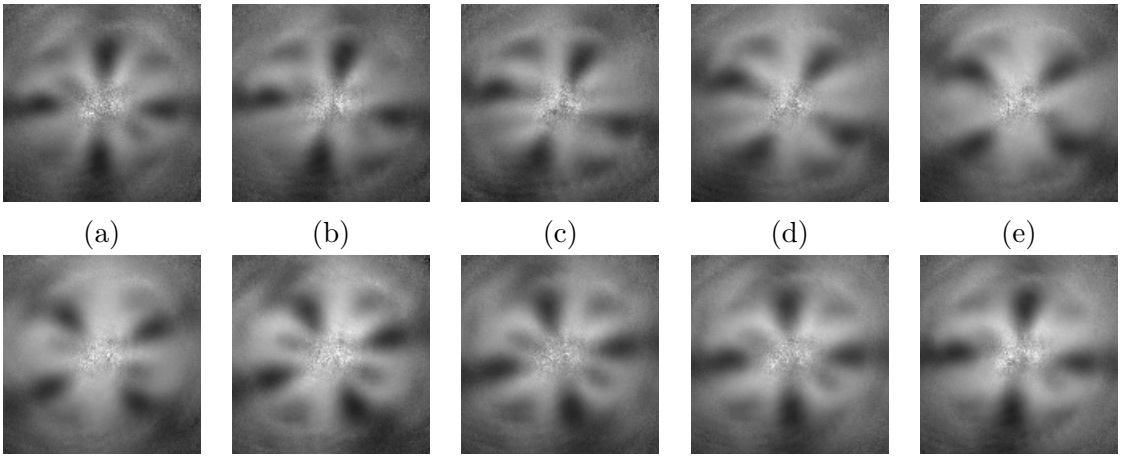

Figure 5.5: Part of an absorption image dataset for the orthogonal magnetic field rotation variation (as in Fig. 5.2a). The absorption images were taken with $\theta_B = 45°$ and starting at $\varphi_B = 0°$ in (a) and ending at $\varphi_B = 180°$ in (j), changing by 20° for the other images. It is noticeable the apparent "rotation" of the image as the magnetic azimuthal angle φ_B varies. The other experimental parameters are $|\mathbf{B}| = 0.5$ G. Atomic number $0.5 \cdot 10^7$ with a density of $0.5 \cdot 10^{11}$ atoms/cm^{-3} before an expansion of 3.5 ms. Image set is normalized to the same maximum value.

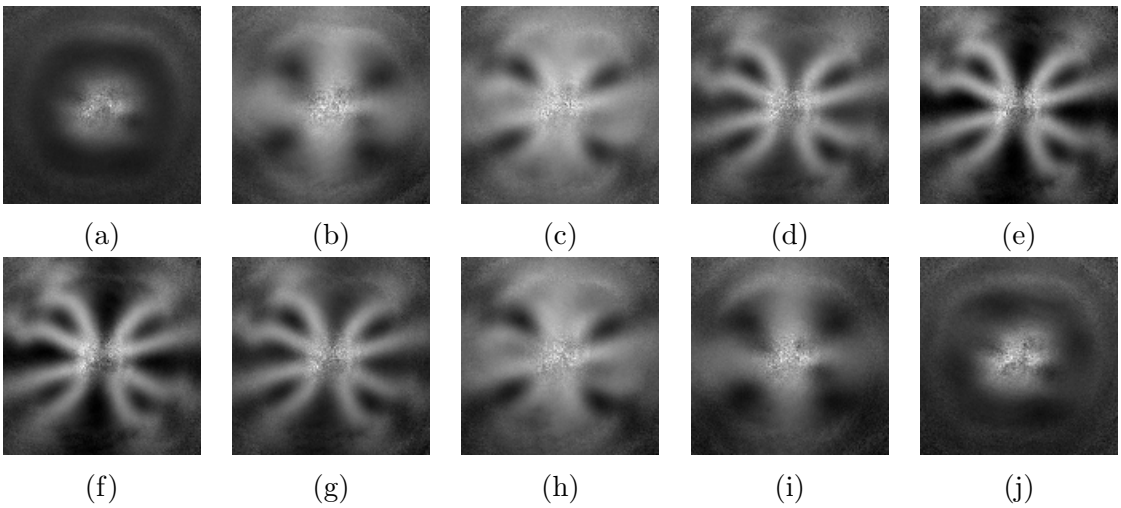

Figure 5.6: Part of an absorption image dataset for the magnetic field inclination variation (as in Fig. 5.2b). The absorption images were taken with $\varphi_B = 0°$ and $\theta_B = 0°$ (a), $\theta_B = 26°$ (b), $\theta_B = 51°$ (c), $\theta_B = 72°$ (d), $\theta_B = 87°$ (e), $\theta_B = 93°$ (f), $\theta_B = 108°$ (g), $\theta_B = 129°$ (h), $\theta_B = 154°$ (i) and $\theta_B = 180°$ (j). As it can be seen, the increase of θ_B causes a "splitting" in the pattern as the one previously estimated in the model shown in Fig. 4.4c. The other experimental parameters are $|\mathbf{B}| = 0.5$ G. Atomic number $0.5 \cdot 10^7$ with a density of $0.5 \cdot 10^{11}$ atoms/cm^{-3} before an expansion of 3.5 ms. Image set is normalized to the same maximum value.

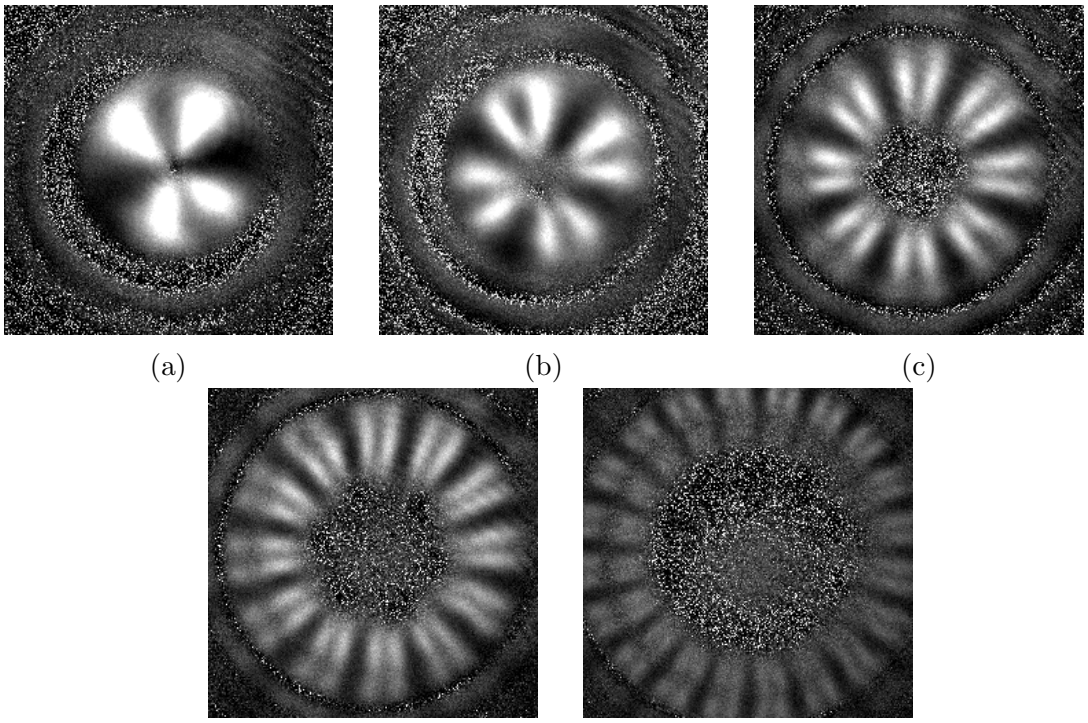

Figure 5.7: Absorption images of probe beams with different angular moment. The absorption images were taken with $\theta_B = 90°$. (a)-(e) $\ell = 1, 2, 4, 6, 10$. The other experimental parameters are $\mathbf{B} = 0.2$ G along $\hat{x}$, i.e. is completely orthogonal to the light propagation direction, and atomic density $1 \cdot 10^8$ with a density of $5 \cdot 10^{11}$ atoms cm^{-3} before an expansion of 2 ms.

In the first stages of development of the setup some experiments have been performed [135] as it was explored the effect of varying the degree of ellipticity of the probe, i.e. going from total σ_+ (or σ_-) to the various mixture in between, without focusing on the variation of the magnetic field. In both [9] as well as this thesis we only extend our investigation to polarisation with as close as possible to the equal ratio of σ_+ and σ_-, as shown in Fig. 3.13 and 5.3. Nevertheless it is noticeable how the manipulation of the probe polarisation structure can be obviously seen as an equivalent actor to the influence of the interaction with the atoms. Therefore, in future plans for the setup it will take a much bigger emphasis the arbitrary generation of the probe, with different mixture of OAM and polarisation from the ones featured in this thesis.

5.2 Data analysis

In the previous section I outlined the procedure from which we obtain a set of absorption images. Here I will now explain how we extrapolate the information on the measured magnetic field from the absorption data and that we then confront with the model. First of all, we need to manipulate the images to simplify the information contained from a $2D$ matrix format into a $1D$ array, which is easier to compare in a graph. In Fig. 5.8 the stages of the transformation just described is shown. In order to do that we first unwrap the image converting it from Cartesian to polar coordinates. This is necessary as the symmetry of the probe beam is cylindrical, which on the plane of the image becomes radial. We perform this operation automatically through software and with the same transformation matrix for the entire dataset: in the program we need to identify the center of the beam around which the polar transformation will be performed. We use the same image coordinates for all the absorption images of the same dataset. It is important to select the center carefully as even a small error will introduce visible distortion in the transformed image. After this first transformation it can be easily perceived how only a section (that in Fig. 5.8a corresponds to a horizontal slice) of the image carries useful information. Hence a variable number of the central rows is taken and added column by column to form the desired array of values, representing the profile of the probe absorption in Fig. 5.8b. The slices can also be used to provide a nice representation of the progressive changes caused by the variation of the magnetic field on the absorption of the probe. This

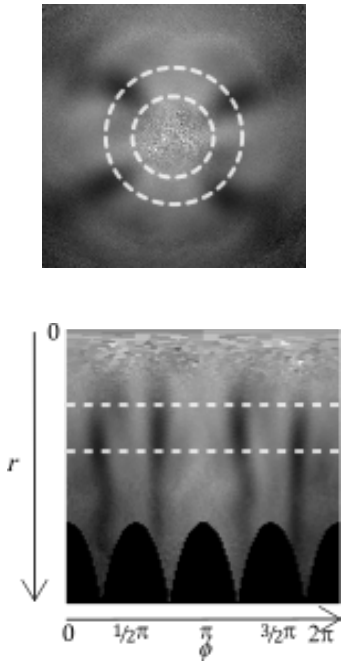

(a)

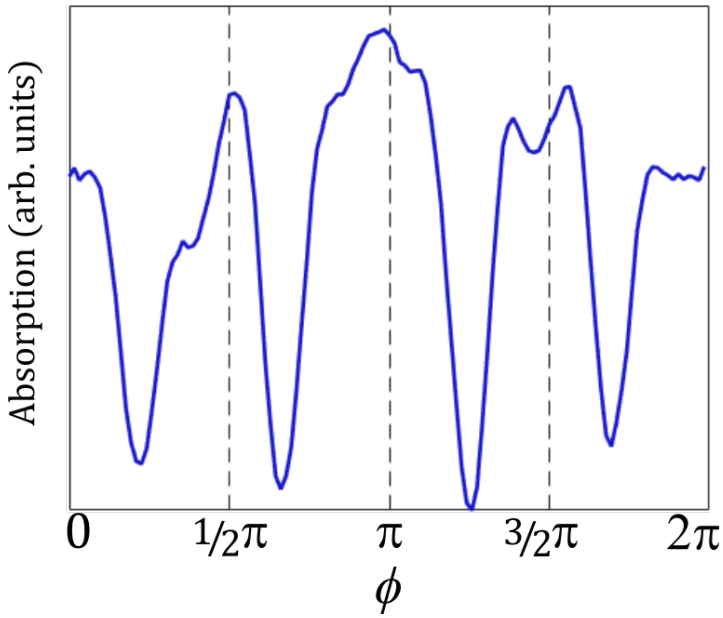

(b)

Figure 5.8: Stages of absorption data extrapolation. (a) Example of absorption image with the relevant area of the analysis shown between the two dashed lines (top) and the same absorption image transformed in polar coordinates and with the same relevant area between the lines (bottom). (b) Absorption profile of the area between the dashed lines, generated from the sum of the pixel values in the columns. The background has also been subtracted and the values are normalized.

.

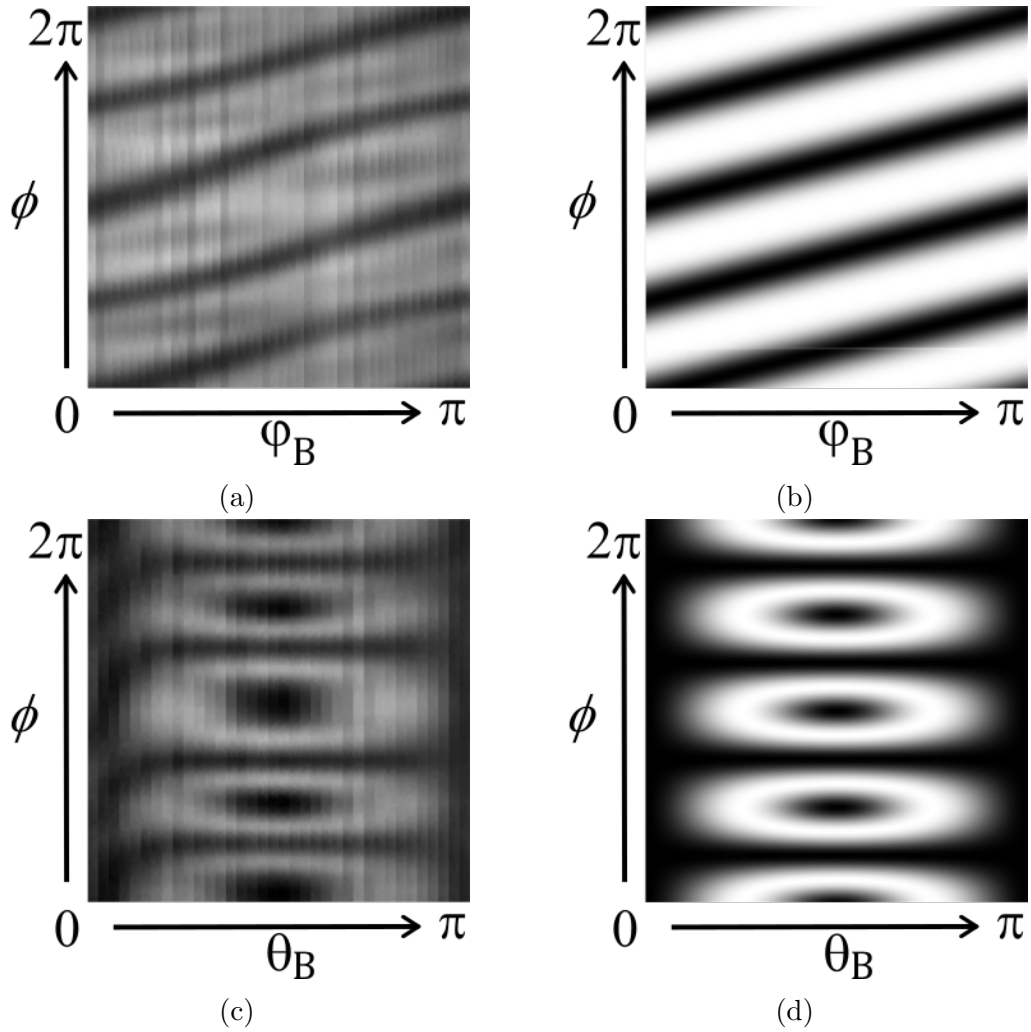

Figure 5.9: Compilations of the unwrapped OD images with varying magnetic field. (a) Azimuthal angle φ_B variation (in steps of 4°) and (b) theoretical equivalent calculated graph. (c) Polar angle θ_B variation (in steps of 5°) and (d) theoretical equivalent calculated graph.

can be done by combining and joining side by side the relevant section of the images in order, as shown in Fig. 5.9

At this point we need to introduce the tool that will allows us to quantify how well the model predicts the absorption profile of the probe for each different magnetic field alignment: the Fourier transform. In fact, it can be shown that the 2ℓ and 4ℓ components of the complex Fourier transform of Eq. 4.42 are directly dependent to the magnetic field angles φ_B and θ_B, respectively. In particular, the Fourier transform must be calculated along the probe phase angle ϕ,

$$\mathcal{F}(T_{|\Psi_1\rangle\to|e\rangle}(\phi)) = \frac{1}{2\pi}\int_0^{2\pi}(T_{|\Psi_1\rangle\to|e\rangle}(\phi))e^{i\Phi\phi}d\phi = F(\Phi) \tag{5.2}$$

. One of the relevant quantities is the argument of the 2ℓ component which is

$$\arg(F(\Phi = 2\ell)) = 2\varphi_B, \tag{5.3}$$

where the factor 2 comes from the symmetry of the specific polarisation pattern of the probe. The dependence on θ_B can be extrapolated from the value of 4ℓ component

$$|F(\Phi = 4\ell)| = \frac{1}{4}\sqrt{\frac{\pi}{2}}\sin^4\theta_B. \tag{5.4}$$

It is also possible to obtain a somewhat similar dependence from the value of the 2ℓ component,

$$|F(\Phi = 2\ell)| = \sqrt{\frac{\pi}{2}}\cos^2\theta_B\sin^2\theta_B, \tag{5.5}$$

which has half the periodicity of the 4ℓ dependence. What Eq. 5.3, 5.4 and 5.5 mean is that we can assign a value to the magnetic field azimuthal (φ_B) and polar angles (θ_B) by applying a simple Fourier transform on the data in Fig. 5.8b.

In detail, from Eq. 5.3 we can read the magnetic field azimuthal rotation, starting from the arbitrary 0 value[2] and tracking the variation of φ_B in between the rotation dataset. Instead from the numerical value obtained in Eq. 5.4 it is possible to extrapolate θ_B, after finding out the normalizing factor, equal to the maximum value of the dataset, that should come out of the absorption image with related to $\theta_B = \pi/2$. If there are multiple absorption images referring to the same magnetic field, an average and standard deviation can be also obtained for the Fourier values.

To recapitulate this section, we begin from an ensemble of absorption images obtained at variable magnetic field angles, either φ_B or θ_B, and we end up with a series of averaged Fourier values, either phase or amplitude respectively.

5.3 Results discussion

Finally in this last section about the atomic magnetometry experiment at Glasgow, we can show the main result of the analysis: the comparison of the data with the Fermi's Golden Rule model, as well as the Optical-Bloch (OB) equation one. These comparisons

[2]The arbitrariness arises from the fact that we are delaying with the phase of $F(\Phi = 2\ell)$, thus we can obtain a relative difference of φ_B between absorption image.

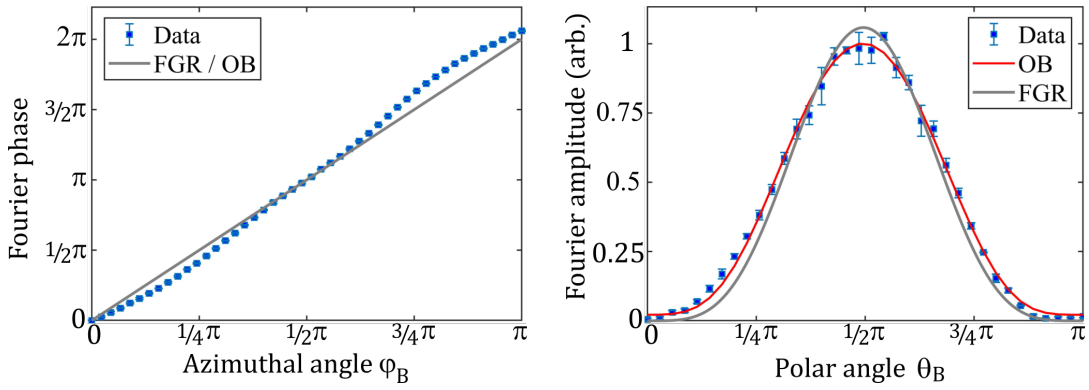

Figure 5.10: Dependence of the 2ℓ Fourier phase (a) and 4ℓ Fourier amplitude (b) vs the magnetic field angles φ_B and θ_B respectively (blue squares). It is also shown in comparison the same dependence for the FGR and OB models (solid lines). Error bars of the data points represent the standard deviation of 3 repetitions for the phase and 5 for the amplitude.

are shown in Fig. 5.10.

Overall the models are in sufficient agreement with the data. It should be noted that due to experimental arrangement, it was necessary to balance the need for a sufficient probe power to obtain an high contrast and the condition of weak-coupling, hence low probe power, for the validity of the perturbative FGR model. We are slightly over the limits for the quantitative validity of the model in Eq. 4.42 and at least for the graph in Fig. 5.10b the model can provide a concise understanding but cannot be used as a proper quantitative simulating tool. Hence it is necessary to carry out a proper numerical simulation through the OB equations which was fitted to the beam intensity and normalized so that the maximum value obtained in the simulation is the same to the maximum Fourier value extrapolated from the data, which is unsurprisingly in optimal agreement with the data.

The underlying deviation is of different nature in the case of 5.10a. We noticed that the polarisation profile noise with small local degrees of ellipticity can induce an acceleration (or deceleration) of the apparent rotation with the implicit imbalance between $\sigma_\pm$ light components. Another source of discrepancy could be the generation of the magnetic field. Any uncertainty in the magnetic field direction will likely show as a deviation from the ideal linear progression desired. This kind of systematic error will be cumulative in the phase values. On the positive note, random error is much more modest, warranting a satisfying amount of reproducibility to the experimental protocol.

To translate this in terms of the **B** alignment, obtaining the values from the inversion of

Eq. 5.3 and 5.4, we get an error of 1.7° for both the calculated angles φ_B and θ_B. It should be noted that the main goal of our investigation was to demonstrate the fundamental concept of a optical atomic magnetometer in $3D$ able to detect the alignment of the magnetic field with single-axis optical probing, with the information on the alignment being independent on the magnitude of the magnetic field. This property is one of the differences between our setup and the one described in 5.4. Thus to the reader with more familiarity and knowledge in the field of optical magnetometry the sensitivity might seem a little bit lackluster, at least compared to the values that can be reached in other setups [10,136,137] and in particular with *Spin-exchange relaxation-free* (SERF) magnetometers [11]. In the last setup in particular the high sensitivity is obtained by minimizing the rates of relaxation of the atomic spin states. The same mechanism applies to our concept: the spin alignment and main driver of the coherence between the states in our experiment is the Larmor frequency, and the mechanism that destroys them is the collision between the atoms. For the parameters that we reported previously, in the ideal case we should be able to detect B-fields down to 50 pT or $5 \cdot 10^{-4}$ mG.

In the future iterations of the experiment the focus of the investigation will shift from the analysis of the model and its validation, to the expansion of the set of polarisation states that can be used for the probe beam, with the end goal of allowing for full flexibility and generation of arbitrary structured light beams. This upgrade will not require much effort in theoretical terms, the model regulating the interaction will only need to include the change in the polarisation structure of the beam. On the other hand to reach the wanted full flexibility a setup similar to the one described in Sec. 2.4 will need to be included in the optical path of the probe beam.

Regardless as it can be seen from Fig. 5.13, some changes in the probe polarisation can be introduced even by simply adding some waveplates before or after the q-plate in the current setup. In Fig. 5.11 and 5.12 are shown some preliminary results of these experiments. The most promising development that seems to arise from the use of more varied polarisation profiles is the ability to get rid of the main symmetry present in the Fourier values. Unfortunately their dependence from the magnetic angles has a period of π, i.e. $F(\Phi)$ has the same value at φ_B and $\varphi_B + \pi$, and it would be a significant upgrade to use a polarisation profile that produces two different absorption image for these angles and break the symmetry.

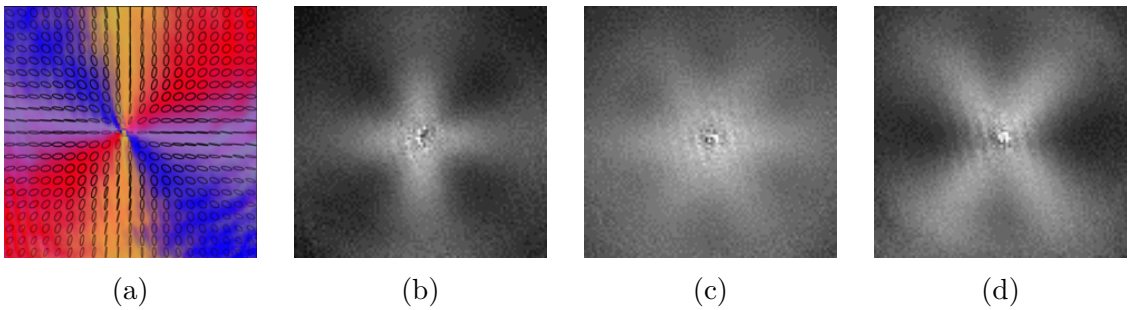

(a) (b) (c) (d)

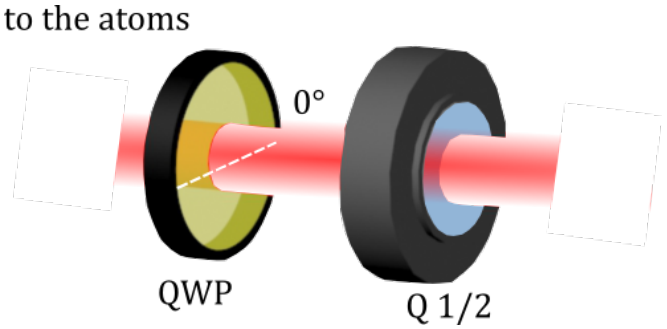

(e)

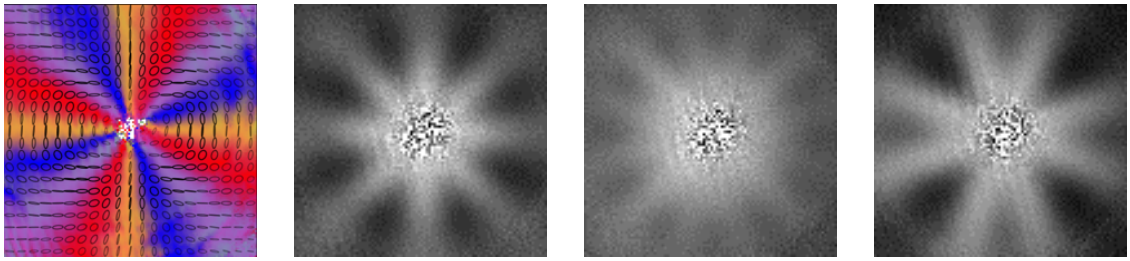

(f) (g) (h) (i)

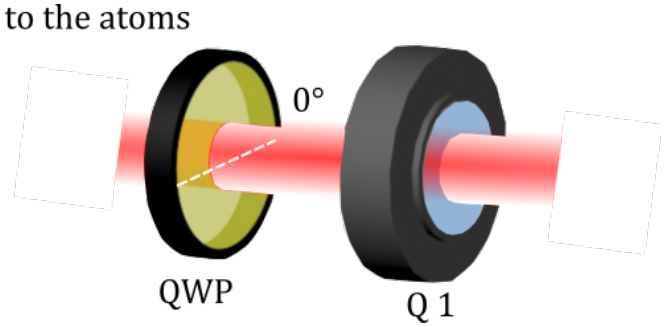

(j)

Figure 5.11: Absorption images for various alternative polarisation profile realized with q-plates and waveplates. (a) polarisation profile of probe beam generated with $\ell = 1$ and QWP. (b-d) Absorption images at $\theta_B = 0°$, $\theta_B = 45°$ and $\theta_B = 90°$ respectively. (e) To generate the polarisation, the linear light passes through the Q-plate ($q = 1/2$) and then a $\lambda/4$ waveplate oriented with horizontal optical axis. (f) polarisation profile of probe beam generated with $\ell = 2$ and QWP. (g-i) Absorption images at $\theta_B = 0°$, $\theta_B = 45°$ and $\theta_B = 90°$ respectively. (j) To generate the polarisation, the linear light passes through the Q-plate ($q = 1$) and then a $\lambda/4$ waveplate oriented with horizontal optical axis. Note how there are different symmetries, i.e. Fourier modes, for these polarisation profiles than the one present in the linear case shown in the main result.

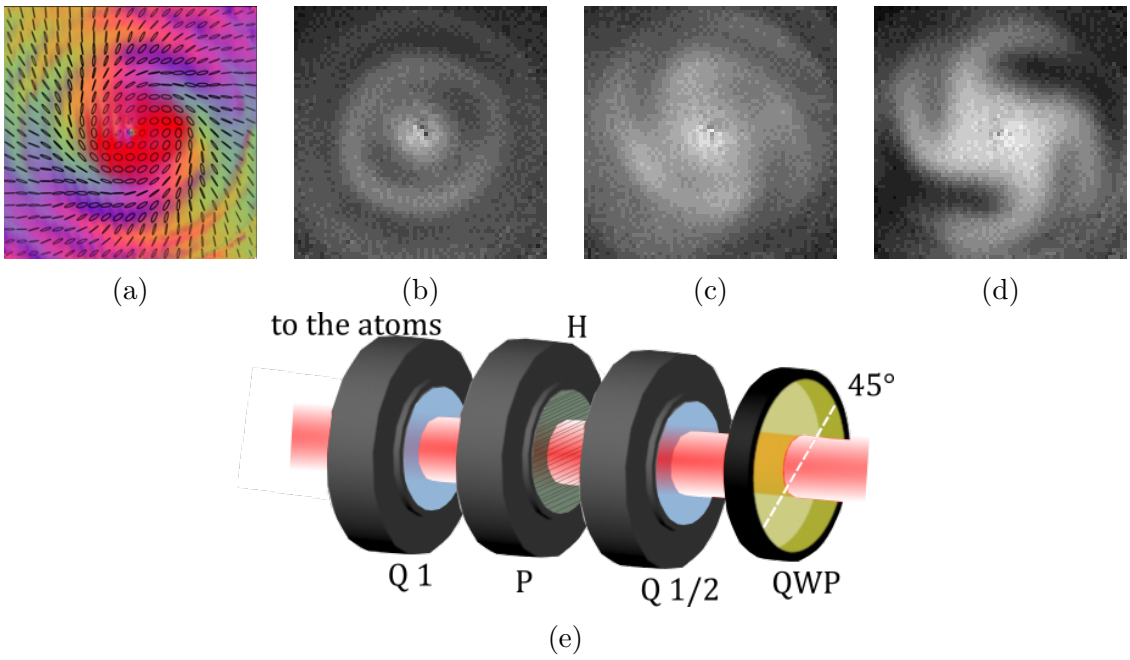

Figure 5.12: Absorption images for a Poincaré beam generated by the linear superposition of a σ_+ vortex beam with $\ell = -1$ and a σ_- vortex beam with $\ell = -3$. (a-d) Absorption images at $\theta_B = 0°$, $\theta_B = 45°$ and $\theta_B = 90°$ respectively. (e) To generate the polarisation, the linear light passes first through a $\lambda/4$ waveplate oriented at 45°, then through the first Q-plate ($q = 1/2$). Afterwards all polarisation different from the horizontal are filter out and the final transformation is done by the last Q-plate ($q = 1$).

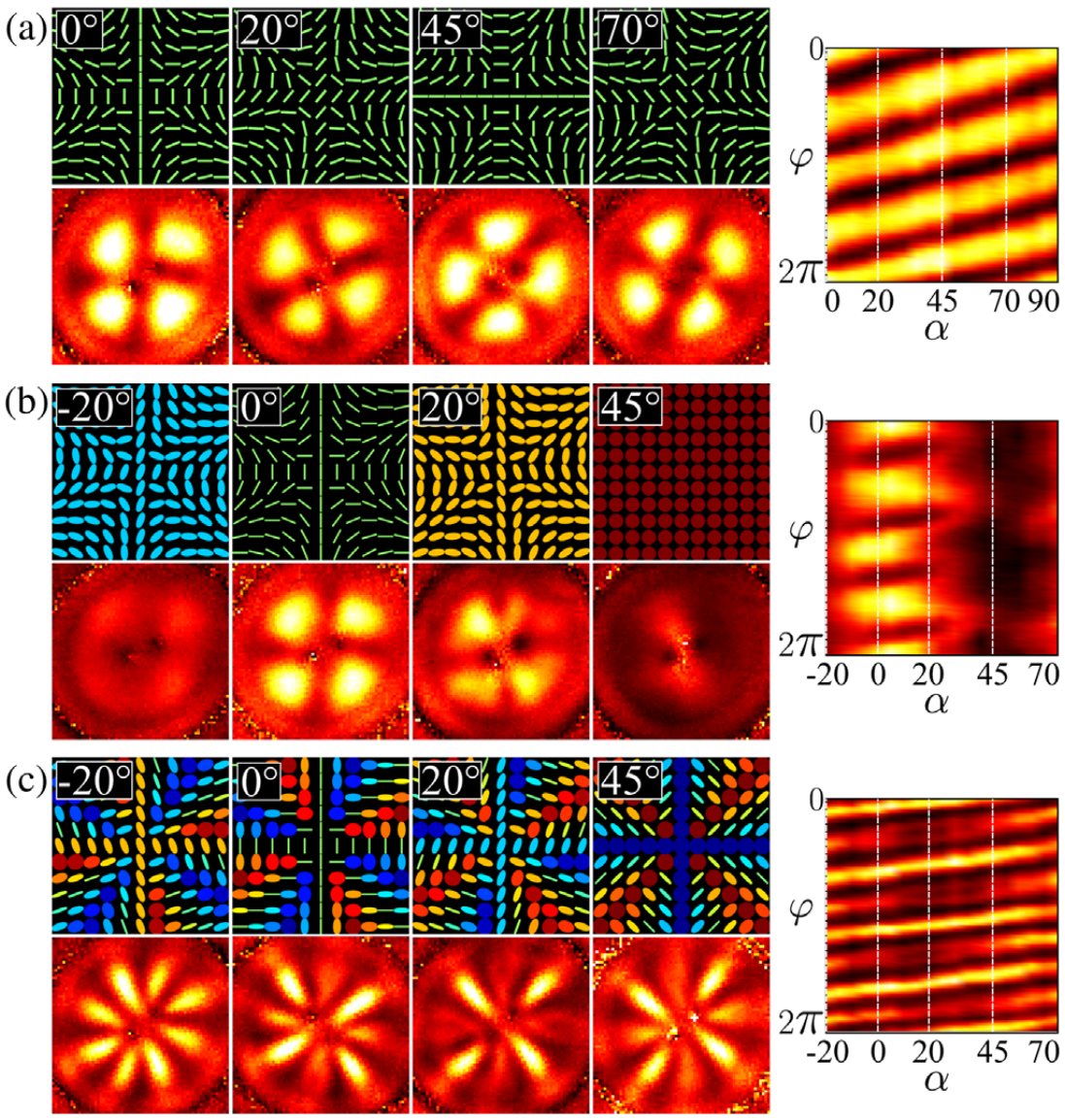

Figure 5.13: Absorption profiles as a function of input polarisation of a beam with $\ell = 2$. In (a) the focus is on the global rotation of the local polarisation direction obtained via a half waveplate placed before the q-plate at an angle α. polarisation profiles (top row). Absorption profiles (high absorption yellow) (lower row). Radially unwrapped absorption profiles, one image every 5° in α (side). In (b) the probe ellipticity is varied by inserting a quarter waveplate. Here, the parameter angle α goes from $-45°$, i.e. left circularly polarized beam) to 45°, i.e. right circularly polarized beam, with $\alpha = 0$ representing the linear vortex beam. polarisation profiles (top row). Absorption profiles (lower row). Radially unwrapped absorption profiles, one image every 5° in α (side). In (c) a superposition of linear and elliptically polarized beam by placing the quarter waveplate after the q plate. Absorption profiles (lower row). Radially unwrapped absorption profiles, one image every 5° in α (side). Image taken from [135]

Another desired development, which is still in the planning stages, is to replicate the magnetometry setup with a glass cell at room temperature as there is no explicit dependence on temperature in the interaction between light and atoms. It should be clear by now that the main benefit deriving from the use of cold atoms in the experiment is the control on the starting atomic population in the desired state $5S_{1/2}, F = 1$. However even at room temperature the same level is populated by a fraction (about 3/8) of the atoms by the Boltzmann factor. The main advantage of shifting to room temperature would clearly simplify the setup, as the vast majority of the equipment used in the setup is in order to generate an atomic cloud at low temperature and in vacuum conditions. Also since the starting conditions of the atomic population do not need to be modified, the repetition rate of the absorption experiment would be much faster[3] On the other hand, the output information obtained by absorption imaging will be more noisy, as more rates and phenomena will intervene in the whole process, e.g. collision of atoms between themselves and with the glass cell wall, residual Doppler broadening of the lines, blurring due to the atom side velocity[4], and will require a change in the simple absorption setup employed in the cold atoms experiment.

In conclusion, in this chapter I have presented the main results obtained during my PhD regarding the principal investigation of the atomic magnetometry with structured light. These results show the spatial synergy between the magnetic field alignment and the structured light when interacting with an atomic cloud. This spatial information in the form of an absorption image can be used as the "display" of a three-dimensional compass, which is by design not dependent on a time dependent signal. These results are largely independent also on the field strength. The same results were summarized in a recently published PRL article [9].

5.4 Magnetometry with hot atoms

The main effort of my PhD work has revolved around the investigation of the interaction of vectorial light with atomic clouds that are trapped and cooled so to more easily control the

[3]At the moment, the 98% of the effective duration of the experiment is dedicated to the growth of the trapped atomic cloud in the MOT, i.e. its the limiting factor of the repetition rate.

[4]Some of these effects were also taken into consideration in a similar study done by our group some years ago [138]

initial state population of the atoms. As it was already mentioned, this kind of approach is not strictly necessary and there are many experiments, e.g. [139–142], in this field of research that instead choose to use atoms enclosed in glass cells at room temperature.

The main advantage that this choice involves is to sensibly simplify the experimental setup by discarding all the equipment necessary for a MOT[5]. In some of those experiments it is still modified the temperature of the atoms, heating up the cell up to $60°C$, to increase the density of ^{87}Rb, since the rubidium stuck on the glass cell will be released by the heating up of the glass wall.

The obvious downside is that the atoms are in a given state that cannot be modified and the study of the dynamics of the system is much more complex and there is an higher dependence on the external properties of the atoms and their system, such as velocity, pressure, dimension of the cell. The underlying physical processes still determine the interaction, and in particular the theory based on the FGR model shown in Sec. 4.5 applies, not relying on the fact that the atoms must be in a particular condition of density or temperature.

In this section I want to address the work [23] carried out at Xi'an Jiatong University by our collaborators, as I was not involved directly involved in the proper realization of the system in Xi'an laboratory and have participated as a collaborator in the interpretation of the data and the qualitative realization of the model. They have in essence investigated the same interaction between vector vortex beams and atomic ensemble but at room temperature. A difference is the choice for the atomic transition that is excited by the light, which is $5S_{1/2}, F = 2 \rightarrow 5P_{1/2}, F' = 1$[6]. This might not seems as a big difference but it has some non trivial effect as although the system used in Glasgow has less substates, still gives rise to two different kind of dark states which appear when the magnetic field is orthogonal to the probe propagation axis. The detailed explanation of why this occurs will follow the presentation of the data obtained in China by our collaborators. For now, as an hint to the reader, let us keep notice of the polarisation of the light and the optical pumping that it can induce in the different atomic manifolds involved in the experiments.

The setup that is used in the experiment can be seen in Fig. 5.14 and it is clear at

[5]In our experiment the vast majority of electronics, optomechanical equipment and lasers is necessary to prepare the atoms with the desired parameter of state population, temperature and density. The actual experiment relies only on one beam path, the rectangular coils and a camera, plus the electronics to synchronize them which is anyway necessary in the above mentioned "pre-experiment" part.

[6]In our experiment is $5S_{1/2}, F = 1 \rightarrow 5P_{3/2}, F' = 0$

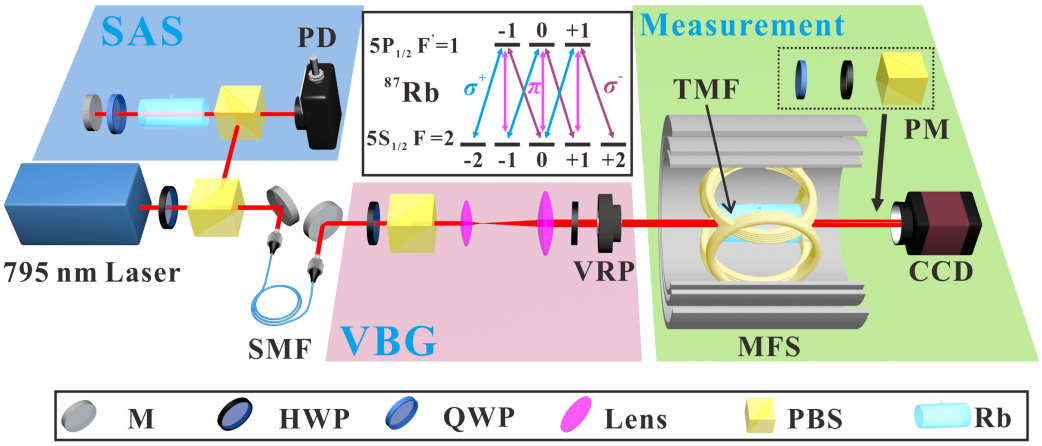

Figure 5.14: Experimental setup and atomic energy levels. M: mirror; HWP: half-wave plate; QWP: quarter-wave plate; L: lens; PBS: polarisation beam splitter; PD: photodetector; SMF: single mode fiber; VRP: vortex retarder plate; CCD: charge-coupled device camera; MFS: Magnetic field shielding; PM: Projection measurement. SAS: Saturated absorption spectroscopy; VBG: Vector beam generation. Image taken from [23]

first glance the simplicity in respect to Fig. 3.14. The light profile is a standard vector vortex beams that can be expressed as:

$$\mathbf{E}(r,\phi,z) = E_0(r,\phi,z)\begin{pmatrix}\cos(m\phi)\\ \sin(m\phi)\\ 0\end{pmatrix} \tag{5.6}$$

where the radial profile is the typical ring shape intensity and m is the optical angular charge. In other words the polarisation of the beam is linear at every point but in a direction that varies with a period of $2\pi/m$, analogous to what is also used in our experiment and shown in Fig. 3.13.

The first phenomenon to investigate is the dependence of the transmission in respect to the variation of the magnitude of the magnetic field in the longitudinal (Fig.5.15) and transverse (Fig.5.16) direction. As it can be seen the two situation present different effects. In the longitudinal case the absorption is completely uniform and independent of the polarisation structure. When the field is small the EIT phenomenon is prevalent and the beam is transparent to the atoms. Then the increase of the longitudinal component induces a Zeeman shift in the energy levels that breaks any coherence or EIT effect in the system, allowing the absorption of the beam by the atoms. It is important to note that

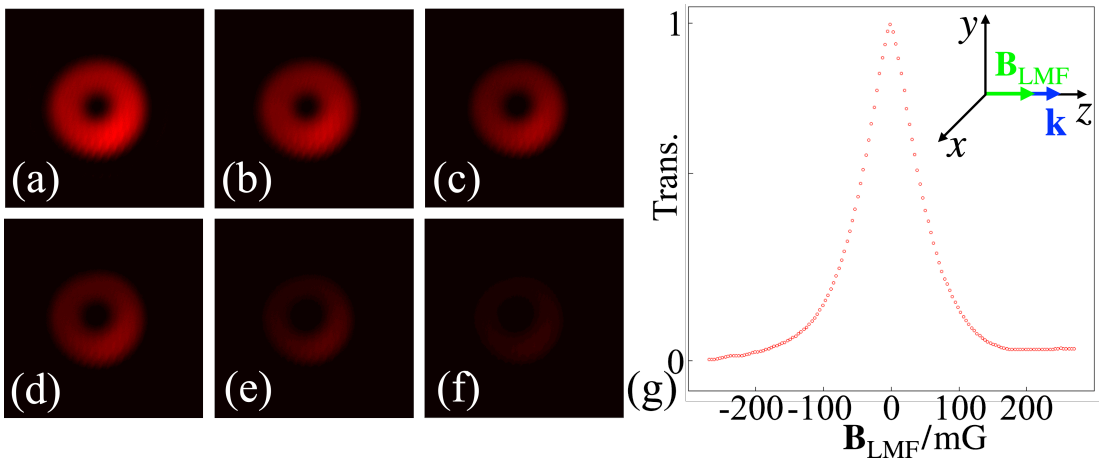

Figure 5.15: The experimental results of the radially polarized beam in presence of LMF. (a) - (f): the intensity distributions after passing through the atom vapor under varied LMF: $\mathbf{B}_{\mathrm{LMF}} = 0$ mG, 50 mG, 100 mG, 120 mG, 160 mG and 200 mG, respectively. (g) The dependence of transmitted intensity for whole beam against the $\mathbf{B}_{\mathrm{LMF}}$. Image taken from [23]

this applies to any linear polarisation with the same effect.

On the contrary the polarisation plays a very important role when the magnetic field is transverse to the propagation direction. In particular there will be parts of the beam where the polarisation is orthogonal to the magnetic field, and others where it will be parallel. In the former case there will be the same effect as the longitudinal field, when increasing the magnitude, while the latter will retain the transparency independently of the magnetic field. The resulting pattern is a petal like structure with $2m$ fold symmetry.

As expected, this effect is retained even when rotating the magnetic field in the orthogonal plane, as a parallel to the experiment shown in Fig. 5.5. As it can be seen in 5.17 the transparency profile that arise with $B_{\perp}$ will rotate so that all the point where the polarisation is parallel to the magnetic field will retain the intensity.

By fixing the intensity of the magnetic field and varying the polar angle of $\mathbf{B}$, the transition between the two regime (full absorption and petal pattern) can be observed, as in Fig. 5.18. The main difference with the experiment in Glasgow is quite evident at this stage, since there is no observation of an additional splitting as in Fig. 5.6. As mentioned briefly earlier this has to do with the different level involved in the transition.

By quantizing the atomic sub-state along the direction of the magnetic field, one can explicitly show the difference between the two experiment. A visual scheme of the states and the light in the mentioned cases is shown in Fig. 5.19.

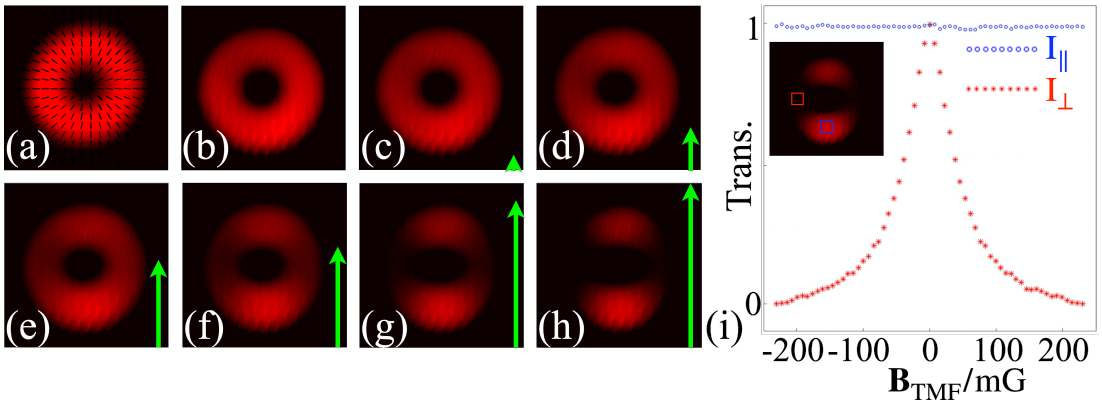

Figure 5.16: The experimental results of the radially polarized beam in presence of TMF. (a) Intensity and polarisation distributions without atoms. (b) - (h) Intensity distributions after passing through atoms under vertical TMF of varying strength: $\mathbf{B}_{\mathrm{TMF}} = 0$ mG, 23 mG, 61 mG, 123 mG, 146 mG, 206 mG and 230 mG, respectively. (i) The dependence of transmitted intensity for two selected regions against $\mathbf{B}_{\mathrm{TMF}}$. Image taken from [23]

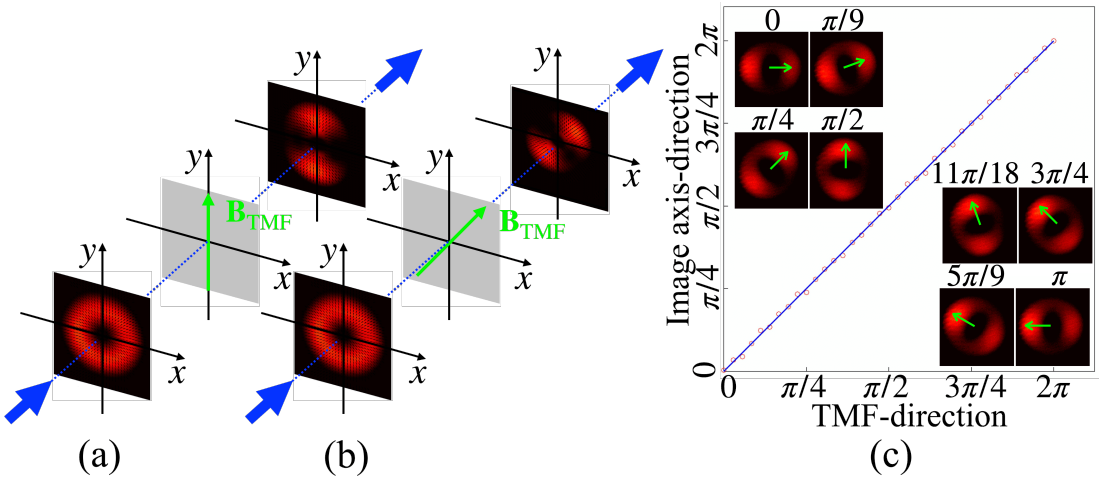

Figure 5.17: Transmission profiles as function of TMFs alignment. (a) and (b): intensity and polarisation distributions for vertical and diagonal TMF alignment. (c) Image axis of the transmission profile as a function of TMF direction. Insets: examples of observed transmission profiles. Image taken from [23]

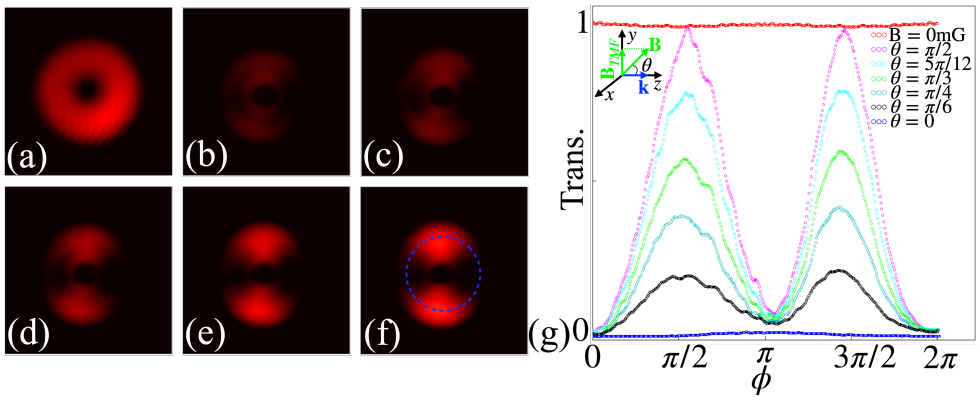

Figure 5.18: The experimental results of the radially polarized beam in presence of the spatial magnetic field with fixed intensity ($|\mathbf{B}| = 230mG$). (a): $|\mathbf{B}| = 0mG$. (b) - (f): transmitted patterns with $\theta = \pi/6, \pi/4, \pi/3, 5\pi/12, \pi/2$, respectively. (g) Polar plots for patterns at different angle θ at the radius indicated in (f). Image taken from [23]

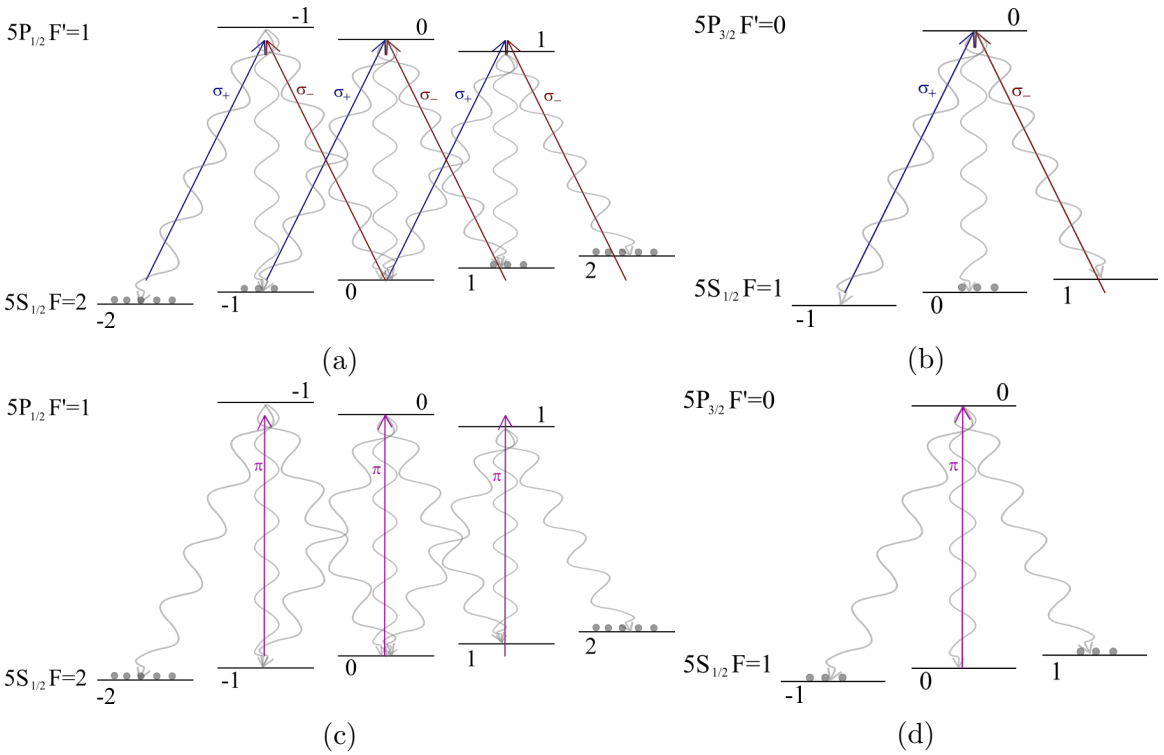

Figure 5.19: Scheme of the transition between energy level for the different light polarisation in the Xi'an (a,c) and Glasgow (b,d) experiments. (a) Transition scheme of the Xi'an experiment when only $\sigma_\pm$ polarized light is present. No dark state and continuous absorption. (b) Transition scheme of the Glasgow experiment when only $\sigma_\pm$ polarized light is present. The dark state is $5S_{1/2}, F = 1 m_F = 0$ and the atom become transparent. (c) Transition scheme of the Xi'an experiment when only π polarized light is present. The dark state is $5S_{1/2}, F = 2 m_F = \pm 2$ and the atom become transparent. (d) Transition scheme of the Glasgow experiment when only π polarized light is present. The dark state is $5S_{1/2}, F = 1 m_F = \pm 1$ and the atoms become transparent.

Let's consider the case of [23] first. When the electric field is orthogonal to the magnetic field (**B** all along $\hat{z}$), then each of the Zeeman substates is connected to at least one excited state by the light field, which is $\sigma_{\pm}$ polarized. This leads to the two possibilities outlined above. If the magnetic field is small or absent the destructive interference between different transitions dominates and the EIT phenomenon prevails. By adding a Zeeman shift induced by the magnetic field the destructive interference loses strength and light starts being absorbed by the atoms that continuously undergo transition between the states, both induced by the light or by spontaneous emission from the excited state[7]. In the case of **B** orthogonal to $\hat{z}$ there will be some place of the beam where the electric field is parallel to the magnetic field. In this case the resulting polarisation[8] is all π. A dark state is formed in the ground state population on the extreme Zeeman substates $m_F = \pm 2$, since the substates are not connected by the light to any of the excited state. Hence the light, after an initial transient of time, will not be absorbed anymore[9].

To conclude, in this section I have presented an alternative approach to the same inquiry that underlined my whole PhD. Regarding the experiment me and my group mainly helped in the understanding and interpretation of the data obtained by the group in Shaanxi, due to our expertise in the subject and previous work.

In particular the analysis of the dark state present in the system has been crucial in the development of a coherent narrative for the publication of [23]. Both this work and the previous data mentioned in the thesis, confirm the suitability of atomic vapor[10] to visualize the orientation of magnetic fields in $3D$ space although using only a single axis excitation scheme.

[7]Spontaneous emission from the excited state is isotropic and acts as a sort of "re-equalizer" of the population of the ground substates

[8]Remember that the quantization axis is along **B** and not $\hat{z}$. So the polarisation is different although the electric field is the same

[9]The accumulation of the population in the "side" states is done through spontaneous emission. And since there is no equivalent "spontaneous absorption" it will remain in this dark state

[10]Cold or hot.

Chapter 6

Conclusion

In the few final words of this thesis I want to summarize the content of my Ph.D. studies and give an outlook on the future prospect regarding the experiments that are described in the thesis.

During my three years of study, I mainly concentrated my effort on the experimental work by taking part in different experiments that were centered around the various application of structured light either in a pure optics context or in interaction with atoms. In the main atomic magnetometry experiment, me together with my group, have demonstrated the spatial relationship that incurs between magnetic field alignment and structured light interacting with atoms. The previously developed model of this interaction was finally confirmed through the analysis of the experimental data, hence an atomic compass for $3D$ magnetic alignment could be realized with the setup. In these years, my group and I have managed to achieve the deep level of understanding and mastery of the system that allowed us to publish a scientific paper summarizing the same work which is featured in this thesis. I want to mention with pride the resolve and thoroughness of my group which have not given up to the temptation of publishing earlier with somehow worse data, which have rewarded us in the end.

Our new approach to atomic magnetometry builds up in the field of EIT based magnetometers. We have shown a spatial relationship between the magnetic field alignment and the phase-shaped light as their interaction was mediated in an atomic cloud. This relationship can be employed to obtain the magnetic field alignment, realizing an atomic compass without explicitly invoking time-dependent effects. The 3D-alignment is derived from individual absorption images obtained in single-axis optical probing, where a spatially

structured vector vortex beam is responsible for both the generation and measurement of the atomic polarization. These results hold in the steady-state limit and can be largely independent of applied field strength, which can be of use for some application linked to magnetic sensing. There are two main roads concerning the future of this setup. For one of these road we planned to translate the acquired know-how of the model to a setup at room temperature. The other upgrade will be the insertion of a DMD setup to expand on the set of polarisation states that can be used for the probe beam as this will employ at his best our deep knowledge in the field of structured light as well allowing for more customization and asymmetry in the spatial profile of the interaction.

As I think back at my time in the lab, not only while working on the main experiments, but also when dealing with other projects, I feel a little odd noticing how the vast amount, at least in term of time involved, of the main activities of an experimental Ph.D., e.g. building up a optics setup, constantly realigning and readjusting all the optical elements, managing and maintaining all electronic equipment, writing the programming code for the PC controls, make a small apparition in the thesis. Thus I want to mention them here to give credit to those less "celebrated" labors.

The other important aspect which I want to mention here is the role that had the ColOpt ITN in the general development of my studentship. I feel particularly privileged to have had the opportunity to engage regularly not only with the group in which I was based on, which is a fundamental yet "normal" experience for many Ph.D. students, but also with many other Ph.D. and research groups in other universities in UK and the EU. I feel that all the additional training, which was of both theoretical and technical nature in the field of optics, collective effects, atom optics, statistical physics and many others, have widened as well as deepened my knowledge on many aspect of physics avoiding the unfortunate phenomenon of "narrow vision" in their particular small corner of research that sometime can affect Ph.D. students. An even more important contribution to my studies has been the opportunity given me with the the international secondments at the University of Münster and at Holoeye Photonics in Berlin. In the former, I have learned by working in close contact with another research group that was as well versed to the manipulation of structure light as my own in Glasgow, although being more focused on the interaction of light fields with nanoparticles instead of atoms. In the latter I was immersed in a very different environment from an academic research group. In there I have been

given responsibility on the development of a automated setup to ease the measure of the SLM display flatness, which is one of the product that the company sells. All these opportunities have definitely added quality and substance to the standard content of an experimental Ph.D. and I feel to have taken part to an enriched and enhanced experience.

In the end I hope that in this pages the reader would find the knowledge and experiences that I have acquired and performed in my research, and that they have been reported clear enough to be transferred to who are going to undertake their studies on the many possible aspects of vectorial optics, atom optics and physics research in general.

Bibliography

[1] The bakerian lecture. experiments and calculations relative to physical optics. *Philosophical Transactions of the Royal Society of London*, 94:1–16, December 1804.

[2] Isaac Newton. *Opticks, or, a treatise of the reflections, refractions, inflections & colours of light*. Courier Corporation, 1952.

[3] All of the early observation in the field of astronomy relied on the light coming from the celestial objects in the sky.

[4] Holger G. Krapp. Polarization vision: How insects find their way by watching the sky. *Current Biology*, 17(14):R557–R560, July 2007.

[5] Nadav Shashar, Roland Hagan, Jean G Boal, and Roger T Hanlon. Cuttlefish use polarization sensitivity in predation on silvery fish. *Vision research*, 40(1):71–75, 2000.

[6] Ricardo Gutiérrez, Cristiano Simonelli, Matteo Archimi, Francesco Castellucci, Ennio Arimondo, Donatella Ciampini, Matteo Marcuzzi, Igor Lesanovsky, and Oliver Morsch. Experimental signatures of an absorbing-state phase transition in an open driven many-body quantum system. *Physical Review A*, 96(4):041602, 2017.

[7] J. Wang, F. Castellucci, and S. Franke-Arnold. Vectorial light–matter interaction: Exploring spatially structured complex light fields. *AVS Quantum Science*, 2(3):031702, 2020.

[8] H. Rubinsztein-Dunlop, A. Forbes, M. V. Berry, M. R. Dennis, D. L. Andrews, M. Mansuripur, C. Denz, C. Alpmann, P. Banzer, T. Bauer, et al. Roadmap on structured light. *Journal of Optics*, 19(1):013001, 2016.

[9] F. Castellucci, T. Clark, A. Selyem, J. Wang, and S. Franke-Arnold. An atomic compass – detecting 3d magnetic field alignment with vector vortex light. *Phys. Rev. Lett.*, 127:233202, Dec 2021.

[10] D. Budker, D. F. Kimball, S. M. Rochester, V. V. Yashchuk, and M. Zolotorev. Sensitive magnetometry based on nonlinear magneto-optical rotation. *Phys. Rev. A*, 62:043403, Sep 2000.

[11] I. K. Kominis, T. W. Kornack, J. C. Allred, and M. V. Romalis. A subfemtotesla multichannel atomic magnetometer. 422(6932):596–599, Apr 2003.

[12] Dmitry Budker and Michael Romalis. Optical magnetometry. *Nature physics*, 3(4):227–234, 2007.

[13] Raghwinder Singh Grewal, Gour Pati, and Renu Tripathi. Light-ellipticity and polarization-angle dependence of magnetic resonances in rubidium vapor using amplitude-modulated light: Theoretical and experimental investigations. *Physical Review A*, 102(3):033102, 2020.

[14] C Affolderbach, M Stähler, S Knappe, and R Wynands. An all-optical, high-sensitivity magnetic gradiometer. *Applied Physics B*, 75(6):605–612, 2002.

[15] L Lenci, A Auyuanet, S Barreiro, P Valente, A Lezama, and H Failache. Vectorial atomic magnetometer based on coherent transients of laser absorption in rb vapor. *Physical Review A*, 89(4):043836, 2014.

[16] Stuart J. Ingleby, Carolyn O'Dwyer, Paul F. Griffin, Aidan S. Arnold, and Erling Riis. Vector magnetometry exploiting phase-geometry effects in a double-resonance alignment magnetometer. *Physical Review Applied*, 10(3), September 2018.

[17] Tadas Pyragius, Hans Marin Florez, and Thomas Fernholz. Voigt-effect-based three-dimensional vector magnetometer. *Physical Review A*, 100(2):023416, 2019.

[18] Aaron Smith, Brian E Anderson, Souma Chaudhury, and Poul S Jessen. Three-axis measurement and cancellation of background magnetic fields to less than 50 μg in a cold atom experiment. *Journal of Physics B: Atomic, Molecular and Optical Physics*, 44(20):205002, 2011.

[19] K-J Boller, A Imamoğlu, and Stephen E Harris. Observation of electromagnetically induced transparency. *Physical Review Letters*, 66(20):2593, 1991.

[20] F Renzoni, Wolfgang Maichen, Laurentius Windholz, and Ennio Arimondo. Coherent population trapping with losses observed on the hanle effect of the d1 sodium line. *Physical Review A*, 55(5):3710, 1997.

[21] VI Yudin, AV Taichenachev, YO Dudin, VL Velichansky, AS Zibrov, and SA Zibrov. Vector magnetometry based on electromagnetically induced transparency in linearly polarized light. *Physical Review A*, 82(3):033807, 2010.

[22] Kevin Cox, Valery I Yudin, Alexey V Taichenachev, Irina Novikova, and Eugeniy E Mikhailov. Measurements of the magnetic field vector using multiple electromagnetically induced transparency resonances in rb vapor. *Physical Review A*, 83(1):015801, 2011.

[23] Shuwei Qiu, Jinwen Wang, Francesco Castellucci, Mingtao Cao, Shougang Zhang, Thomas W. Clark, Sonja Franke-Arnold, Hong Gao, and Fuli Li. Visualization of magnetic fields with cylindrical vector beams in a warm atomic vapor. *Photonics Research*, 9(12):2325, November 2021.

[24] D. A. Steck. Rubidium 87 d line data, 2001. *URL http://steck. us/alkalidata*, 83, 2016.

[25] A. E. Kozhekin, K. Mølmer, and E. Polzik. Quantum memory for light. *Physical Review A*, 62(3):033809, 2000.

[26] B. Julsgaard, J. Sherson, J. I. Cirac, J. Fiurášek, and E. S. Polzik. Experimental demonstration of quantum memory for light. *Nature*, 432(7016):482–486, 2004.

[27] G. Alzetta, A. Gozzini, L. Moi, and G. Orriols. An experimental method for the observation of r.f. transitions and laser beat resonances in oriented na vapour. *Il Nuovo Cimento B (1971-1996)*, 36(1):5–20, Nov 1976.

[28] E. Arimondo. V coherent population trapping in laser spectroscopy. *Progress in optics*, 35:257–354, 1996.

[29] B. J. Dalton, R. McDuff, and P. L. Knight. Coherent population trapping. *Optica Acta: International Journal of Optics*, 32(1):61–70, 1985.

[30] J. P. Marangos. Electromagnetically induced transparency. *Journal of Modern Optics*, 45(3):471–503, 1998.

[31] M. Fleischhauer, A. Imamoglu, and J. P. Marangos. Electromagnetically induced transparency: Optics in coherent media. *Reviews of modern physics*, 77(2):633, 2005.

[32] K. Kowalski, V. C. Long, K. D. Xuan, M. Głódź, B. N. Huy, and J. Szonert. Electromagnetically induced transparency. *Physics Today*, 50(7):36–42, 1997.

[33] A. Forbes, A. Dudley, and M. McLaren. Creation and detection of optical modes with spatial light modulators. *Advances in Optics and Photonics*, 8(2):200–227, 2016.

[34] A. Selyem, C. Rosales-Guzmán, S. Croke, A. Forbes, and S. Franke-Arnold. Basis-independent tomography and nonseparability witnesses of pure complex vectorial light fields by Stokes projections. *Physical Review A*, 100(6):063842, 2019.

[35] A. Manthalkar, I. Nape, N. T. Bordbar, C. Rosales-Guzmán, S. Bhattacharya, A. Forbes, and A. Dudley. All-digital stokes polarimetry with a digital micromirror device. *Optics Letters*, 45(8):2319–2322, 2020.

[36] B. Zhao, X.-B. Hu, V. Rodríguez-Fajardo, A. Forbes, W. Gao, Z.-H. Zhu, and C. Rosales-Guzmán. Determining the non-separability of vector modes with digital micromirror devices. *Applied Physics Letters*, 116(9):091101, 2020.

[37] L. Allen, M. W. Beijersbergen, R. J. C. Spreeuw, and J. P. Woerdman. Orbital angular momentum of light and the transformation of laguerre-gaussian laser modes. *Physical Review A*, 45(11):8185–8189, June 1992.

[38] A. M. Yao and M. J. Padgett. Orbital angular momentum: origins, behavior and applications. *Advances in Optics and Photonics*, 3(2):161–204, 2011.

[39] R. Dorn, S. Quabis, and G. Leuchs. Sharper focus for a radially polarized light beam. *Physical review letters*, 91(23):233901, 2003.

[40] Q. Zhan. Cylindrical vector beams: from mathematical concepts to applications. *Advances in Optics and Photonics*, 1(1):1–57, 2009.

[41] G. Milione, H. I. Sztul, D. A. Nolan, and R. R. Alfano. Higher-order Poincaré sphere, Stokes parameters, and the angular momentum of light. *Physical Review Letters*, 107(5):053601, 2011.

[42] G. M. Lerman, L. Stern, and U. Levy. Generation and tight focusing of hybridly polarized vector beams. *Optics Express*, 18(26):27650–27657, 2010.

[43] X.-L. Wang, Y. Li, J. Chen, C.-S. Guo, J. Ding, and H.-T. Wang. A new type of vector fields with hybrid states of polarization. *Optics Express*, 18(10):10786–10795, 2010.

[44] Amber M Beckley, Thomas G Brown, and Miguel A Alonso. Full Poincaré beams. *Optics Express*, 18(10):10777–10785, 2010.

[45] Amber M Beckley, Thomas G Brown, and Miguel A Alonso. Full Poincaré beams ii: partial polarization. *Optics Express*, 20(9):9357–9362, 2012.

[46] Filippo Cardano, Ebrahim Karimi, Lorenzo Marrucci, Corrado de Lisio, and Enrico Santamato. Generation and dynamics of optical beams with polarization singularities. *Optics Express*, 21(7):8815–8820, 2013.

[47] Xiaohui Ling, Xunong Yi, Zhiping Dai, Youwen Wang, and Liezun Chen. Characterization and manipulation of full Poincaré beams on the hybrid Poincaré sphere. *JOSA B*, 33(11):2172–2176, 2016.

[48] Gauri Arora, P Senthilkumaran, et al. Full Poincaré beam with all the Stokes vortices. *Optics Letters*, 44(22):5638–5641, 2019.

[49] A Turpin, Yu V Loiko, A Peinado, A Lizana, TK Kalkandjiev, J Campos, and J Mompart. Polarization tailored novel vector beams based on conical refraction. *Optics Express*, 23(5):5704–5715, 2015.

[50] Peng Li, Yi Zhang, Sheng Liu, Chaojie Ma, Lei Han, Huachao Cheng, and Jianlin Zhao. Generation of perfect vectorial vortex beams. *Optics Letters*, 41(10):2205–2208, 2016.

[51] C Alpmann, C Schlickriede, E Otte, and C Denz. Dynamic modulation of Poincaré beams. *Scientific Reports*, 7(1):1–9, 2017.

[52] Lin Li, Chenliang Chang, Xiangzheng Yuan, Caojin Yuan, Shaotong Feng, Shouping Nie, and Jianping Ding. Generation of optical vortex array along arbitrary curvilinear arrangement. *Optics Express*, 26(8):9798–9812, 2018.

[53] Sheng Liu, Shuxia Qi, Yi Zhang, Peng Li, Dongjing Wu, Lei Han, and Jianlin Zhao. Highly efficient generation of arbitrary vector beams with tunable polarization, phase, and amplitude. *Photonics Research*, 6(4):228–233, 2018.

[54] Peng Li, Dongjing Wu, Yi Zhang, Sheng Liu, Yu Li, Shuxia Qi, and Jianlin Zhao. Polarization oscillating beams constructed by copropagating optical frozen waves. *Photonics Research*, 6(7):756–761, 2018.

[55] Chenliang Chang, Lin Li, Yuan Gao, Shouping Nie, Zhi-Cheng Ren, Jianping Ding, and Hui-Tian Wang. Tunable polarization singularity array enabled using superposition of vector curvilinear beams. *Applied Physics Letters*, 114(4):041101, 2019.

[56] Peng Li, Xinhao Fan, Dongjing Wu, Xuyue Guo, Yu Li, Sheng Liu, and Jianlin Zhao. Shaping vector fields in three dimensions by random fourier phase-only encoding. *Optics Express*, 27(21):30009–30019, 2019.

[57] Zhongzheng Gu, Da Yin, Fengyan Gu, Yanran Zhang, Shouping Nie, Shaotong Feng, Jun Ma, and Caojin Yuan. Generation of concentric perfect Poincaré beams. *Scientific Reports*, 9(1):1–9, 2019.

[58] Enliang Wang, Jiebin Niu, Yonghao Liang, HaiLiang Li, Yilei Hua, Lina Shi, and Changqing Xie. Complete control of multichannel, angle-multiplexed, and arbitrary spatially varying polarization fields. *Advanced Optical Materials*, 8(6):1901674, 2020.

[59] T. E. Northup and R. Blatt. Quantum information transfer using photons. *Nature Photonics*, 8(5):356–363, April 2014.

[60] Ermes Toninelli, Bienvenu Ndagano, Adam Vallés, Bereneice Sephton, Isaac Nape, Antonio Ambrosio, Federico Capasso, Miles Padgett, and Andrew Forbes. Quantum

state tomography on spatial modes with intense light: concept and implementation. 2017.

[61] Adam Selyem, Carmelo Rosales-Guzmán, Sarah Croke, Andrew Forbes, and Sonja Franke-Arnold. Basis-independent tomography and nonseparability witnesses of pure complex vectorial light fields by stokes projections. *Physical Review A*, 100(6), December 2019.

[62] Sarah Croke, Harry Jimbrown, Mustafa Al Khafaji, Adam Selyem, Sebastiao Padua, and Sonja Franke-Arnold. Tomography of structured light beams: exploring analogies with quantum measurement theory. In David L. Andrews, Enrique J. Galvez, and Halina Rubinsztein-Dunlop, editors, *Complex Light and Optical Forces XV*. SPIE, March 2021.

[63] Amy McWilliam, Claire Marie Cisowski, Robert Bennett, and Sonja Franke-Arnold. Angular momentum redirection phase of vector beams in a non-planar geometry. *Nanophotonics*, 0(0), November 2021.

[64] Fuyong Yue, Dandan Wen, Jingtao Xin, Brian D. Gerardot, Jensen Li, and Xianzhong Chen. Vector vortex beam generation with a single plasmonic metasurface. *ACS Photonics*, 3(9):1558–1563, July 2016.

[65] Yuttana Intaravanne and Xianzhong Chen. Recent advances in optical metasurfaces for polarization detection and engineered polarization profiles. *Nanophotonics*, 9(5):1003–1014, 2020.

[66] Neal Radwell, RD Hawley, JB Götte, and Sonja Franke-Arnold. Achromatic vector vortex beams from a glass cone. *Nature Communications*, 7(1):1–6, 2016.

[67] RD Hawley, R Offer, N Radwell, and S Franke-Arnold. Tight focal spots using azimuthally polarised light from a fresnel cone. In *Biomedical Spectroscopy, Microscopy, and Imaging*, volume 11359, page 1135910. International Society for Optics and Photonics, 2020.

[68] L. Marrucci, C. Manzo, and D. Paparo. Optical spin-to-orbital angular momentum conversion in inhomogeneous anisotropic media. *Phys. Rev. Lett.*, 96:163905, Apr 2006.

[69] Andrea Rubano, Filippo Cardano, Bruno Piccirillo, and Lorenzo Marrucci. Q-plate technology: a progress review. *JOSA B*, 36(5):D70–D87, 2019.

[70] V. G. Niziev, R. S. Chang, and A. V. Nesterov. Generation of inhomogeneously polarized laser beams by use of a Sagnac interferometer. *Applied Optics*, 45(33):8393, November 2006.

[71] Christian Maurer, Alexander Jesacher, Severin Fürhapter, Stefan Bernet, and Monika Ritsch-Marte. Tailoring of arbitrary optical vector beams. *New Journal of Physics*, 9(3):78, 2007.

[72] Giovanni Milione, S Evans, DA Nolan, and RR Alfano. Higher order Pancharatnam-Berry phase and the angular momentum of light. *Physical Review Letters*, 108(19):190401, 2012.

[73] E Otte, C Alpmann, and C Denz. Higher-order polarization singularitites in tailored vector beams. *Journal of Optics*, 18(7):074012, June 2016.

[74] Kevin J. Mitchell, Sergey Turtaev, Miles J. Padgett, Tomáš Čižmár, and David B. Phillips. High-speed spatial control of the intensity, phase and polarisation of vector beams using a digital micro-mirror device. *Optics Express*, 24(25):29269, December 2016.

[75] Erasmus Bartholin. An accompt of sundry experiments made and communicated by that learn'd mathematician, dr. erasmus bartholin, upon a chrystal-like body, sent to him out of island. *Philosophical Transactions of the Royal Society of London*, 5(67):2139–2148.

[76] Dmitry Budker, W Gawlik, DF Kimball, SM Rochester, VV Yashchuk, and A Weis. Resonant nonlinear magneto-optical effects in atoms. *Reviews of Modern Physics*, 74(4):1153, 2002.

[77] John Kitching, Svenja Knappe, and Elizabeth A Donley. Atomic sensors–a review. *IEEE Sensors Journal*, 11(9):1749–1758, 2011.

[78] John Kitching. Chip-scale atomic devices. *Applied Physics Reviews*, 5(3):031302, 2018.

[79] Evgeniy B Alexandrov, Marcis Auzinsh, Dmitry Budker, Derek F Kimball, Simon M Rochester, and Valeriy V Yashchuk. Dynamic effects in nonlinear magneto-optics of atoms and molecules. *JOSA B*, 22(1):7–20, 2005.

[80] FW Deeg and MD Fayer. Analysis of complex molecular dynamics in an organic liquid by polarization selective subpicosecond transient grating experiments. *The Journal of chemical physics*, 91(4):2269–2279, 1989.

[81] Ho Seong Lee, Sang Eon Park, Jong Dae Park, and Hyuck Cho. Zeeman effect in the saturation spectroscopy of the 87 rb d 2 line. *JOSA B*, 11(4):558–563, 1994.

[82] ML Harris, CS Adams, SL Cornish, IC McLeod, E Tarleton, and IG Hughes. Polarization spectroscopy in rubidium and cesium. *Physical Review A*, 73(6):062509, 2006.

[83] Geol Moon, Heung-Sik Noh, and Heung-Ryoul Noh. Effect of laser beam diameter variation in saturated absorption spectra. *Journal of the Physical Society of Japan*, 77(7):074301–074301, 2008.

[84] Huy Diep Do, Geol Moon, and Heung-Ryoul Noh. Polarization spectroscopy of rubidium atoms: theory and experiment. *Physical Review A*, 77(3):032513, 2008.

[85] Shigeru Nakayama. Optical pumping effects in high resolution laser spectroscopy. *Physica Scripta*, 1997(T70):64, 1997.

[86] Marcis Auzinsh, Dmitry Budker, and Simon Rochester. *Optically polarized atoms: understanding light-atom interactions*. Oxford University Press, 2010.

[87] Liron Stern, Anat Szapiro, Eliran Talker, and Uriel Levy. Controlling the interactions of space-variant polarization beams with rubidium vapor using external magnetic fields. *Optics Express*, 24(5):4834, February 2016.

[88] Larry J Hornbeck. Digital light processing for high-brightness high-resolution applications. In *Projection Displays III*, volume 3013, pages 27–40. International Society for Optics and Photonics, 1997.

[89] A. Selyem. Three-dimensional light sculptures and their interaction with atomic media, ph.d dissertation, university of glasgow. 2019.

[90] Carmelo Rosales-Guzmán, Xiao-Bo Hu, Adam Selyem, Pedro Moreno-Acosta, Sonja Franke-Arnold, Ruben Ramos-Garcia, and Andrew Forbes. Polarisation-insensitive generation of complex vector modes from a digital micromirror device. *Scientific Reports*, 10(1), June 2020.

[91] Sijia Gao, Fiona C. Speirits, Francesco Castellucci, Sonja Franke-Arnold, Stephen M. Barnett, and Jörg B. Götte. Paraxial skyrmionic beams. *Physical Review A*, 102(5), November 2020.

[92] A non-linear field theory. *Proceedings of the Royal Society of London. Series A. Mathematical and Physical Sciences*, 260(1300):127–138, February 1961.

[93] T.H.R. Skyrme. A unified field theory of mesons and baryons. *Nuclear Physics*, 31:556–569, March 1962.

[94] Stefano Donati, Lorenzo Dominici, Galbadrakh Dagvadorj, Dario Ballarini, Milena De Giorgi, Alberto Bramati, Giuseppe Gigli, Yuri G. Rubo, Marzena Hanna Szymańska, and Daniele Sanvitto. Twist of generalized skyrmions and spin vortices in a polariton superfluid. *Proceedings of the National Academy of Sciences*, 113(52):14926–14931, December 2016.

[95] Zernike von F. Beugungstheorie des Schneidenver-fahrens und seiner verbesserten Form, der Phasenkontrastmethode. *Physica*, 1(7-12):689–704, 1934.

[96] Grigory Lazarev, Friedemann Gädeke, and Jarek Luberek. Ultrahigh-resolution phase-only LCOS spatial light modulator. In Liang-Chy Chien, editor, *Emerging Liquid Crystal Technologies XII*. SPIE, February 2017.

[97] C. E. Wieman, D. E. Pritchard, and D. L. Wineland. Atom cooling, trapping, and quantum manipulation. *Reviews of Modern Physics*, 71(2):S253–S262, March 1999.

[98] H. J. Metcalf and P. van der Straten. Laser cooling and trapping of atoms. *Journal of the Optical Society of America B*, 20(5):887, May 2003.

[99] H. Metcalf and P. van der Straten. Cooling and trapping of neutral atoms. *Physics Reports*, 244(4-5):203–286, August 1994.

[100] W. D. Phillips. Nobel lecture: Laser cooling and trapping of neutral atoms. *Reviews of Modern Physics*, 70(3):721, 1998.

[101] C. Cohen-Tannoudji and D. Guéry-Odelin. Advances in atomic physics: an overview. 2011.

[102] P. Meystre. *Atom optics*, volume 33. Springer Science & Business Media, 2001.

[103] A. S. Arnold, J. S. Wilson, and M. G. Boshier. A simple extended-cavity diode laser. *Review of Scientific Instruments*, 69(3):1236–1239, 1998.

[104] Hr4000 and hr4000cg-uv-nir series spectrometers installation and operation manual.

[105] D. W. Preston. Doppler-free saturated absorption: Laser spectroscopy. *American Journal of Physics*, 64(11):1432–1436, November 1996.

[106] Christopher J Foot et al. *Atomic physics*, volume 7. Oxford University Press, 2005.

[107] E. A. Donley, T. P. Heavner, F. Levi, M. O. Tataw, and S. R. Jefferts. Double-pass acousto-optic modulator system. *Review of Scientific Instruments*, 76(6):063112, June 2005.

[108] D. E. Pritchard. Cooling neutral atoms in a magnetic trap for precision spectroscopy. *Physical Review Letters*, 51(15):1336, 1983.

[109] A. L. Migdall, J. V. Prodan, W. D. Phillips, T. H. Bergeman, and H. J. Metcalf. First observation of magnetically trapped neutral atoms. *Physical Review Letters*, 54(24):2596, 1985.

[110] A. Ashkin, J. M. Dziedzic, J. E Bjorkholm, and S. Chu. Observation of a single-beam gradient force optical trap for dielectric particles. *Optics letters*, 11(5):288–290, 1986.

[111] T. Bergeman, G. Erez, and H. J. Metcalf. Magnetostatic trapping fields for neutral atoms. *Physical Review A*, 35(4):1535, 1987.

[112] H. F. Hess. Evaporative cooling of magnetically trapped and compressed spin-polarized hydrogen. *Physical Review B*, 34(5):3476, 1986.

[113] W. Petrich, M. H. Anderson, J. R Ensher, and E. A. Cornell. Stable, tightly confining magnetic trap for evaporative cooling of neutral atoms. *Physical Review Letters*, 74(17):3352, 1995.

[114] M. H. Anderson, J. R. Ensher, M. R. Matthews, C. E. Wieman, and E. A. Cornell. Observation of Bose-Einstein condensation in a dilute atomic vapor. *Science*, 269(5221):198–201, 1995.

[115] K. B. Davis, M. Mewes, M. R. Andrews, N. J. van Druten, D. S. Durfee, D.M. Kurn, and W. Ketterle. Bose-einstein condensation in a gas of sodium atoms. *Physical review letters*, 75(22):3969, 1995.

[116] F. S. Cataliotti, E. A. Cornell, C. Fort, M. Inguscio, F. Marin, M. Prevedelli, L. Ricci, and G. M. Tino. Magneto-optical trapping of fermionic potassium atoms. *Phys. Rev. A*, 57:1136–1138, Feb 1998.

[117] P. Kapitza. Viscosity of Liquid Helium below the λ-Point. *Nat*, 141:74, January 1938.

[118] E. L. Raab, M. Prentiss, Alex Cable, Steven Chu, and D. E. Pritchard. Trapping of neutral sodium atoms with radiation pressure. *Phys. Rev. Lett.*, 59:2631–2634, Dec 1987.

[119] K. Dieckmann, R. J. C. Spreeuw, M. Weidemüller, and J. T. M. Walraven. Two-dimensional magneto-optical trap as a source of slow atoms. *Physical Review A*, 58(5):3891, 1998.

[120] T. W. Hänsch and A. L. Schawlow. Cooling of gases by laser radiation. *Optics Communications*, 13(1):68–69, 1975.

[121] A. Ashkin. Applications of laser radiation pressure. *Science*, 210(4474):1081–1088, 1980.

[122] William D. Phillips and Harold Metcalf. Laser deceleration of an atomic beam. *Phys. Rev. Lett.*, 48:596–599, Mar 1982.

[123] A.S. Arnold. Preparation and manipulation of an 87rb bose-einstein condensate, ph.d dissertation, university of sussex. 1999.

[124] W. Ketterle, K. B. Davis, M. A. Joffe, A. Martin, and D. E. Pritchard. High densities of cold atoms in a dark spontaneous-force optical trap. *Physical review letters*, 70(15):2253, 1993.

[125] C. G. Townsend, N. H. Edwards, K. P. Zetie, C. J. Cooper, J. Rink, and C. J. Foot. High-density trapping of cesium atoms in a dark magneto-optical trap. *Physical Review A*, 53(3):1702, 1996.

[126] N. Radwell, G. Walker, and S. Franke-Arnold. Cold-atom densities of more than 10^{12} cm^{-3} in a holographically shaped dark spontaneous-force optical trap. *Phys. Rev. A*, 88:043409, Oct 2013.

[127] V. Y. Bazhenov, M. V. Vasnetsov, and M. S. Soskin. Laser beams with screw dislocations in their wavefronts. *Jetp Lett*, 52(8):429–431, 1990.

[128] Jacques Vanier and Cipriana Tomescu. The quantum physics of atomic frequency standards: recent developments. 2015.

[129] James Keaveney. *Collective atom–light interactions in dense atomic vapours*. Springer, 2014.

[130] T.W. Clark. Sculpting shadows. on the spatial structuring of fields atoms: a tale of light and darkness, ph.d dissertation, university of glasgow. 2016.

[131] Marlan O Scully and M Suhail Zubairy. Quantum optics, 1999.

[132] John S Toll. Causality and the dispersion relation: logical foundations. *Physical review*, 104(6):1760, 1956.

[133] Jacob B Khurgin and Rodney S Tucker. *Slow light: Science and applications*. CRC press, 2018.

[134] G. F. Quinteiro, D. E. Reiter, and T. Kuhn. Formulation of the twisted-light–matter interaction at the phase singularity: The twisted-light gauge. *Physical Review A*, 91(3), March 2015.

[135] N. Radwell, T. W. Clark, B. Piccirillo, S. M. Barnett, and S. Franke-Arnold. Spatially dependent electromagnetically induced transparency. *Phys. Rev. Lett.*, 114:123603, Mar 2015.

[136] C. Affolderbach, M. Stähler, S. Knappe, and R. Wynands. An all-optical, high-sensitivity magnetic gradiometer. 75(6-7):605–612, November 2002.

[137] Dmitry Budker and Michael Romalis. Optical magnetometry. 3(4):227–234, April 2007.

[138] A. Selyem, S. Fayard, T.W. Clark, A.S. Arnold, N. Radwell, and S. Franke-Arnold. Holographically controlled three-dimensional atomic population patterns. *Optics Express*, 26(14):18513, July 2018.

[139] V. Acosta, M. P. Ledbetter, S. M. Rochester, D. Budker, D. F. Jackson Kimball, D. C. Hovde, W. Gawlik, S. Pustelny, J. Zachorowski, and V. V. Yashchuk. Nonlinear magneto-optical rotation with frequency-modulated light in the geophysical field range. *Physical Review A*, 73(5), May 2006.

[140] S. Pustelny, A. Wojciechowski, M. Gring, M. Kotyrba, J. Zachorowski, and W. Gawlik. Magnetometry based on nonlinear magneto-optical rotation with amplitude-modulated light. *Journal of Applied Physics*, 103(6):063108, March 2008.

[141] S. Gateva, L. Gurdev, E. Alipieva, E. Taskova, and G. Todorov. Narrow structure in the coherent population trapping resonances in rubidium and rayleigh scattering. *Journal of Physics B: Atomic, Molecular and Optical Physics*, 44(3):035401, January 2011.

[142] S. Afach, G. Ban, G. Bison, K. Bodek, Z. Chowdhuri, Z. D. Grujić, L. Hayen, V. Hélaine, M. Kasprzak, K. Kirch, P. Knowles, H.-C. Koch, S. Komposch, A. Kozela, J. Krempel, B. Lauss, T. Lefort, Y. Lemière, A. Mtchedlishvili, O. Naviliat-Cuncic, F. M. Piegsa, P. N. Prashanth, G. Quéméner, M. Rawlik, D. Ries, S. Roccia, D. Rozpedzik, P. Schmidt-Wellenburg, N. Severjins, A. Weis, E. Wursten, G. Wyszynski, J. Zejma, and G. Zsigmond. Highly stable atomic vector magnetometer based on free spin precession. *Opt. Express*, 23(17):22108–22115, Aug 2015.